Density Profiles of Ionic Liquids at a Hard Wall

Diplomarbeit von
Sebastian M. Schramm

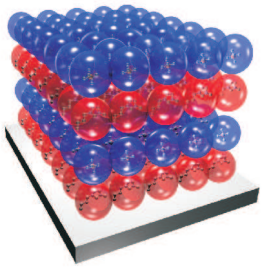

Hauptberichter : Prof. Dr. H. Dosch
Mitberichter : Prof. Dr. J. Wrachtrup

Max-Planck-Institut
für Metallforschung
in Stuttgart

Institut für Theoretische
und Angewandte Physik
der Universität Stuttgart

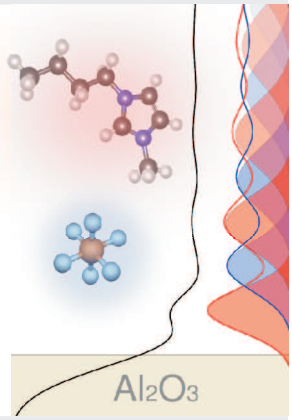

Stuttgart, den 02. Mai 2008

Density Profiles of Ionic Liquids at a Hard Wall

Diplomarbeit von Sebastian M. Schramm

Hauptberichter : Prof. Dr. H. Dosch

Mitberichter : Prof. Dr. J. Wrachtrup

Max-Planck-Institut für Metallforschung
in Stuttgart

Institut für Theoretische und Angewandte Physik
der Universität Stuttgart

Stuttgart, den 02. Mai 2008

Contents

Deutsche Zusammenfassung

Einführung

Ionische Flüssigkeiten (Room Temperature Ionic Liquids - RTILs) sind Salze mit einem Schmelzpunkt unterhalb von $100\,^{\circ}\mathrm{C}$. Sie bestehen aus voluminösen organischen Kationen und größtenteils anorganischen Anionen die vermehrt auch organische Seitenketten besitzen. In den letzten Jahren ist das Interesse an RTILs wegen Ihrer charakteristischen Eigenschaften stark gestiegen. RTILs besitzen eine einzigartige Kombination von Eigenschaften, wie z.B. einen sehr geringen Dampfdruck bei Raumtemperatur, einen niedrigen Schmelzpunkt und ein großes elektrochemisches Fenster. Daraus ergibt sich ein weites Anwendungsfeld für RTILs z.B. als recyclebare *grüne Lösungsmittel*, als Elektrolyt in einer Reihe von elektrochemischen Prozessen oder als vielseitiges Schmiermittel. Aufgrund ihrer einzigartigen Eigenschaften haben RTILs auch die Aufmerksamkeit der Grundlagenforschung auf sich gezogen.

Schmelzen herkömmlicher Salze wurden schon lange vor der Synthese der ersten RTILs verwendet und untersucht. Der hohe Schmelzpunkt (Kochsalz schmilzt erst oberhalb von $800\,^{\circ}\mathrm{C}$) schränkt die Anwendungsmöglichkeiten dieser Schmelzen stark ein. Auch ist das Studium dieser Flüssigkeiten aufgrund der benötigten komplexen und aufwendigen Experimentierumgebungen erschwert.

Die erste RTIL wurde bereits 1914 durch Walden et al. [1] entdeckt. Allerdings zersetzt sich diese erste Generation von RTILs bei Kontakt mit dem in der Luft enthaltenen Wasserdampf. Im Jahre 1992 wurde die erste erfolgreiche Synthese von RTILs, die sich bei Kontakt mit Luft und Wasser nicht zu zersetzen schienen, berichtet [2]. Die Möglichkeit, RTILs auch bei Umgebungsbedingungen einsetzen zu können, eröffnete ihnen einen größeren Anwendungsbereich.

Ein hervorstechendes Merkmal der RTILs ist die Möglichkeit, ihre physikalischen und chemischen Eigenschaften in einem weiten Bereich zu verändern. Deshalb werden Sie auch *Designer-Lösungsmittel* genannt. Die Eigenschaften der RTILs können durch Veränderung der chemischen Zusammensetzung ihrer Kationen und/oder ihrer Anionen variiert werden. Bisher geschieht dies aufgrund von Erfahrung und nach der Methode von Versuch und Irrtum. Ein fundamentaleres Verständnis der Wechselwirkungen in RTILs könnte die Vorhersage von Eigenschaften bestimmter RTILs ermöglichen. Umgekehrt könnte dann auch die notwendige chemische Struktur für eine RTIL mit einer bestimmten Konstellation an physikalischen und chemischen Eigenschaften bestimmt werden.

In der Mehrzahl der Anwendungen für RTILs spielen Grenzflächen eine wesentliche Rolle. Für die Kontrolle des Verhaltens und der Leistungsfähigkeit von RTILs z.B. als Elektrolyt in Batterien, als Lösungsmittel oder als Schmiermittel ist die Kenntnis des Grenzflächenverhaltens von RTILs auf molekularer Ebene unerlässlich. Es ist zu erwarten, dass sich das Verhalten von RTILs in einer eingeschränkten Geometrie wie z.B. an einer Grenzfläche gegenüber dem im Volumen unterscheidet. Auf der anderen Seite ist es auch möglich, aufgrund des gestörten Kräftegleichgewichts an der Grenzfläche Eigenschaften zu beobachten und zu studieren, die im Volumen der Flüssigkeit schwerer zugänglich sind (siehe z.B. Reichert et al. [3]). Das Studium des Verhaltens von RTILs an einer Grenzfläche ist daher nicht nur für Anwendungen relevant, sondern könnte auch zu einem tieferen physikalischen Verständnis der RTILs beitragen.

Die Grenzfläche zwischen flüssigen RTILs und Gasphase ist die am ausführlichsten untersuchte Grenzfläche, da sie mit einer Vielzahl von experimentellen Techniken zugänglich ist. Dem gegenüber sind bisher nur wenige Studien über die fest-flüssig Grenzfläche veröffentlicht worden. In einem großen Teil der theoretischen Arbeiten wurde das Grenzflächenverhalten mit Hilfe von Modellpotentialen für RTILs simuliert [4, 5]. Neben wenigen Rasterkraftmikroskopie (AFM) Experimenten [6], finden sich zu fest-flüssig Grenzflächen in der Literatur hauptsächlich Ergebnisse spektroskopischer Messungen (SFG) [7, 8]. In dieser Arbeit wurde ein für das Studium von tief vergrabenen Grenzflächen angepasster Messplatz an dem Strahlrohr ID15A der Europäischen Synchrotron Strahlungsquelle (ESRF) verwendet [9]. Mit Hilfe eines hochenergetischen ($E = 72.5\,\mathrm{keV}$) Röntgenmikrostrahls wurden Elektronendichteprofile an der Grenzfläche zu Saphir mit molekularer Auflösung bestimmt. Die folgenden vier RTILs wurden in dieser Arbeit untersucht:

1. 1-Butyl-3-Methylimidazol Tetrafluorborate ([bmim$^+$][BF$_4^-$])
2. 1-Butyl-3-Methylimidazol Hexafluorphosphate ([bmim$^+$][PF$_6^-$])
3. 1-Hexyl-3-Methylimidazol Bi(trifluormethylsulfonyl)imide ([hmim$^+$][Tf$_2$N$^-$])
4. 1-Butyl-1-Methylpyrrolidin Bi(trifluormethylsulfonyl)imide ([bmpy$^+$][Tf$_2$N$^-$])

In den Systemen 2-4 wurde an der Grenzfläche zu Saphir eine molekulare Schichtstruktur mit Anionen und Kationen in getrennten Lagen beobachtet. Zusätzlich zu den Röntgenmessungen wurden Oberflächen- und Grenzflächenspannungen der vier RTILs bestimmt.

Hochenergie Röntgenreflektivität

Bei Reflektivitätsmessungen wird die Intensität eines an einer Grenzfläche reflektierten Röntgenstrahls in Abhängigkeit des vertikalen Impulsübertrages gemessen. Dies geschieht durch die symmetrische Variation des Einfallwinkels und Ausfallwinkels. Die Reflektivitätskurve enthält Informationen über das Elektronendichteprofil senkrecht zur untersuchten Grenzfläche. Konventionelle Röntgenreflektivitätsexperiements werden

typischer Weise mit einer Strahlenenergie von 10-20 keV durchgeführt. Dies führt dazu, dass die Röntgenstrahlen bereits nach wenigen $100\,\mu\mathrm{m}$ absorbiert sind. Mit hochenergetischer Röntgenstrahlung ($\approx 70\,\mathrm{keV}$) sind aufgrund der geringeren Absorption tief vergrabene Grenzflächen experimentell zugänglich. Aufgrund der kleineren Winkel bei gleichem Impulsübertrag werden für hochenergetische Reflektivitätsexperimente sehr präzise Diffraktometer benötigt. Ein Diffraktometer mit der notwendigen Präzision wurde 2003 in unserer Arbeitsgruppe entwickelt [9].

Zur Rekonstruktion der Grenzflächenstruktur aus den gemessenen Reflektivitätskurven wurden aus Modellen für die Elektronendichte Reflektivitäskurven mit Hilfe des Parratt und des Master Formalismus berechnet. Die berechneten Reflektivitätskurven sind mit Hilfe eines Computeralgorithmus an die gemessenen Reflektivitäten angepasst worden. Der verwendete Monte Carlo Algorithmus [10] erlaubt auch in hochdimensionalen Parameterräumen das Auffinden des globalen Minimum und ermöglicht somit die zuverlässige Bestimmung von Elektronendichteprofilen aus den Reflektivitätskurven.

Experimentelles

In dieser Arbeit wurden vier verschiedene RTILs untersucht. Die Flüssigkeiten wurden von der Firma Merck KGaA [11] mit hohem Reinheitsgrad bezogen. Um flüchtige Verunreinigungen wie Wasser aus den ionischen Flüssigkeiten zu entfernen, wurden diese bei einer Temperatur von $80\,^{\circ}\mathrm{C}$ für 24 Stunden einem Vakuum von $1\,\mathrm{mbar}$ ausgesetzt. Als Modell für eine harte Wand wurden Proben aus Saphir mit (0001) Oberflächenorientierung verwendet. Die Saphir Substrate wurden in einer Reihe von organischen Lösungsmitteln gereinigt und anschließend in Piranha Lösung geätzt. Die so erreichte hydrophile OH-Terminierung wurde durch in einer Sauerstoff Atmosphäre mit UV-Licht erzeugtes Ozon verstärkt.

Die Röntgenreflektivitätsexperimente wurden am Hochenergiemessplatz ID15A der Europäischen Synchrotron Strahlungsquelle (ESRF) in Grenoble, Frankreich mit Hilfe eines neuartigen und speziell für Grenz- und Oberflächen Experimente optimierten Hoch-Energie-Mikro-Diffraktometers (HEMD) durchgeführt. Ein hochenergetischer Röntgenstrahl ($E = 72.5\,\mathrm{keV}$) wird mit einem Linsensystem (CRL), bestehend aus 194 einzelnen parabolischen Aluminiumlinsen, auf die Probenposition fokussiert. Der Röntgenstrahl kann damit auf eine Größe von $6\,\mu\mathrm{m} \times 26\,\mu\mathrm{m}$ (vertikal $\times$ horizontal) gebündelt werden. Somit wird auch bei kleinen Einfallswinkeln α_i ein möglichst kurzer Beleuchtungsfleck erzeugt. Die Strahlendosis wurde mittels eines dreieckigen Absorberblocks aus Polymethylmethacrylat (PMMA) sowie einer schnell schließenden Verschlussblende im Primärstrahl soweit als möglich reduziert, um eine Zerstörung der organischen Moleküle weitestgehend zu vermeiden.

Die verwendete Probenkammer wurde speziell für Reflektivitätsmessungen entwickelt. Sie ist vakuumtauglich bis zu einem Druck von etwa $10^{-6}\,\mathrm{mbar}$. Die Temperatur der Kammer kann im Bereich von $-120\,^{\circ}\mathrm{C}$ bis $+250\,^{\circ}\mathrm{C}$ eingestellt werden. Alle Materialien die sich in direktem Kontakt mit der Probe befinden sind chemisch inert und einfach zu reinigen um Verunreinigungen zu vermeiden.

Die Messungen der Oberflächen- und Grenzflächenspannungen wurden an dem Gerät OCA 30 (Dataphysics) mit der *Pendant Drop* Methode durchgeführt.

Ergebnisse und Diskussion

Von den vier verschiedenen untersuchten RTILs, enthalten zwei das gleiche Kation, [bmim$^+$], und die am häufigsten und umfangreichsten analysierten Anionen, [BF_4^-] und [PF_6^-]. Die anderen beiden RTILs gehören zu einer neueren Gruppe von RTILs mit einer verbesserten elektrochemischen Stabilität. Sie enthalten das gleiche Anion, [Tf_2N^-], und ein pyrrolidin-basiertes bzw. ein imidazol-basiertes Kation. Der systematische Austausch der Ionen-Typen in diesen vier RTILs ließ einen ausgeprägten Einfluss des Ionen-Paares auf das Grenzflächenverhalten erkennen.

Zusätzliche Informationen über die Wechselwirkungen in den untersuchten Systemen wurden durch Messungen der Oberflächen- und Grenzflächenspannung mit n-Hexan bei Normalbedingungen für alle vier RTILs erhalten. Die Oberflächenspannungen der RTILs sind größer als die Oberflächenspannung von n-Hexan aber dennoch kleiner als die von Wasser. Die Messungen zeigten, dass kleinere Änderungen des Ionen-Typus nur einen geringen Einfluss auf die Oberflächen- und Grenzflächenspannung hat. Die Ergebnisse deuten daraufhin, dass die flüssig-gas Grenzflächen von RTILs und RTIL-n-Hexan Grenzflächen zu annähernd gleichen Teilen aus Kationen und Anionen bestehen, d.h. es findet keine Ladungstrennung an diesen Grenzflächen statt.

Die Ergebnisse zur Struktur an der Grenzfläche wurde mit Hilfe von Röntgenstreuexperimenten im Volumen der Flüssigkeiten in Zusammenhang mit den Volumeneigenschaften der RTILs gesetzt. Diese Messungen zeigten, dass ausgeprägte räumliche Korrelationen in den RTILs vorhanden sind. In allen Fällen wurden Korrelationen beobachtet, die dem Ring-Ring Abstand der Kationen oder der ersten Solvatisierungsschale des Anions zugeschrieben wurden. Ein ausgeprägtes Merkmal, welches auf Kationen Zentroid-Zentroid Korrelationen oder Kation-Kation Abstände hindeutet, wurde in der Volumenflüssigkeitsstreuung von [bmim$^+$][PF_6^-], [hmim$^+$][Tf_2N^-] und [bmpy$^+$][Tf_2N^-] beobachtet. Die imidazol-basierten RTILs zeigten zusätzliche Streusignale im Bereich kleiner Impulsüberträge. Diese Signale wurden mittelreichweitigen Korrelationen der Alkyl-Ketten der Kationen zugeordnet, was durch Ergebnisse aus der Literatur unterstützt wird. Es wurde keine signifikante Temperaturabhängigkeit der Flüssigkeitskorrelationen festgestellt. Der Vergleich von Korrelationsabständen in der flüssigen Phase mit denen im kristallinen Zustand von [bmim$^+$][PF_6^-] zeigt, dass auch in der flüssigen Phase ein großes Maß an Strukturordnung ähnlich dem kristallinen Zustand vorhanden ist. Für [bmpy$^+$][Tf_2N^-] führte die Sättigung mit Wasser (maximal $14800\,\mathrm{ppm}$ Wasser können gelöst werden [12]) zu keiner Veränderung der Volumenflüssigkeitskorrelationen im untersuchten q-Bereich .

Die Messungen der Röntgenreflektivitäten zeigen deutlich, dass eine molekulare Schichtstruktur von ladungsgetrennten Doppellagen an der Grenzfläche zu Saphir bei den RTILs [bmim$^+$][PF_6^-], [hmim$^+$][Tf_2N^-] und [bmpy$^+$][Tf_2N^-] vorhanden ist. Der Lagenabstand beträgt ungefähr $6.5\,\mathrm{\AA}$. [bmim$^+$][BF_4^-] zeigte keine Merkmale einer

Schichtstruktur in dem untersuchten q-Bereich. Die räumlich ausgedehnteste Schichtstruktur an der RTIL-Saphir Grenzfläche mit einer Abklinglänge von etwa 1.5 Lagenabständen wurde für [bmim$^+$][PF_6^-] beobachtet. Im Falle von [hmim$^+$][Tf_2N^-] fällt die Schichtstruktur über ungefähr 1.1 Lagenabstände ab. Bereits nach etwa 0.5 Lagenabständen zerfällt die ladungsgetrennte Schichtstruktur von [bmpy$^+$][Tf_2N^-]. Eine Temperaturabhängigkeit der Röntgenreflektivität konnte nur für die Grenzfläche [bmpy$^+$][Tf_2N^-]-Saphir beobachtet werden. Dieses Temperaturverhalten könnte durch eine Änderung der Konformation des pyrrolidin-Rings des Kations verursacht werden. Bei mit Wasser gesättigtem [bmpy$^+$][Tf_2N^-] wurde keine Schichtstruktur beobachtet.

Die RTILs, die eine molekulare Schichtstruktur an der Grenzfläche zu Saphir ausbilden, zeigen Korrelationsabstände in den Volumenstreuexperimenten, die den Lagenabständen der Schichtstrukturen ähnlich sind. Der Wert der Oberflächenspannungen der RTILs hängt nur in geringem Maße von den Ionen-Typen ab. Die Grenzflächenstruktur hängt jedoch signifikant von den Ionen ab. Es wird daraus gefolgert, dass die ladungsgetrennten molekularen Schichtstrukturen an einer harten Wand der Tendenz zur Ordnungsbildung in der Volumenflüssigkeit folgen.

Mit zwei Modellen für das Elektronendichteprofil, dem semi-quantitativen (SQ) generischen Lagen-Modell und dem modifizierten deformierten Kristall (DC) Modell, wurden vergleichbare Werte für den Lagenabstand und die Zerfallslänge der molekularen Schichtstruktur erhalten. Die Ergebnisse für den Lagenabstand und die Zerfallslänge werden daher als fundierte zuverlässige Werte betrachtet. Das DC Modell führte mit einer Kationenlage am Saphirsubstrat zu deutlich besseren Ergebnissen gegenüber einer Anionenlage am Saphirsubstrat.

In dieser Arbeit wurde erstmals eine Analyse der Grenzflächen zwischen RTILs und einer harten Wand mit molekularer Auflösung mit Hochenergieröntgenreflektivität vorgenommen. Unsere Daten zeigen deutlich, dass eine exponentiell gedämpfte, ladungsgetrennte Schichtstruktur senkrecht zur Grenzfläche an Saphir auftritt, hervorgerufen durch Eigenschaften der Volumenflüssigkeit. Die Zerfallslängen hängen entscheidend von den Ionen in den RTILs ab. Wegen der komplexen Natur der untersuchten Systeme und der ungeheuren Anzahl an RTILs sind weitere Studien notwendig, auch mit anderen experimentellen Techniken, um diese ersten Ergebnisse zur Struktur von RTILs an fest-flüssig Grenzflächen mit molekularer Auflösung zu bestätigen.

Introduction

Room temperature ionic liquids (RTILs) are molten salts consisting solely of ions with a melting point below $100\,^{\circ}\mathrm{C}$. Most RTILs are composed of relatively large (polyatomic) organic cations and inorganic anions. In the last few years the interest in them experienced an enormous growth. Their unique and useful properties like non-volatility, low melting point, and a wide electrochemical window render them suitable for a wide range of applications, i.e. as green solvents, or as electrolytes in a variety of electrochemical processes, and have also drawn the attention of fundamental research.

The first RTIL was synthesized as early as 1914 [1]. Only almost 80 years later, in 1992, the first synthesis of an air and water stable RTIL was reported, enabling applications at ambient conditions. Even before the synthesis of the first RTIL, efforts were made to employ conventional salts for technological processes. However, due to the high melting points of conventional salts (sodium chloride starts to melt above $800\,^{\circ}\mathrm{C}$) possible applications were limited. Sophisticated and complex experimental environments are necessary to handle these high temperature ionic liquids.

A novel characteristic of RTILs is that their properties can easily be modified in a wide range. For this reason they are also referred to as designer solvents. The modification is accomplished by varying the chemical composition of the bulky organic cations and/or inorganic anions of the RTILs. So far, this is guided by experience and trial and error. A more fundamental understanding of the interactions present in RTILs could lead to reliable predictions of the properties of a certain RTIL. Vice versa, it could be used to define the composition of the RTIL ions for a specific set of properties.

In many of the applications of RTILs the interface is a vital component. In order to control the performance of RTILs used as electrolytes in batteries, as solvents, or as versatile lubricants, the knowledge of the interfacial behavior at a molecular level is of outmost importance. It is expected that the behavior in a confined geometry, e.g. at interfaces, differs significantly from the bulk. On the other hand, the interfacial behavior could readily reveal interaction forces and properties which are accessible only with major efforts from the bulk liquid [3]. Thus, the study of RTIL interfaces is not only essential for many applications, but may also lead to a deeper understanding of the bulk liquid. So far, most studies were focused on the RTIL-vapor interface, since the RTIL surface can be accessed straightforward with a large variety of experimental techniques [7, 8, 13–15]. In contrast, only a few studies of the RTIL-solid interface are available up to now. A large part of these studies are computational, employing model potentials for the description of the RTILs [4, 5]. Besides a few attempts of using atomic force microscopy (AFM) or scanning tunneling microscopy (STM) [6] mainly sum-

frequency vibrational spectroscopy (SFG) [7, 8] has been used to study the RTIL-solid interface. In this work, an optimized experimental scheme was used in order to access deeply-buried interfaces for studies of the RTIL-solid interface [9]: A high energy x-ray microbeam ($E = 72.5\,\mathrm{keV}$) probes the interface in transmission-reflection geometry. Measurements of the x-ray reflectivity allowed it to deduce the electron density distribution in the vicinity of an interface with molecular resolution.

A total of four RTILs has been investigated for this diploma thesis:

1. 1-butyl-3-methylimidazolium tetrafluoroborate ([bmim$^+$][BF_4^-])
2. 1-butyl-3-methylimidazolium hexafluorophosphate ([bmim$^+$][PF_6^-])
3. 1-hexyl-3-methylimidazolium bis(trifluoromethylsulfonyl)imide ([hmim$^+$][Tf_2N^-])
4. 1-butyl-1-methylpyrrolidinium bis(trifluoromethylsulfonyl)imide ([bmpy$^+$][Tf_2N^-])

In the systems 2-4 we found molecular layering at the interface with the different ion types stratified in separate layers. In addition to the structural investigations, measurements of surface and interface tensions have been performed.

Chapter 1

Basic description of the system

1.1 Room Temperature Ionic Liquids (RTILs)

What is a room temperature ionic liquid (RTIL)? In principle, it is a molten salt, thus consisting solely of ions, with a melting point below $100\,^{\circ}\mathrm{C}$. Most RTILs are composed of relatively large (polyatomic) organic cations and inorganic anions. Among the more common cations are the ones based on imidazolium and pyrrolidinium. More recently synthesized anions also contain fluorocarbon groups.

One of the first RTILs has been discovered as early as 1914 [1], yet it was unstable when exposed to water vapor. In 1992, the successful synthesis of air and water stable RTILs with 1-alkyl-3-methylimidazolium based cations and less reactive anions such as tetrafluoroborate was reported [2]. This led to a broader spectrum of possible applications, and therefore to a growing interest in RTILs. The rising scientific interest in RTILs and their potential applications has triggered an explosive progress in the field of RTIL synthesis and fundamental research. Nowadays more than 300 RTILs are commercially available in high purity [11]. Studies focusing on the basic physico-chemical properties of the most common RTILs are available to a large extent. The rapidly increasing research activity is reflected in the exponentially growing number of publications per year since 1992 (see Fig. 1.1).

RTILs have drawn attention due to their unique properties. The most striking are a negligible vapor pressure at ambient temperature, wide electrochemical window, low viscosity, versatile solvent capability, and large liquidus range. The liquidus range of RTILs is limited at the high temperature end by decomposition rather than vaporization due to a low vapor pressure. The decomposition of RTILs occurs in the range $300\,^{\circ}\mathrm{C}$ - $450\,^{\circ}\mathrm{C}$ [17] due to pyrolysis. The vapor pressure for several RTILs, among them [bmim$^+$][Tf_2N^-] and [bmpy$^+$][Tf_2N^-], has been determined to be $6\,\mathrm{mbar}$ at $300\,^{\circ}\mathrm{C}$ [18]. RTILs fall into a class of newtonian fluids with a significantly high viscosity compared to conventional solvents [17]. Many RTILs exhibit a strong temperature dependence in their viscosities.

In addition, these properties can be tuned and adjusted by changing the structure and the composition of the ions composing the RTIL. A certain constellation of required properties for a specific application can be met by varying the nature of the ions, there-

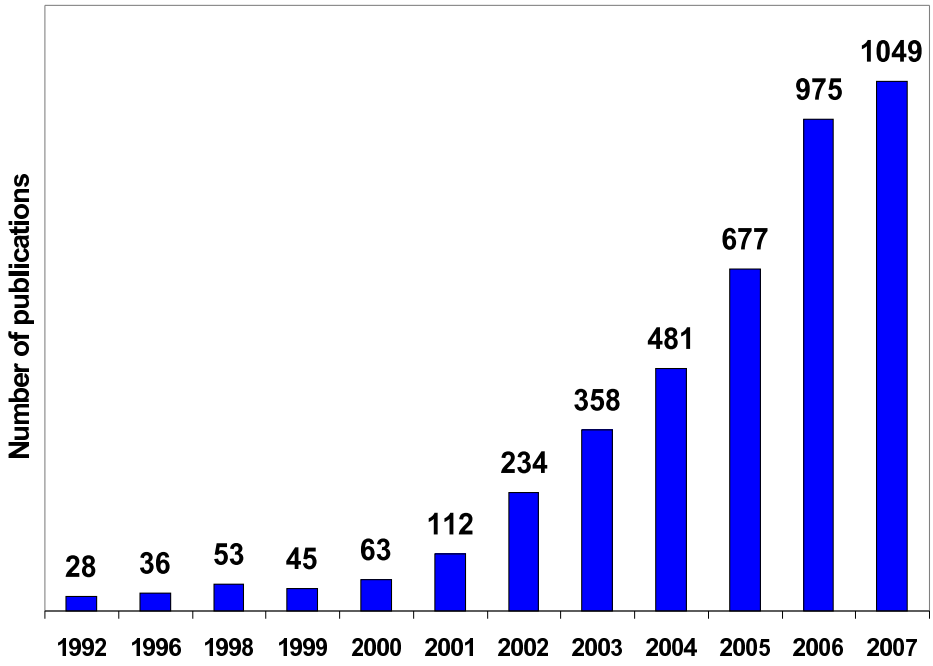

Figure 1.1: Number of publications per year containing the phrase *ionic liquid* in their title as obtained from Scifinder scholar [16].

fore they are sometimes called designer solvents. A fundamental understanding of the correlation between the chemical structure of the RTIL ions and their corresponding properties is only about to arise. Hence, the before mentioned tuning of properties is achieved mostly by trial and error.

A large variety of applications already employ the unique characteristics of RTILs (see Fig. 1.2). Among them are electrochemistry, synthesis, catalysis and biocatalysis, analytics and sensorics, and engineering fluids. The applications of RTILs in these fields span a wide range. A few examples are the use as electrolytes in batteries [19], in gas sensors [20] and for electrodeposition [6, 21], as versatile high performance lubricants [22, 23], as heat transfer fluids [24], as matrix medium in gas chromatography [25], as solvents in catalytic reactions replacing volatile organic solvents [26], and as solvents in studying the ripening process of bananas [27]. Just recently RTILs were employed in building the prototype of a lunar liquid mirror telescope [28].

Beside the fact that RTILs have outstanding properties making them suitable for a broad spectrum of applications, they represent a unique model system from a physical point of view. A complex combination of van der Waals, Coulomb, dipole, and hydrogen interactions are present in RTILs. The impact of each interaction force may be studied systematically by changing the structure of the cations or anions. By adding a dielectric solvent into a RTIL screening of the Coulomb forces can be obtained as a function of the solvent concentration [29]. Another aspect is that the energy/entropy ratio of the free energy is much closer to the one of atomic systems compared to the colloidal systems at mesoscopic length scale which are widely used to mimic and study structural aspects and fluctuations of atomic systems.

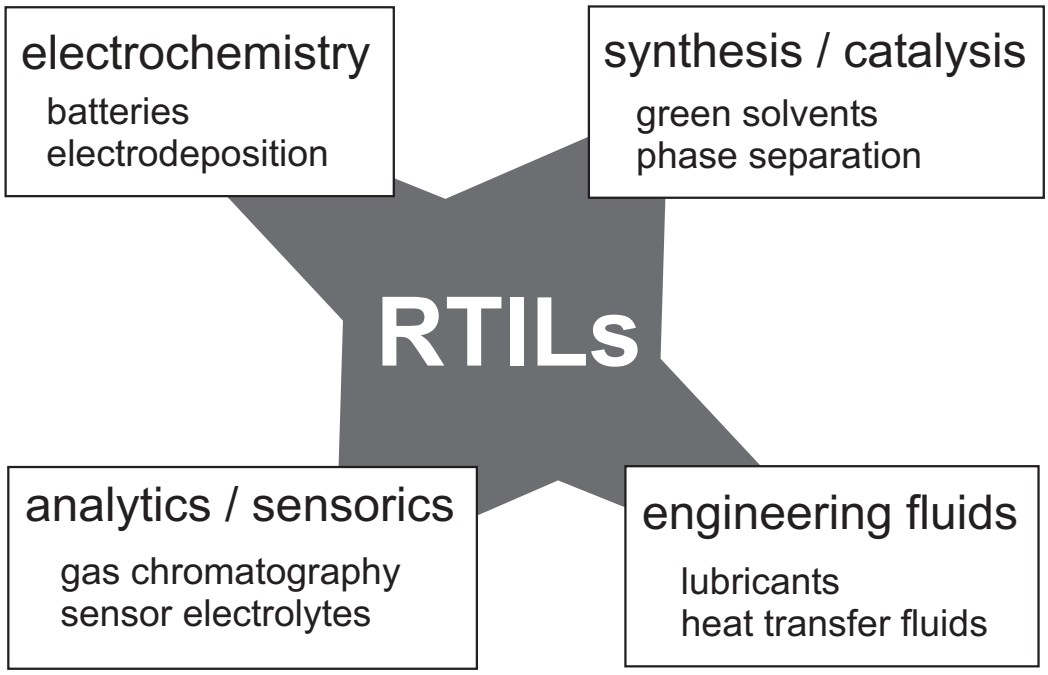

Figure 1.2: Overview of the most common fields employing RTILs.

1.2 RTILs at interfaces

Many of the potential applications of RTILs involve the presence of interfaces as a vital component. In tribology, for instance, the performance and the efficiency of a RTIL as lubricant depends highly on the interfacial properties. In electrochemistry, the electron transfer between the RTIL and an electrode, depends crucially on the nature of the interface. For such applications the knowledge of the interfacial structure of RTILs at molecular level is essential. The study of RTIL interfaces may also lead to a deeper understanding of the physical and chemical properties of the bulk liquid since the symmetry break and unbalanced forces at the interface may reveal interactions, behavior, and properties which are difficult to probe in the bulk liquid itself.

Experimental techniques which have been used to study RTIL-vapor interfaces on a molecular level are direct recoil spectrometry (DRS), sum-frequency generation vibrational spectroscopy (SFG), and neutron and x-ray reflectivity. Due to the low vapor pressure, also ultra high vacuum-based techniques such as ultraviolet photoemission spectroscopy (UPS), x-ray photoelectron spectroscopy (XPS), and metastable impact electron spectroscopy (MIES) have been applied to reveal the structure of RTIL-vapor interfaces. In addition, molecular dynamics simulations have been carried out for the RTIL-vapor interface. The properties of RTIL-vapor interfaces determined by the different techniques qualitatively agree with each other. All studies report a well-ordered structure for one layer at the interface. On the other hand, there are still open questions concerning the details of ion orientation and the composition of the first layer at the interface. SFG measurements [7, 8, 30, 31] revealed that the surface layer is composed of an equal amount of cations and anions. The same result was reported by the DRS

studies [13, 14, 32]. Surface x-ray reflectivity found a $10\,\%$ enhancement in the anion density in the surface layer compared to the bulk liquid [15] and no ion layering. Molecular dynamics simulations of the same system confirm the result of the x-ray reflectivity study of the enhanced anion density at the surface [33,34], but predicted a layering of the ions near the surface. The picture of the cation orientation at the interface is still blurry. The orientation of the cation could not be revealed by x-ray reflectivity. SFG measurements reported a orientation of the imidazolium ring of the cation which is parallel or only slightly tilted with respect to the surface, whereas the alkyl chains point towards the vapor phase away from the liquid. DRS investigations revealed an imidazolium ring orientation perpendicular to the surface with the alkyl chains aligned along the surface. As different as these results on the cation orientation may seem at first, molecular dynamics simulations showed that indeed both imidazolium ring orientations are present in different regions of the liquid-vapor interface. In denser areas the imidazolium ring is aligned along the surface normal, whereas less dense regions closer to the vapor phase are composed of cations with their imidazolium rings oriented parallel to the surface plane [33].

Studies concerning the structure at RTIL-liquid interfaces are rather scarce. Interfaces between two immiscible electrolyte solutions (ITIES) with one of them being a RTIL have been studied, focusing mainly on cyclic voltammetry at the liquid-liquid interface, electrocapillarity, and molecular dynamics studies [35, 36].

Up to now, only a few experimental techniques are capable of probing RTIL-solid interfaces and even less with subnanometer resolution. Among them are SFG, x-ray reflectivity, atomic force microscopy (AFM), and scanning tunneling microscopy (STM) [6]. SFG studies focusing on the RTIL-SiO_2 interface have been reported by two different groups [7, 8]. They both suggested an imidazolium ring orientation more parallel to the surface plane than perpendicular to it. Romero et al. [8] described a significant anion impact on the cation orientation near the interface. They also revealed that both ions are present at an interface with hydrophilic SiO_2, whereas the imidazolium ring of the cation is slightly tilted out of the interface towards the interface normal. The tilt angle of the cation was reported to increase with an increase of the size of the anion composing the RTIL. However, Rollins et al. [7] found only a negligible anion impact but a strong alkyl chain length influence on the cation alignment in the interfacial regime. More particular, the authors found that the imidazolium rings are aligned more parallel to the interface with decreasing alkyl chain length. The same effect appeared by increasing the negative surface charge of the quartz substrate.

1.3 Investigated RTILs

In the course of this work four RTILs have been investigated. Two of them share the same cation, 1-butyl-3-methylimidazolium [$bmim^+$] but different anions, hexafluorophosphate [PF_6^-] and tetrafluoroborate [BF_4^-]. They are among the most widely used and extensively studied RTILs since they are easy and cheap to synthesize. In addition, they are supposed to be air and water stable - exactly the properties required to re-

place volatile organic compounds in large scale industrial chemical processes. The other two RTILs contain the same anion, bis(trifluoromethylsulfonyl)imide [Tf_2N^-] but different cations, 1-hexyl-3-methylimidazolium [$hmim^+$] and 1-butyl-1-methylpyrrolidinium [$bmpy^+$]. RTILs containing [Tf_2N^-] exhibit exceptional properties like hydrophobicity, high thermal and electrochemical stability, low viscosity, high conductivity, and low melting point. Thus, they are well suited as solvents for synthetic and electrochemical applications [37]. In the following, the physico-chemical properties of these four RTILs are summarized and discussed. Figure 1.3 shows the structural formulae of the ions composing the four investigated RTILs and Fig. 1.4 depicts sketches of the molecular geometry of these ions.

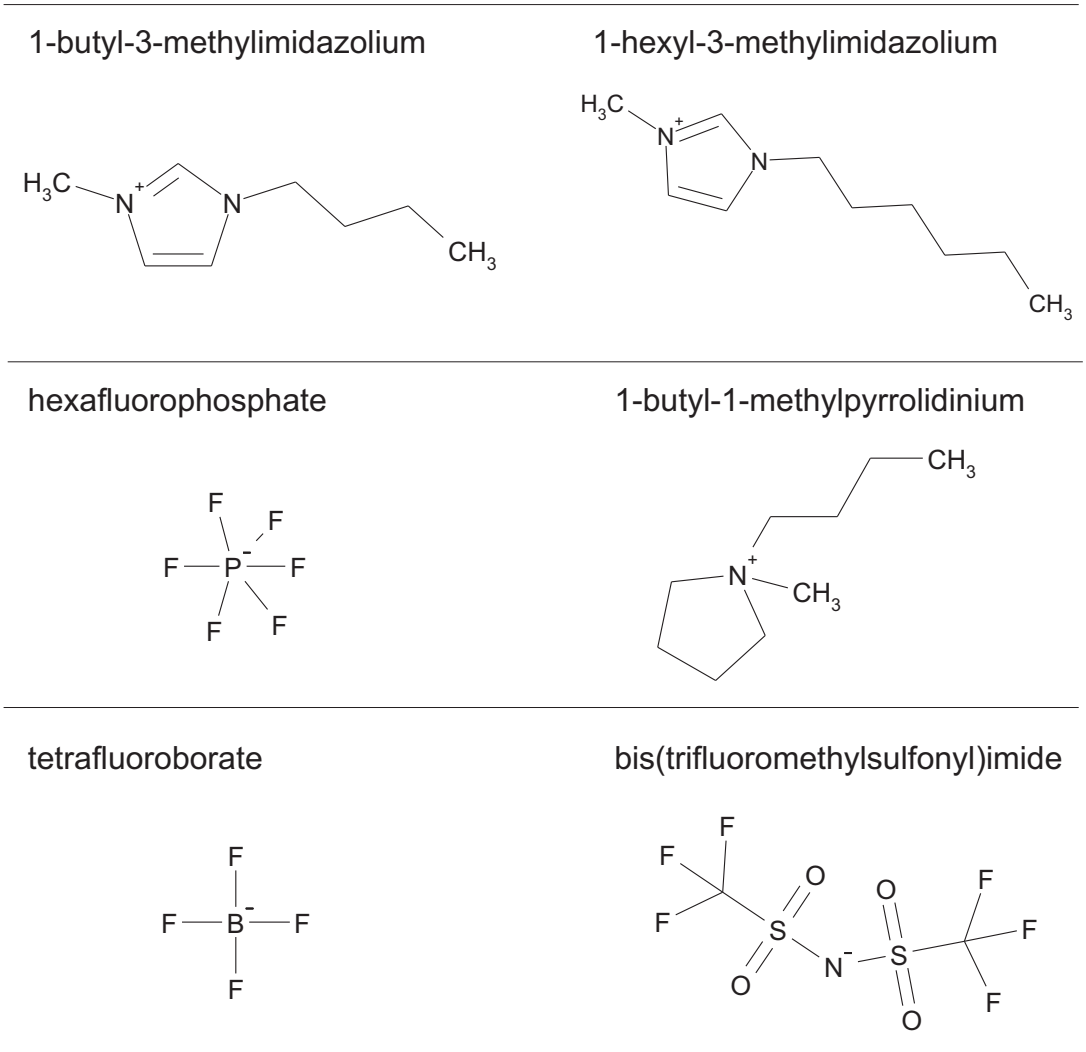

Figure 1.3: Structural formulae of the ions composing the four RTILs investigated in this work.

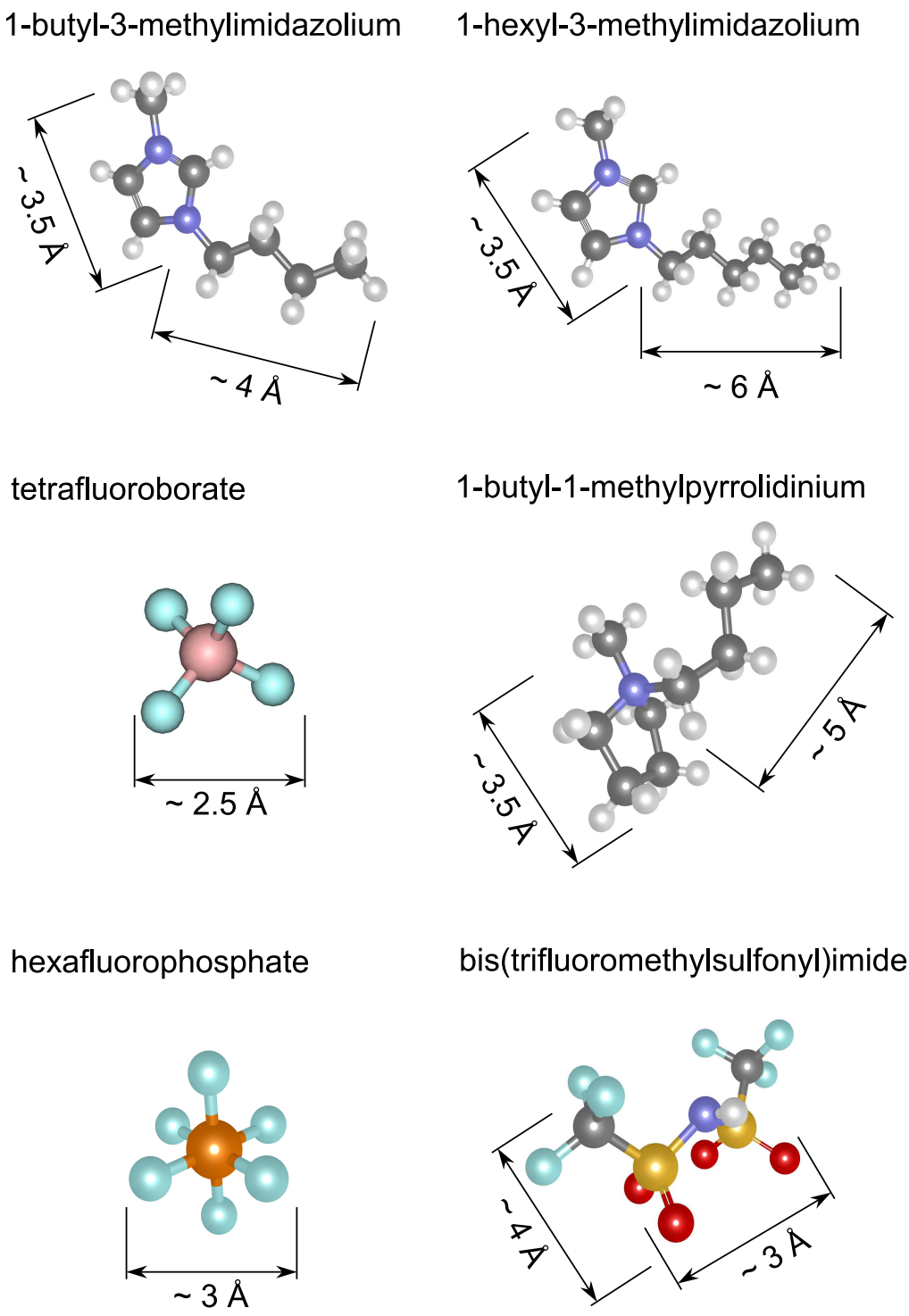

Figure 1.4: Sketch of the molecular geometry of the ions investigated in this work (taken from the database Scifinder Scholar [16]; carbon: gray, hydrogen: white, nitrogen: blue, fluorine: light blue, boron: pink, phosphorus: orange, sulfur: yellow, oxygen: red). Typical distances in the molecular ions are indicated.

Table 1.1: Physico-chemical properties of the four RTILs. The molar mass $\mathrm{m}\,/(\mathrm{g\,mol^{-1}})$, melting point $\mathrm{T_p}\,/(^\circ\mathrm{C})$, glass transition temperature $\mathrm{T_g}\,/(^\circ\mathrm{C})$, bulk liquid density $\varrho\,/(\mathrm{g\,cm^{-3}})$, index of refraction n, viscosity $\eta\,/(\mathrm{mPa\,s})$, surface tension $\gamma\,/(\mathrm{mN\,m^{-1}})$, electrical conductivity $\sigma\,/(10^{-3}\,\mathrm{S\,cm^{-1}})$, maximum water uptake $\kappa\,/(\mathrm{ppm})$, and electrochemical window $\mathrm{W}\,/(\mathrm{V})$.

	[bmim$^+$][PF$_6^-$]	[bmim$^+$][BF$_4^-$]	[hmim$^+$][Tf$_2$N$^-$]	[bmpy$^+$][Tf$_2$N$^-$]
CAS no.	174501-64-5	174501-65-6	382150-50-7	223437-11-4
Formula	$C_8H_{15}F_6N_2P$	$C_8H_{15}BF_4N_2$	$C_{12}H_{19}F_6N_3O_4S_2$	$C_{11}H_{20}F_6N_2O_4S_2$
m	284.18	226.02	447.42	422.41
$\mathrm{T_p}$ [d]	12.0		-15.0	-6.0
$\mathrm{T_g}$ [d]	-77.0	-83.0	-81.0	-83.0
ϱ [e]	1.37	1.21	1.38	1.40
n [f]	1.411	1.429	—	—
η [d]	182.0	75.0	56.0	60.0
γ [c]	43.5	44.2	31.0	33.2
σ [d]	1.9	4.5	2.7	3.4
κ	22600 [a]	miscible [b]	10670 [a]	14800 [a]
W [d]	4.2 [g]	4.1 [g]	6.3 [a]	6.8 [a]

[a]: *taken from Ignat'ev et al. [12].*
[b]: *taken from Huddleston et al. [38].*
[c]: *measured in this work at $T = 22\,^\circ\mathrm{C}$ (see Sec. 4.2).*
[d]: *$T = 30\,^\circ\mathrm{C}$; taken from Tokuda et al. [39]*
[e]: *measured in this work (see Sec. 4.1).*
[f]: *$T = 20\,^\circ\mathrm{C}$, λ in the optical regime; taken from Carda-Broch et al. [40].*
[g]: *taken from Schroeder et al. [41].*

Most RTILs exhibit a rather complex thermal behavior. They do not crystallize upon cooling from the liquid state due to slow solidification kinetics but form metastable glass states at low temperatures, typically around $-80\,^\circ\mathrm{C}$. Heating a RTIL sample in the glassy state leads in many cases to crystallization and, subsequently, melting. Figure 1.5 shows a temperature dependent differential scanning calorimetry (DSC) plot of [bmim$^+$][PF$_6^-$] measured by Choudhury et al. [42]. It is therefore not always straigthforward to determine the melting point and the glass transition of RTILs. This is reflected in the broad scatter of the values of these properties found in literature. This should be kept in mind upon using the values summarized in Tab. 1.1.

The influence of the ion size and their symmetry on the melting point has already been studied extensively [17]. An increase of the cation and/or anion size leads to a lower melting point for two reasons. First, the interionic distance increases with the ions getting bigger. Second, with increasing ion sizes the ionic charges become less localized. The melting point changes also upon modification of the ion symmetry. The symmetry can be influenced by the position and length/size of substitutes at the ions. As a rule of thumb one might say that for more symmetric ions, the melting point is

increasing. On the other hand, by increasing the length of the alkyl chain in 1-alkyl-3-methylimidazolium cations, the corresponding RTILs ([Nmim$^+$] [PF_6^-]) showed a decrease of the melting point up to $N = 8$ (octyl), followed by an increase of the melting point with a further increase of N [17]. A comparison of the melting points of [bmim$^+$][PF_6^-] and [hmim$^+$][Tf_2N^-] supports these ideas on the dependence of the melting point on ion size and symmetry.

The dynamic viscosities of the RTILs investigated in this work are in the range of $50\,\mathrm{mPa\,s}$ to $200\,\mathrm{mPa\,s}$ (water exhibits a dynamic viscosity of $0.894\,\mathrm{mPa\,s}$). For the viscosity of [bmim$^+$] [PF_6^-], an increase of $27\,\%$ at a temperature change from $25\,^\circ\mathrm{C}$ to $20\,^\circ\mathrm{C}$ was reported [17]. The solvation properties vary with cation and anion type. [bmim$^+$][BF_4^-] is known to be hydrophilic, whereas [bmim$^+$][PF_6^-], [hmim$^+$][Tf_2N^-], and [bmpy$^+$][Tf_2N^-] are hydrophobic [17]. Hydrophobic RTILs are discussed as replacements of volatile organic compounds in aqueous/RTIL biphase separation schemes [17]. The hydrophobic [bmim$^+$][PF_6^-] has been found to be totally miscible with aqueous ethanol between 0.5 and $0.9\,\mathrm{mol}$ fraction of ethanol in contrast to partial miscibility with pure ethanol [43]. The majority of the RTILs, including the ones investigated in this work, are known to be hygroscopic [17]. The wide electrochemical windows qualify RTILs for applications in electrochemical processes if they are chemically stable. [hmim$^+$][Tf_2N^-] and [bmpy$^+$][Tf_2N^-] exhibit a higher electrochemical stability compared to [bmim$^+$][PF_6^-] and [bmim$^+$][BF_4^-]. Mainly [PF_6^-], but also [BF_4^-], decompose by hydrolysis in contact with moisture especially at high temperatures, forming hazardous volatiles like HF and POF_3 [44]. This is a serious drawback for the application of these RTILs in industrial processes.

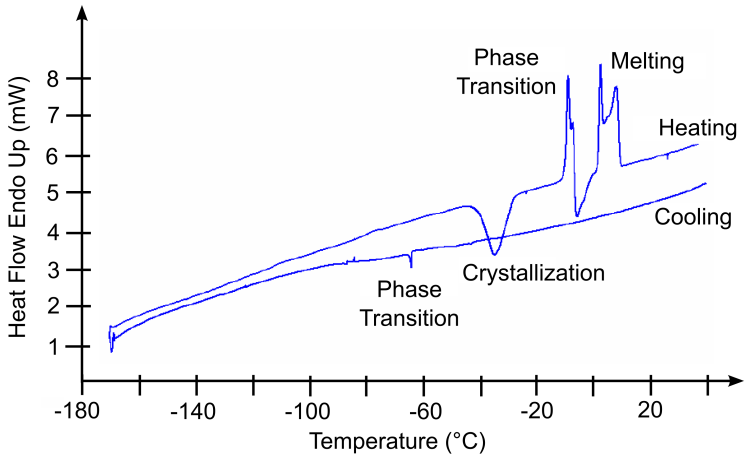

Figure 1.5: Differential scanning calorimetry plot of [bmim$^+$][PF_6^-] reproduced from Choudhury et al. [42].

Chapter 2

X-ray scattering and analysis methods

The first section of this chapter serves as a reminder of some common issues and equations of the x-ray reflectivity theory. An extensive review of x-ray reflectivity techniques can be found in [45], [46], and [47]. Subsequently, analysis methods for reconstructing the electron density profile from measured reflectivity data are discussed, followed by an introduction of the models for the electron density profile used in this work. The last section elaborates on a basic description of the structural correlations of liquids and how they are experimentally accessible. Further details about the liquid state of matter can be found in Ref. [48], [49], and [50].

2.1 X-ray reflectivity

X-ray reflectivity is an experimentell technique for gaining information about the vertical structure of an interface. A varying refractive index n along the interface normal leads to a partial reflection of the incident beam and thus to an interference pattern which contains information about the electron density distribution.

2.1.1 Scattering geometry

Figure 2.1 shows a sketch of the scattering geometry. The difference between scattered and incident wave vector determines the momentum transfer $\mathbf{q} = \mathbf{k}_f - \mathbf{k}_i$. The components of the momentum transfer (for the orientation of the coordinate system see Fig. 2.1) are given by

$$\mathbf{q} = \begin{pmatrix} q_x \\ q_y \\ q_z \end{pmatrix} = \begin{pmatrix} k\left(\cos\alpha_f \cos\chi - \cos\alpha_i\right) \\ k\cos\alpha_i \sin\chi \\ k\left(\sin\alpha_i + \sin\alpha_f\right) \end{pmatrix} \tag{2.1}$$

with $k = 2\pi/\lambda$ as the modulus of the wave vector, and χ as the horizontal component of the total angle $\alpha_i + \alpha_f$ between $\mathbf{k}_f$ and $\mathbf{k}_i$. In reflectivity measurements ($\chi = 0$, $\alpha = \alpha_i = \alpha_f$) the components of the momentum transfer are

$$(q_x, q_y, q_z) = (0, 0, 2k\sin\alpha) \tag{2.2}$$

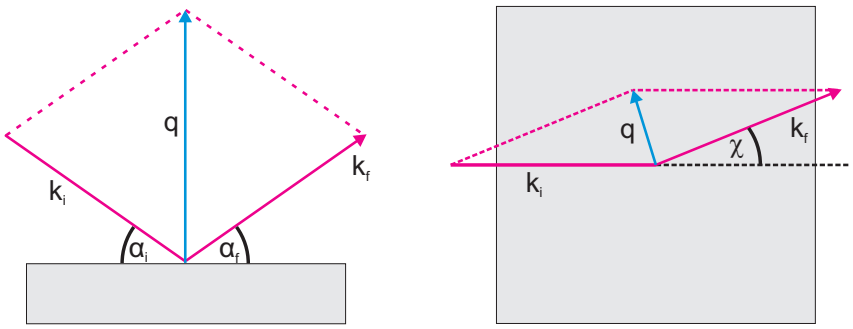

Figure 2.1: Sketch of the geometry for a surface or interface sensitive scattering experiment.

For small angles $\sin\alpha \approx \alpha$, and Eq. (2.2) can be simplified to $(q_x, q_y, q_z) = (0, 0, 2k\alpha)$. All reflectivity measurements presented here were recorded in this regime ($\alpha < 30\,\mathrm{mrad}$).

2.1.2 Resolution

The momentum transfer resolution for the out-of-plane scattering geometry ($\chi = 0$) can be obtained by calculating the total differential of Eq. (2.1).

$$\delta q_l = \frac{\partial q_l}{\partial \lambda}\Delta\lambda + \frac{\partial q_l}{\partial \alpha_i}\Delta\alpha_i + \frac{\partial q_l}{\partial \alpha_f}\Delta\alpha_f \tag{2.3}$$

with $l = x, y, z$. In the reflectivity geometry the experimental resolution is given by

$$\delta q_x = q_z\left(\Delta\alpha_i + \Delta\alpha_f\right) \tag{2.4}$$

$$\delta q_z = \frac{\Delta\lambda}{\lambda} q_z + k\left(\Delta\alpha_i + \Delta\alpha_f\right). \tag{2.5}$$

For reflectivity scans, the detector slits have to be adjusted such, that all reflected intensity is detected within the resolution range.

2.1.3 Refractive index

The refractive index n of a medium for incident x-rays with a wave vector $k = 2\pi/\lambda$ is given by

$$n = 1 - \delta + i\beta \tag{2.6}$$

$$\delta = \frac{\lambda^2}{2\pi} r_e \rho_e \frac{f^{(1)}(E)}{Z} \approx \frac{\lambda^2}{2\pi} r_e \rho_e \tag{2.7}$$

$$\beta = \frac{\lambda^2}{2\pi} r_e \rho_e \frac{f^{(2)}(E)}{Z} = \frac{\lambda}{4\pi}\mu, \tag{2.8}$$

where δ represents the dispersion, β the absorption, and $f^{(1)}(E)$ and $f^{(2)}(E)$ the energy-dependent form factors for forward scattering (see Ref. [51]). The approximation for the dispersion is valid far away from absorption edges.

2.1.4 Reflection at one ideal interface

The intensity of a reflected wave from an ideal interface, the so-called Fresnel reflectivity R_F^2, is given by the square of the reflection coefficient of the Fresnel formula. Since the polarization is negligible at small scattering angles, the reflection coefficient for all polarizations is given by

$$R_F = \frac{k_{i,z} - k_{t,z}}{k_{i,z} + k_{t,z}}, \tag{2.9}$$

where $k_{i,z} = k \sin \alpha_i$ and $k_{t,z} = n_2/n_1 k \sin \alpha_t$. For $\alpha_i > 3\alpha_c$ a good approximation for the Fresnel reflectivity reads

$$R_F^2 \approx \left(\frac{\alpha_c}{2\alpha_i} \right)^4 \approx (4\pi r_e \rho_e)^2 \frac{1}{q_z^4} \tag{2.10}$$

with $\alpha_c \approx \sqrt{2\delta} = \lambda \sqrt{\frac{r_e}{\pi} \rho_e}$ denoting the critical angle of total reflection, and $r_e = 2.8179 \cdot 10^{-15}\,\mathrm{m}$ as the classical electron radius. This relationship describes the rapid decline of the intensity for incident angles $\alpha_i \gg \alpha_c$. For $\alpha_i \leq \alpha_c$ the reflected intensity is almost unity. Exemplarily, the calculated critical angle for the sapphire/vacuum interface is $\alpha_c \approx 0.032°$ for $\lambda = 0.171\,\text{Å}$.

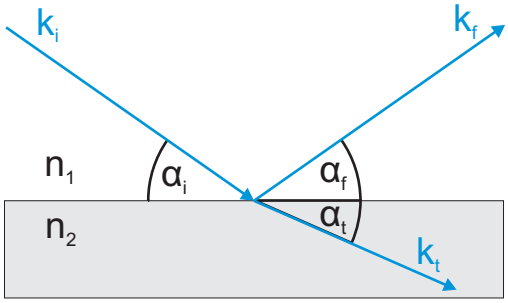

Figure 2.2: Reflection and refraction of a plane electromagnetic wave: An incident plane wave with wave vector $\mathbf{k}_i$ hits the interface at an incident angle α_i. It splits into a reflected wave ($\alpha_i = \alpha_f$) with wave vector $\mathbf{k}_f$ and a transmitted wave with wave vector $\mathbf{k}_t$ at an angle α_t.

2.1.5 Buried interfaces

Interfaces buried under a macroscopic amount of material are regarded as deeply-buried. They are difficult to access at conventional x-ray energies ($10 - 20\,\mathrm{keV}$) but readily accessible with high energy x-rays since the attenuation coefficient decreases rapidly with increasing photon energy. A transmission-reflection scheme, developed in our group in 2003 [9], was used for the investigations reported in this work. Figure 2.3 compares it to a conventional reflection scheme. Several advantages are obvious: The reflection pattern obtained in transmission geometry contains only information from the buried interface, whereas the conventional geometry may lead to a complex pattern containing information from the buried interface together with information from at least the

interface between the top layer and air. Also the thickness of the top layer forming the interface is no longer limited to a few microns. Details about the analysis of reflectivity data from buried interfaces can be found in Ref. [51].

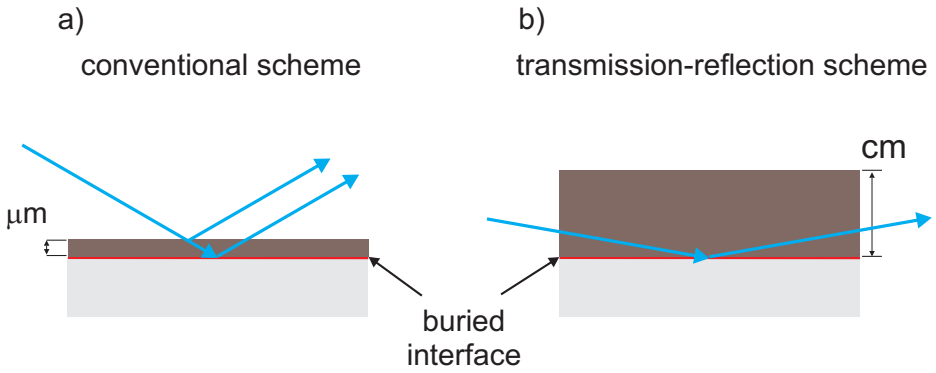

Figure 2.3: a) Conventional setup of an interface scattering experiment. b) Transmission-reflection scheme. In the conventional geometry the reflected waves from all interfaces are contributing to the reflection pattern.

2.1.6 Multiple interfaces

In many cases one has to deal with stratified media, i.e. multilayers. The reflection and transmission of each interface can be calculated using the Fresnel formulae. In addition, the corresponding retardation between the different layers has to be taken into account. A sketch of a system with N layers plus substrate ($N+1$) is shown in Fig. 2.4. Each layer is characterized by a refractive index n_j and a thickness d_j. The top layer and the substrate are considered as semi-infinite. The N interfaces of the system are located at the positions z_j. R_j represents a reflected wave propagating in layer j, and T_{j+1} is a wave transmitted into layer $j+1$. Furthermore, a transmitted wave T_j from interface $j-1$ and a reflected wave R_{j+1}, created at interface $j+1$, appear at interface j. By definition, there is no wave propagating within the substrate, and the incident wave impinging on the top layer is $T_1 = 1$

In order to solve the problem of a multilayer system consistently a recursive method is used, the so-called Parratt formalism [45, 52]. The reflectivity is calculated from the squared modulus of the transition coefficient

$$R^2 = |X_1|^2 = \left|\frac{r_1}{t_1}\right|^2 \tag{2.11}$$

with r_j the reflection coefficient and t_j the transmission coefficient of the interface j to be obtained by the Fresnel formulae. X_1 is obtained recursively starting with the transition coefficient at the substrate $X_{N+1} = 0$:

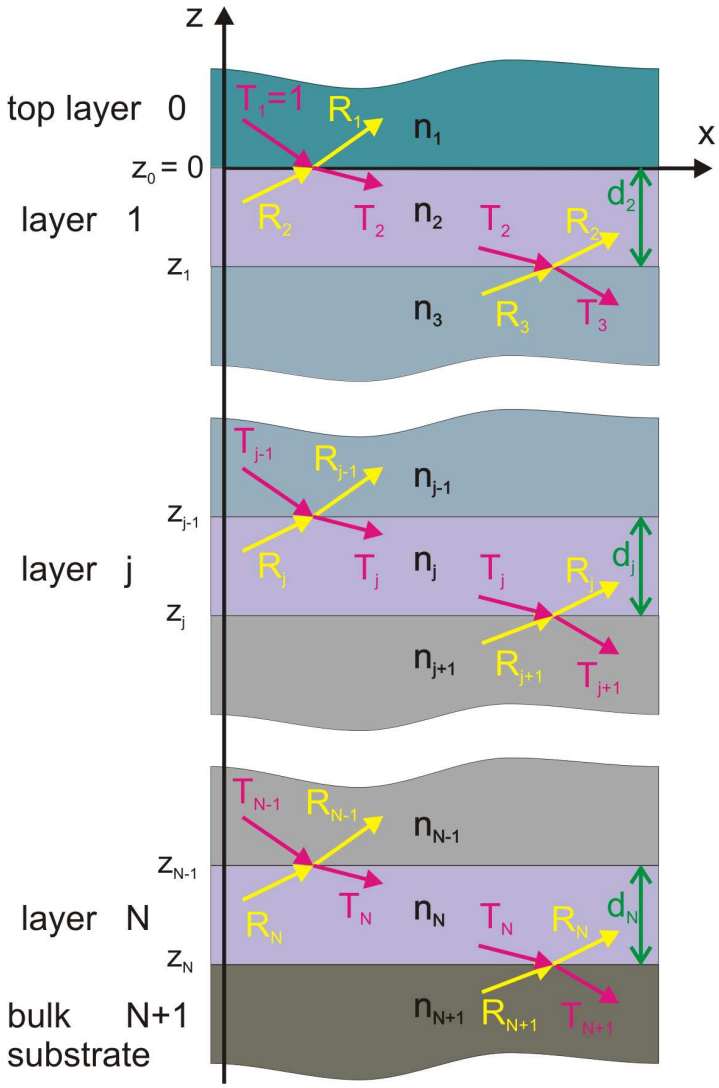

Figure 2.4: Reflection and refraction of a plane wave at a system of multiple interfaces.

$$X_j = \frac{R_j}{T_j} = \varphi_{j,j} \frac{r_{j,j+1} + X_{j+1}\varphi_{j+1,j}}{1 + r_{j,j+1} X_{j+1}\varphi_{j+1,j}} \tag{2.12}$$

$$r_{j,j+1} = \frac{k_{j,z} - k_{j+1,z}}{k_{j,z} + k_{j+1,z}} \tag{2.13}$$

$$\varphi_{n,m} = \exp\left(-2ie^{i(n+m)\pi} k_{n,z} z_m\right). \tag{2.14}$$

Interfacial roughness has to be taken into account to describe a real system since there will always be corrugations at least on an atomic length scale at any interface. Using an error function interfacial profile instead of a sharp step function profile leads to a reflection coefficient modified by an exponential damping factor. The Nevot-Croce approach describes the roughness of an interface with no in-plane correlations. An interface with

a correlated roughness can be described with the Beckmann-Spizzichino approach. In this work, the Nevot-Croce description was applied:

$$r'_{j,j+1} = r_{j,j+1} e^{-2k_{j,z}k_{j+1,z}\sigma_j^2} \tag{2.15}$$

$$\sigma_j = \sqrt{\langle [h_j(x,y)]^2 \rangle_{\text{spatial}}} \tag{2.16}$$

with σ_j the RMS roughness parameter and $h_j(x,y)$ the height distribution function.

The modified reflection coefficients $r'_{j,j+1}$ can be used within the Parratt formalism to calculate the corresponding reflectivity under the condition that $\sigma_j \ll d_j$ and $\sigma_j \ll d_{j-1}$ for all layers j, i.e that the interfaces are well separated.

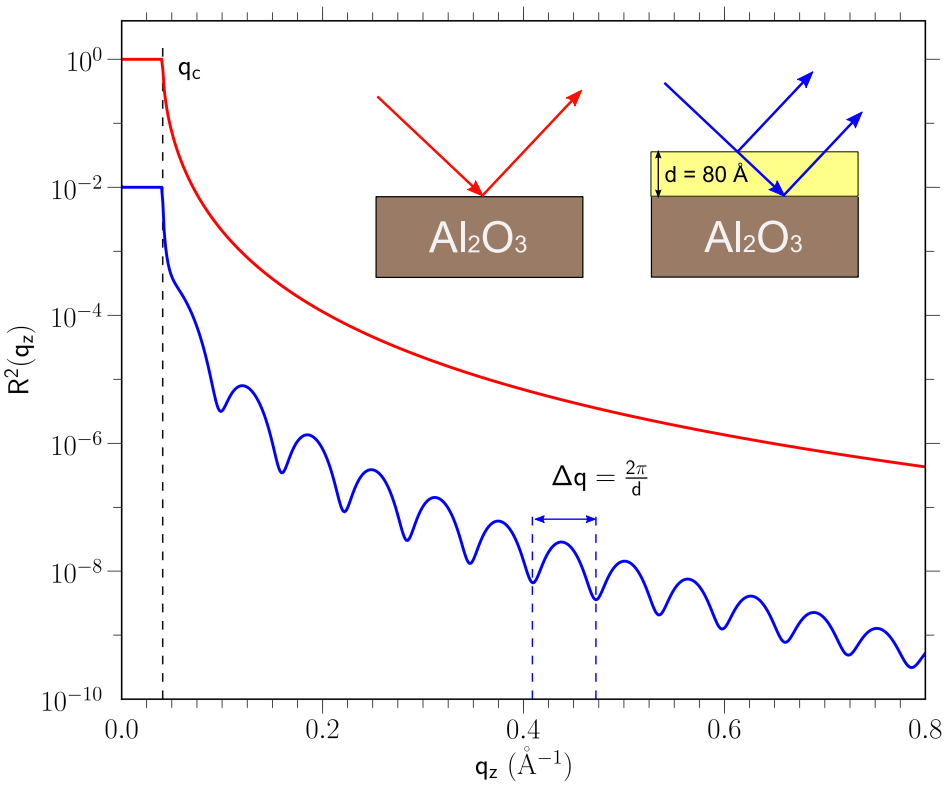

Figure 2.5: Reflection curves calculated within the Parratt formalism from a sapphire substrate with roughness $\sigma_s = 0$ Å (red curve) and from a sapphire substrate with a thin film with thickness $d = 80$ Å and a refactive index smaller than the one of the substrate on top of it (blue curve, shifted by 2 orders of magnitude for clarity). The oscillation period in the reflectivity is related to the film thickness by $\Delta q = 2\pi/d = 0.0785$ Å^{-1}. Sketches of the corresponding slab models are also shown.

2.1.7 Arbitrary profiles

Some density profiles may not fulfill the condition $\sigma_j \ll d_j$. Therefore, they cannot be treated as a multilayer systems consisting of N independent layers. In such cases the profile can be sliced into thin layers of thickness ε with sharp interfaces, each of them with constant refractive index n. Considering that the natural length scale of an atomic profile is given by at least the Bohr radius, the slice thickness was chosen to $\varepsilon = 0.2$ Å in this work. These thin layers can now be treated with the Parratt formalism (see above).

Another approach to treat arbitrary density profiles is the use of the Master formula, which is derived within a kinematical approximation (see Sec. 2.1.8).

2.1.8 Kinematical approximation

Analytical expressions for the reflectivity can be obtained by approximating the full dynamical theory. The advantages of an analytical expression are the straight-forward interpretation of the relation between the density profile and the reflectivity and the reduced numerical effort. A kinematical approximation for the reflectivity is the so-called Master formula:

$$R^2(q) = R_F^2(q)\,|F(q)|^2 \tag{2.17}$$

$$F(q) = \frac{1}{\rho_{-\infty} - \rho_{+\infty}} \int_{-\infty}^{+\infty} \frac{d\rho(z)}{dz} e^{iqz} dz. \tag{2.18}$$

The Master formula neglects multiple reflections at the interfaces. Since multiple reflections are dominant in the vicinity of the critical angle, the region near the total reflection regime is not well-described by the kinematical approximation. Well above the critical angle ($\alpha_i > 3\alpha_c$), the approximation gives a sufficient description of the reflectivity. The deviation in the region of the critical angle can be reduced by taking refraction corrections into account by using a modified wave vector q_z:

$$q_z = 2k \sin \sqrt{\alpha_i^2 - \alpha_c^2}. \tag{2.19}$$

2.2 X-ray reflectivity analysis

The real space electron density profile is related to the x-ray reflectivity from which it can be calculated by solving the Maxwell equations. By measuring the reflection of x-rays one records the intensity $I \propto E^2$ with $E \propto e^{ikz}$ the respective electric field, thus the phase information is missing. Therefore, the corresponding electron density distribution cannot be reconstructed unambiguously from the reflectivity. To overcome this problem, models of the density profile are constructed in which additional knowledge about the invesitgated system, such as bulk density, atomic composition, or generic interfacial structure, has to be included. The missing information can be considered in the model as free parameters. The reflectivity of the model, obtained by the methods discussed in Sec. 2.1, is then fitted to the experimental data in order to determine the free model parameters.

The number of free parameters to be determined by parameter refinement should be limited to about the number of independent features occuring in the experimental reflection pattern to ensure a physically relevant parameter set. More free parameters may lead to better fitting results at the expense of direct physical relevance. In this work, electron density profiles of RTILs, which tend to form layered structures at the interface to the substrate, were investigated. Typical electron density profiles and reflectivities for layered structures are shown in Fig. 2.6. Independent features justifying a free parameter are for example oscillation period, oscillatory strength and decay, position and width of minima and/or maxima, and the overall decay of the reflectivity with respect to the Fresnel reflectivity.

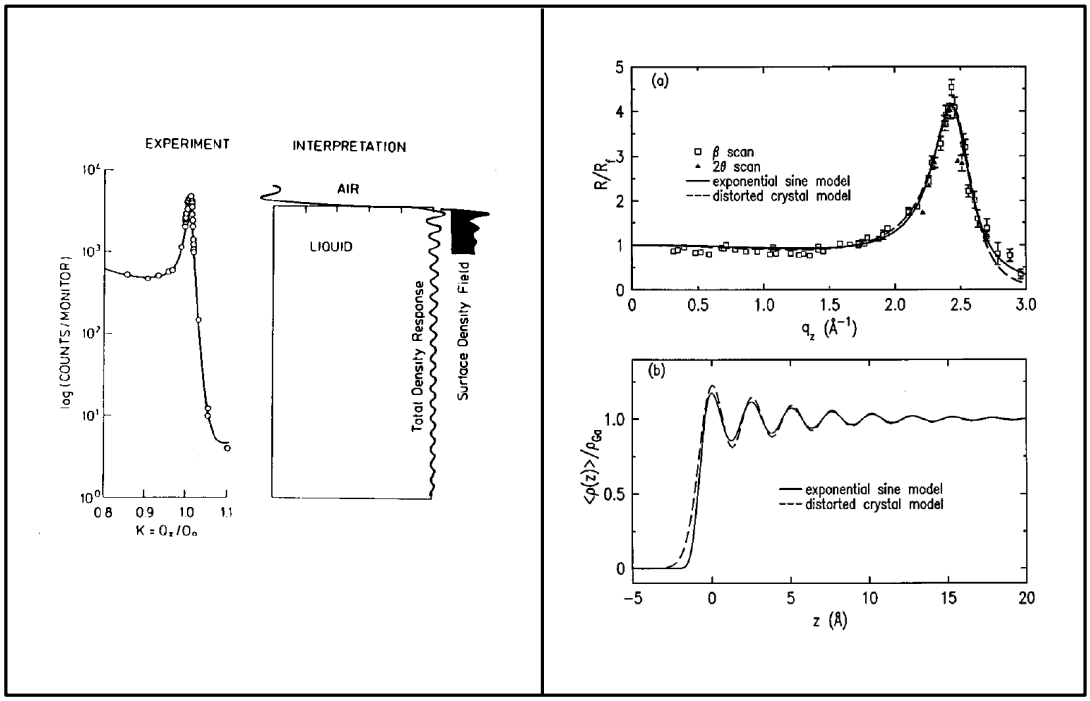

Figure 2.6: Examples of reflectivities resembling layered structures in the corresponding electron density profiles taken from Als-Nielsen [53] (left) and from Regan et al. [54] (right). The left side shows the x-ray reflectivity data from the surface of the liquid crystal 8CB in the nematic phase and the reconstructed electron density profile. The right side shows the normalized x-ray reflectivity data from a liquid gallium surface and the reconstructed electron density profile.

Cost function

The parameter refinement is done by minizing the deviation between the corrected experimental data (see Sec. 3.4.1) and the data calculated from the model as a function of the free parameters. Therefore the best fit of the model is achieved by minimizing the cost function within a numeric algorithm.

A high quality reflectivity curve typically covers a dynamic range of nine orders of magnitude or even more. An adequate scaling of the data allows to consider the low intensity parts (usually for high-q values) with the same weight as the high intensity regime. This is important since information about real space features on small length scales appear in the high-q regime. The dynamic range can be adjusted by dividing the measured reflectivity by the Fresnel reflectivity. The cost function reads then as

$$\chi^2 = \min_{\alpha} M^{-1} \sum_{i=1}^{M} \frac{\left(\alpha I_{i,exp} - I_{i,cal}\right)^2}{R_F^2\left(q_i\right)} \tag{2.20}$$

with $I_{i,exp}$ the experimental data points, $I_{i,cal}$ the calculated intensity points, and a constant scaling factor α to normalize the primary intensity to unity.

Another approach to reduce the dynamic range of the measured reflection intensity employs logarithmic scaling of the data. The cost function becomes then

$$\chi^2 = \min_{\alpha} M^{-1} \sum_{i=1}^{M} (\ln\alpha + \delta_i)^2 \tag{2.21}$$

$$= \min_{\alpha} \left[(\ln\alpha)^2 + 2\ln\alpha \left\langle\delta\right\rangle + \left\langle\delta^2\right\rangle\right] \tag{2.22}$$

$$= \left\langle\delta^2\right\rangle - \left\langle\delta\right\rangle^2 \tag{2.23}$$

with $\delta_i = \ln\frac{I_{i,exp}}{I_{i,cal}}$, and $\ln\alpha = -\left\langle\delta\right\rangle$ as a necessary condition for χ^2 to reach a minimum. This has the advantage that the scaling factor α is not a free fitting parameter but can be obtained directly at each refinement step. To avoid numerical errors, the data is scaled iteratively with the α of the preceding step which results in a small value for $\left\langle\delta\right\rangle^2$ compared to $\left\langle\delta^2\right\rangle$ in the final stage of the refinement.

Numerical algorithm

The global minimum of the cost function in a multi-dimensional parameter space spanned by the free model parameters has to be obtained by a numerical algorithm. Deterministic algorithms are not capable of solving such a problem satisfactory since they can easily be trapped in a local minimum close to given starting parameter values. The use of stochastic Monte Carlo fitting routines is much better suited for reaching the global minimum in such a complex parameter space. They reach every point in the parameter space arbitrarily close. Since only a finite time can be used for the fitting process there is still a non-zero probability to get stuck in a local minimum. In this work the Adaptive Simulated Annealing algorithm developed by Ingber [10, 55] was used.

2.2.1 Semi-quantitative generic layering model

In the following, a semi-quantitative (SQ) approach to a layered electron density profile at the solid-liquid interface is discussed. A generic model for an exponentially damped oscillatory profile is used to describe the density profile on a phenomenological level

without considering the atomistic nature of the system. The corresponding x-ray reflectivity can be calculated analytically in the kinematic approximation. This approach leads to information about the sensitivity of the measurements to certain features in the electron density profile. Therefore, a direct interpretation of particular features of the reflectivity pattern is possible. A more detailed atomic description employing the modified distorted crystal model is discussed in Sec. 2.2.2.

The profile of the SQ model

The SQ model contains only a basic set of arguments to portray the fundamental features of the solid-liquid interface. Five free parameters are used to describe the profile and thus the structure factors of the system, provided that the density of the bulk liquid and solid are known. The physical interpretation of these parameters are the decay length ξ, the layer spacing d_l and the amplitude of the electron density oscillations A, the interfacial substrate roughness σ, and the offset distance d_0.

The profile can be split in two underlying parts, one from the solid wall $\rho_w(z)$ and one from the liquid $\rho_l(z)$:

$$\rho(z) = \underbrace{\rho_w(z)}_{\text{wall}} + \underbrace{\rho_l(z-d_0)}_{\text{liquid}}. \tag{2.24}$$

The hard wall with electron density ρ_s is represented by an error-function interfacial profile smeared out by the surface roughness σ:

$$\rho_w(z) = \frac{\rho_s}{2}\left[1 - \operatorname{erf}\left(\frac{z}{\sqrt{8}\sigma}\right)\right]. \tag{2.25}$$

The liquid at the interface is modeled by an oscillatory profile decaying exponentially to the bulk liquid density ρ_{IL} with a decay length ξ as

$$\rho_l(z) = \rho_{\mathrm{IL}}\Theta(z)\left[1 + Ae^{-\frac{z}{\xi d_l}}\sin\left(\frac{2\pi z}{d_l}\right)\right]. \tag{2.26}$$

$\Theta(z)$ is the Heaviside step function, A an amplitude and d_l the layer spacing. The phase of the sinusoidal layering profile with respect to the wall is given by the offset distance d_0 (see Eq. (2.24)). Figure 2.7 shows an electron density profile created with the SQ model. The model parameters are indicated.

The reflectivity of the SQ model

An analytic expression for the reflectivity $R^2(q)$ of a density profile described by Eqs. (2.24) - (2.26) can be obtained using the Master formula Eq. (2.17), which is a good approximation for scattering angles $\alpha_i = \alpha_f > 3\alpha_c$. The structure factor for the above

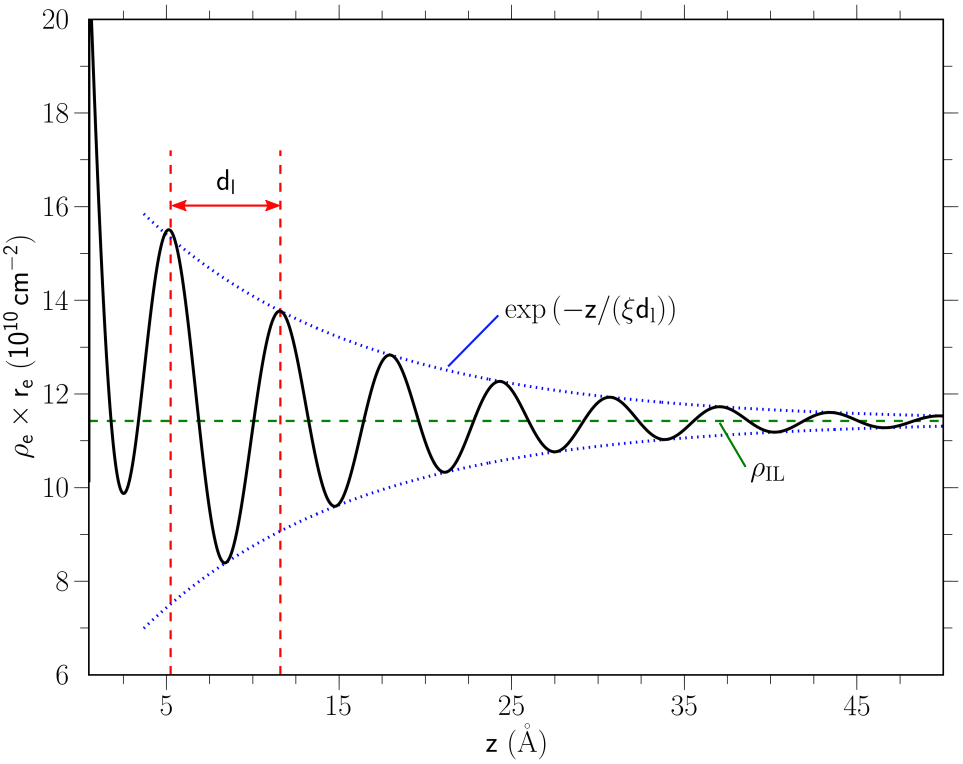

Figure 2.7: Electron density profile created with the SQ model. The parameters are indicated.

model derived via the Master formula is given by

$$F(q) = \underbrace{(1+\rho')e^{-\sigma^2 q^2}}_{\text{wall}} \underbrace{-\rho' e^{-id_0 q}\left[1 + e^{i\phi}\frac{A}{2}\sqrt{L^+ - L^-}\right]}_{\text{liquid}} \tag{2.27}$$

$$\phi(q) = \arctan\left(\frac{q^2 - q_0^2 - \mu^2}{2\mu q}\right) \tag{2.28}$$

$$L^{\pm}(q) = \left[(q \mp q_0)^2 + \mu^2\right]^{-1} \tag{2.29}$$

where $\rho' = \frac{\rho_{IL}}{\rho_s - \rho_{IL}}$ denotes the relative electron density, $q_0 = \frac{2\pi}{d_l}$ and $\mu = \frac{1}{\xi d_l}$. The individual terms of Eq. (2.27) can be assigned to their corresponding features in the real space electron density profile due to the linearity of the Fourier transformation. The Gaussian is associated with the substrate surface component introduced in Eq. (2.25). Increasing surface roughness σ leads to a faster decay of the reflected intensity. The second term accounts for interfacial layering of the RTIL. The exponentially damped sinusoidal profile leads to a Lorentzian contribution to the structure factor. This Lorentzian layering peak is modulated by a complex phase factor determined by the offset distance

d_0 and $\phi(q)$ given in Eq. (2.28). The impact of the offset distance d_0 on the shape of the reflection pattern can be visualized by calculating the reflectivity for different ratios between offset distance and layer spacing. Figure 2.8 shows the modification of the Lorentzian layering peak into a Lorentzian shaped dip as a function of the offset distance normalized by the layer spacing.

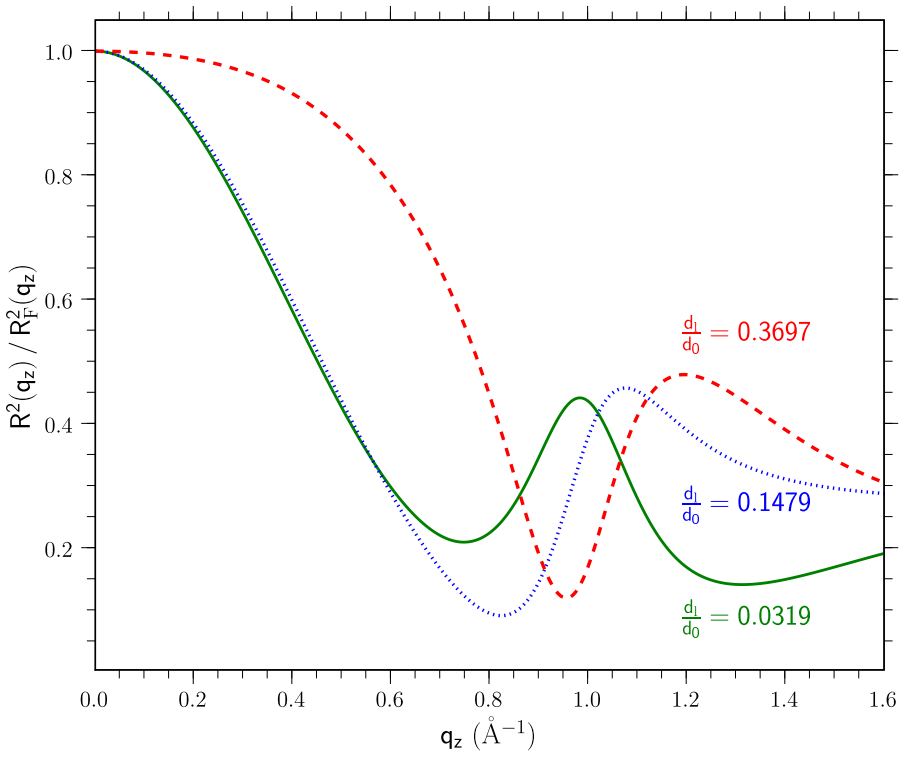

Figure 2.8: Normalized reflectivities with different ratios d_0/d_l calculated via the semi-quantitative layering model.

2.2.2 Distorted crystal model

The distorted crystal model was used successfully in many studies to describe surface-induced layering in single-component liquid metals [56], [54], [57]. A modification of this model, taking into account the binary composition of RTILs, is described in the following.

The modified distorted crystal (DC) model describes a layered density profile along the interface normal via equally spaced layers with Gaussian density distributions. It takes into account the molecular nature of the liquid at the interface. The layering decays with increasing distance from the solid-liquid interface. Charge neutrality is preserved by an alternate layering of the cations and anions. The model conserves the locally

averaged mass and electron density. Starting with a cation layer next to the substrate[1], the electron density profile is parameterized by

$$\rho(z) = (2\pi)^{-1} \sum_{n=0}^{\infty} \left[\frac{\rho_c}{\sigma_n^c} e^{-\frac{1}{2}\left(\frac{d_0+nd_l-z}{\sigma_n^c}\right)^2} + \frac{\rho_a}{\sigma_n^a} e^{-\frac{1}{2}\left(\frac{d_0+(n+\frac{1}{2})d_l-z}{\sigma_n^a}\right)^2} \right] + \rho_s \mathrm{erf}\left(\frac{-z}{\sqrt{2}\sigma_s}\right), \tag{2.30}$$

with d_0 as the distance between the surface of the substrate and the center of the first ion layer. The decay of the layering is described by the Gaussian width $\sigma_n^{c,a}$ which increases with distance from the interface as

$$\sigma_n^{c,a} = \sqrt{(\sigma_0^{c,a})^2 + n\sigma_b^2} \tag{2.31}$$

with $n = 0 \ldots \infty$ as the layer index. The broadening, and thus the decay, is controlled by σ_b. σ_0^a denotes the Gaussian width of the first anion layer and σ_0^c the one for the first cation layer. The widths of the first cation and anion layer incorporate also the interfacial roughness. The area density of the ions is given by $\rho_{c,a} = d_l Z_{c,a} \rho_m N_A / M_{c,a}$ with N_A the Avogadro constant, Z the number of electrons of the respective ion, M its molar mass, ρ_m the molar density, and d_l the periodicity of the layering. The substrate-liquid junction is described by an interfacial error-function profile with an interfacial roughness σ_s and the substrate electron density ρ_s.

The increase of the Gaussian width as described by Eq. (2.31) is also referred to as the full step model incrementing the Gaussian widths every full double layer (comprised of a cation and an anion layer) although both ionic layers within a double layer do not have the same distance from the interface. To account for this difference, the broadening of the ionic layers could be calculated in intermediate steps, i.e. $\sigma_n^c = \sqrt{[(\sigma_0^c)^2 + n\sigma_b^2]}$, $\sigma_n^a = \sqrt{[(\sigma_0^a)^2 + (n+\frac{1}{2})\sigma_b^2]}$, $n = 0 \ldots \infty$. In the following this will be referred to as the half step model. Both models were applied for the analysis of the data in this work.

With known bulk densities (ρ_s and ρ_m) only six parameters are necessary to describe the interfacial density distribution by the DC model. They correspond to the following real space features (see Fig. 2.9): d_l the periodicity of the layering, d_0 the offset distance of the first layer with respect to the wall, $\sigma_0^{c,a}$ the widths of the first ionic double layer, σ_s the substrate roughness, and σ_b incorporating the damped oscillatory decay length ξ.

The reflectivity for the above described density profile composed by the DC model is computed with a parameter refinement method using the Parratt formalism (slice size $0.2\,\text{Å}$; see Sec. 2.1.7) and the Adaptive Simulated Annealing algorithm. Particular features in the reflectivity pattern cannot be assigned to real space quantities in a straightforward manner as within the semi-quantitative model.

One might also introduce an additional asymmetry factor Δ_s for the positioning of different ion layers with respect to each other at the cost of one additional free fitting

[1] Exemplarily the model is discussed in the configuration with the cation layer next to the substrate in the following, since the model in this configuration led to the best fit with the experimental data.

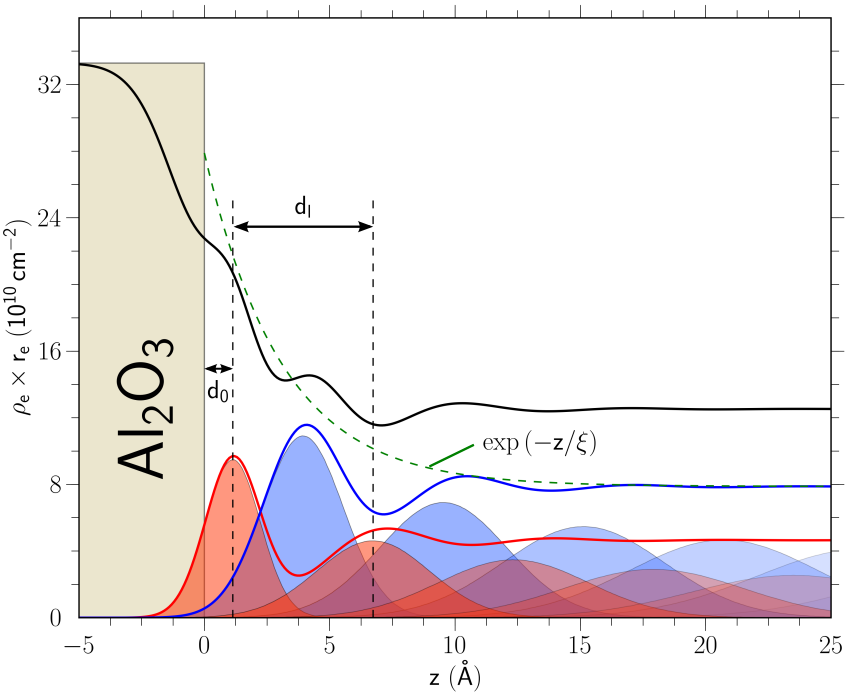

Figure 2.9: Electron density profile represented by the DC model. The parameters are taken from Sec. 4.4.5 Tab. 4.8.

parameter. This is motivated by the possibility that a cation and an anion might assemble into dipolar molecular units. This implies that an anion layer might be closer to one of the neighboring cation layers in the direction vertical to the interface. The parametrization of the electron density profile is then given by (compare Eq. (2.30))

$$\rho(z) = (2\pi)^{-1} \sum_{n=0}^{\infty} \left[\frac{\rho_c}{\sigma_n^c} e^{-\frac{1}{2}\left(\frac{d_0+nd_l-z}{\sigma_n^c}\right)^2} + \frac{\rho_a}{\sigma_n^a} e^{-\frac{1}{2}\left(\frac{d_0+(n+\frac{1}{2})d_l-\Delta_s-z}{\sigma_n^a}\right)^2} \right] + \rho_s \mathrm{erf}\left(\frac{-z}{\sqrt{2}\sigma_s}\right). \tag{2.32}$$

2.3 Bulk liquid scattering

The liquid state of matter is comprised of highly disordered molecules compared to the solid phase. Thus, only short-range order is found in liquids. This short-range structure can be described within the concept of the radial distribution function $g(r)$. It is a measure of the number of molecules surrounding an arbitrarily chosen molecule at any distance r and can be obtained experimentally by analyzing the intensity distribution of x-rays or neutrons scattered by the liquid.

X-ray scattering experiments probe the differential scattering cross-section $\frac{d\sigma}{d\Omega}$ reflecting the electron density distribution in a sample. Employing the first Born approxi-

mation yields

$$I(q) \approx \frac{d\sigma}{d\Omega} = \left\langle \left| \sum_{k=1}^{N_e} r_0 \exp(i\mathbf{q} \cdot \mathbf{r}_k) \right|^2 \right\rangle \tag{2.33}$$

with r_0 as the Thomson scattering length, N_e the number of electrons in the sample, $\mathbf{r}_k$ their positions, and $\mathbf{q}$ the momentum transfer for the scattering process. Equation (2.33) can be separated into contributions from individual molecules (self-scattering) and intermolecular correlations $S(q)$. Assuming that the scattering arises from independent neutral atoms with spherical electron density distributions (Debye approximation), the scattered intensity from a liquid is given by

$$I(q) \approx \sum_{ij} x_i x_j f_i(q) f_j(q) \frac{\sin qr_{ij}}{qr_{ij}} + \sum_{i \leq j} x_i x_j f_i(q) f_j(q) S_{ij}(q) \tag{2.34}$$

with x_i the atomic fraction of atom type i, $f_i(q)$ the q-dependent atomic scattering factor for atom type i, and r_{ij} the intramolecular distance between atom centers. The intermolecular correlations are specified by the relation

$$S_{ij}(q) = 1 + 4\pi\rho \int_0^\infty r^2 dr \left[g_{ij}(r) - 1 \right] \frac{\sin qr}{qr} \tag{2.35}$$

with ρ the atomic number density, and $g_{ij}(r)$ the partial radial distribution function between atom types i and j.

In order to apply the above equations and to obtain distribution functions comparable with other experiments, some corrections have to be applied to the measured intensity. The background arising from the sample chamber, air scattering, or backscattering from parts in the experimental hutch needs to be subtracted. Corrections for the used detector type and geometry (especially for 2D flat field detectors) have also to be considered (for details see Sec. 3.5). The absorption of the intensity depends on the path length of the x-rays in the sample. The path length $\tau(x, \alpha) = d - x(1 - \frac{1}{\cos 2\alpha})$ depends on the sample thickness d, the scattering angle 2α and on the position of the scattering event x (see Fig. 2.10). Therefore, the correction factor for the absorption is obtained by integration over all possible path lengths for each scattering angle [58], yielding

$$A(\alpha) = \frac{\int_0^d \exp\left[-\mu\tau(x,\alpha)\right] dx}{\int_0^d dx} \tag{2.36}$$

$$= \frac{\exp\left(-\mu d\right)}{\mu d \left(\frac{1}{\cos 2\alpha} - 1\right)} \left\{ 1 - \exp\left[-\mu d \left(\frac{1}{\cos 2\alpha} - 1 \right) \right] \right\} \tag{2.37}$$

with μ as the linear attenuation coefficient. The polarization of the incident beam requires also a correction. For unpolarized radiation, the correction is given by $P = \frac{1}{2}(1 + \cos^2\theta)$. In the case of polarized radiation from an accelerator-based x-ray source, the latter is replaced by

$$P = P_{\mathrm{i}}[1 - (\sin\phi \sin\theta)^2] + P_{\mathrm{o}}[1 - (\cos\phi \sin\theta)^2] \tag{2.38}$$

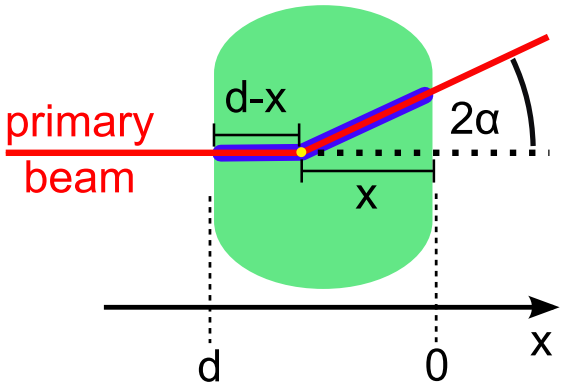

Figure 2.10: The absorption depends on the path length through the liquid sample, whereas the path length depends on the scattering angle and the x position of the scattering event.

with the fractional polarizations of the beam in the plane P_{i} and out of the plane P_{o} of the circulating electrons. Multiple scattering events contain no information on the intermolecular correlations and must be removed from the measured intensities. The probability of multiple scattering events increases with sample thickness. The ratio of multiple scattering to primary scattering is about $1\,\%$ for samples with a product of linear attenuation coefficient and sample thickness $\mu t \approx 0.1$ [59, 60]. Incoherent scattered intensity due to the Compton effect contains also no information on the correlations present in the liquid. The Compton scattering occurs as a q-dependent signal. The standard Compton formula is given by

$$\lambda_f = \lambda_i + \frac{h}{m_e c}\left(1 - \cos\theta\right) \tag{2.39}$$

with $\frac{h}{m_e c} = 2.4263 \cdot 10^{-12}\,\mathrm{m}$ as the Compton wavelength of an electron (obtained from NIST [61]). The energy loss due to the Compton effect can be approximated for small scattering angles by

$$\Delta E \approx \frac{dE}{d\lambda}\Delta\lambda \approx -\frac{\hbar^2}{4m_e}q^2 \tag{2.40}$$

with $m_e = 9.1093826 \cdot 10^{-31}\,\mathrm{kg}$ the electron mass, $\hbar = 1.054571628 \cdot 10^{-34}\,\mathrm{Js}$ the Planck constant over 2π, and q the modulus of the momentum transfer.

The specific correction factors used for the experiments performed in this work are discussed in Sec. 3.5.

Chapter 3

Experimental details

In this chapter, the beamline for the x-ray scattering experiments, the sample chamber, the sample preparation process, some details about the reflectivity measurements, and the bulk liquid scattering experiments are described.

3.1 The beamline ID15A at ESRF

The x-ray reflectivity experiments presented in this work were all carried out at the high energy beamline ID15A at the European Synchrotron Radiation Facility (ESRF) in Grenoble, France. The beamline is optimized for the production of high energy x-rays in the range between $40\,\mathrm{keV}$ and $300\,\mathrm{keV}$. A schematic layout of the beamline is shown in Fig. 3.1. The main components of the beamline setup are the source, the optics and focusing device, the diffractometer and the detector. These components are briefly discussed in the following.

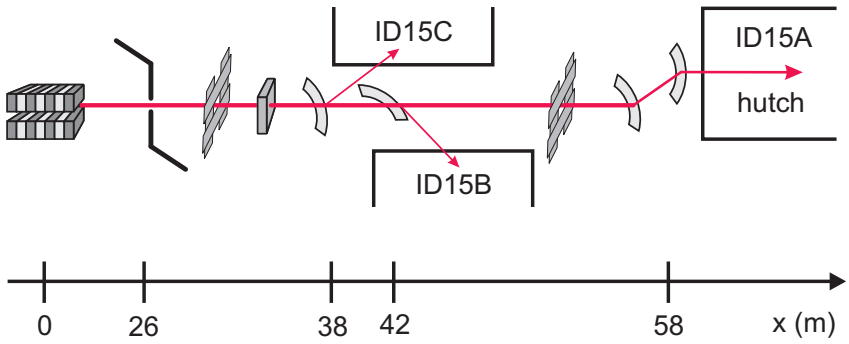

Figure 3.1: Schematic layout of the high energy beamlines ID15A, ID15B, and ID15C (see Ref. [51]).

3.1.1 Source

The x-ray source of ID15A is a 7 period asymmetric wiggler with a critical energy of $44.1\,\mathrm{keV}$, a minimal gap size of $20.6\,\mathrm{mm}$, and a magnetic field of $1.84\,\mathrm{T}$. Permanent filters ($0.7\,\mathrm{mm}$ C, $4.0\,\mathrm{mm}$ Be, $4.1\,\mathrm{mm}$ Al), which are installed directly after the front end, reduce the heat load on the crystal optics. The filters surrpress photons with an energy less than $40\,\mathrm{keV}$. The maximum brightness of $3.3{\cdot}10^{14}\,\mathrm{photons\,mrad^{-2}\,0.1\,\%\,bw^{-1}}$ per $100\,\mathrm{mA}$ ring current is reached at an energy of $50\,\mathrm{keV}$. At $70\,\mathrm{keV}$ used in these experiments, the brightness decreases to approximately $2.8 \cdot 10^{14}\,\mathrm{photons\,mrad^{-2}\,0.1\,\%\,bw^{-1}}$ per $100\,\mathrm{mA}$.

3.1.2 Optics and focusing device

The monochromator consists of two asymmetrically cut and bent Si(111) crystals in fixed exit geometry. The energy resolution of $\Delta E/E = 2.3 \cdot 10^{-3}$ is determined by the asymmetric cut of $37.76\,^\circ$ with respect to the (111)-orientation. The horizontal divergence of the beam is reduced by bending the crystals.

Focusing of the beam at the sample position is achieved by a compound refractive lens (CRL) consisting of 150-200 single aluminum concave lenses [62]. The size of the beam at the sample position can be determined by knife edge scans where a sharp edge of a knife blade is scanned across the beam. For a Gaussian beam profile such scans yield an error function intensity curve, from which the beam size in the scan direction can be obtained. Figure 3.2 shows a vertical and a horizontal beam profile obtained with knife edge scans. By fitting the measured profiles the beam size was obtained. The vertical beam size in the experiments was between $6\,\mu\mathrm{m}$ and $8\,\mu\mathrm{m}$. The horizontal beam size was approximately $26\,\mu\mathrm{m}$.

3.1.3 The HEMD setup

The High Energy Micro Diffraction (HEMD) setup developed in our group is a permanent installation in the ID15A experimental hutch [9]. It allows structural investigations of deeply-buried interfaces as well as of free surfaces. The use of high energy x-rays leads to very small scattering angles. Therefore, a high precision diffractometer is essential. The six circle HEMD diffractometer achieves a high angular accuracy for the incident ($< 20\,\mu\mathrm{rad}$) and exit diffractometer angle ($< 10\,\mu\mathrm{rad}$). Also the sample position can be controlled very precisely in the vertical ($< 1\,\mu\mathrm{m}$) and horizontal ($1\,\mu\mathrm{m}$) direction.

3.1.4 Detectors

For detecting x-rays three Eurisys Si PIN diodes were used in the high intensity regime and for monitoring the incident beam. For single photon counting a scintillation counter served as a detector.

The PIN Diodes absorb approximately 10 % of the incident beam intensity at an energy of $70\,\mathrm{keV}$. The high internal gain of Silicon leads to an approximately 10 times

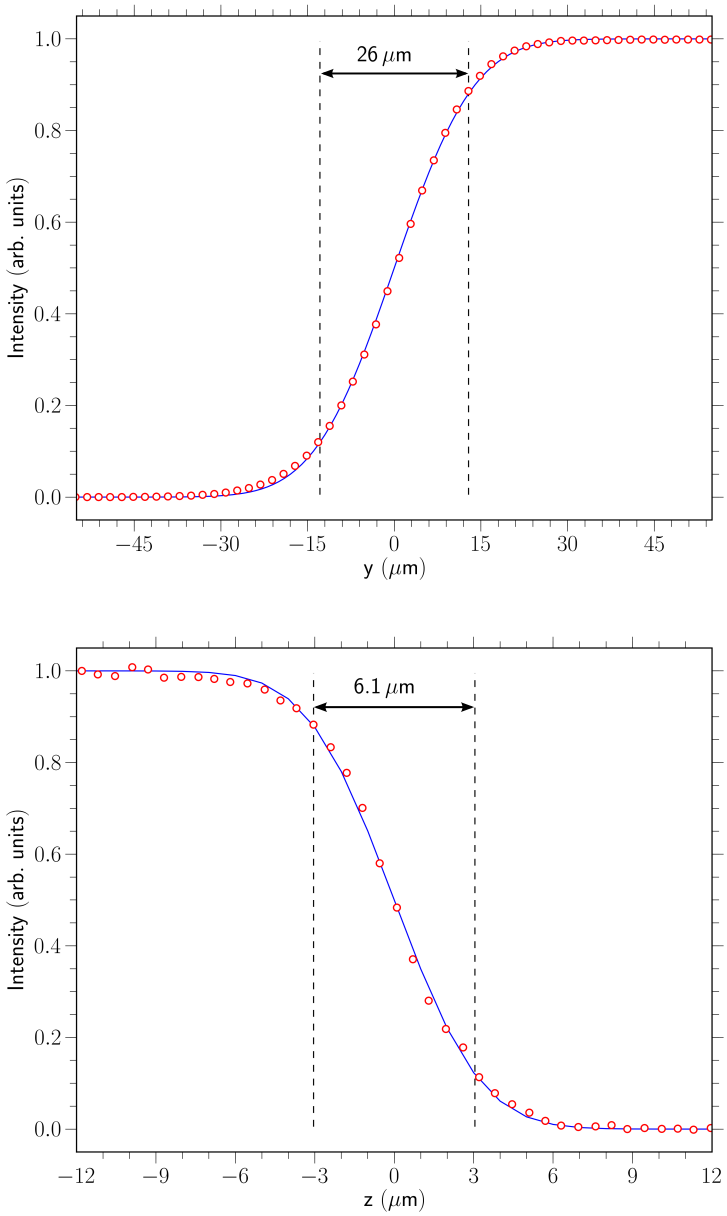

Figure 3.2: Vertical (top) and horizontal (bottom) x-ray beam profile measured with knife edge scans. The vertical dashed lines indicate the FWHM of the beam profiles according to a fit (blue lines) assuming a Gaussian beam profile.

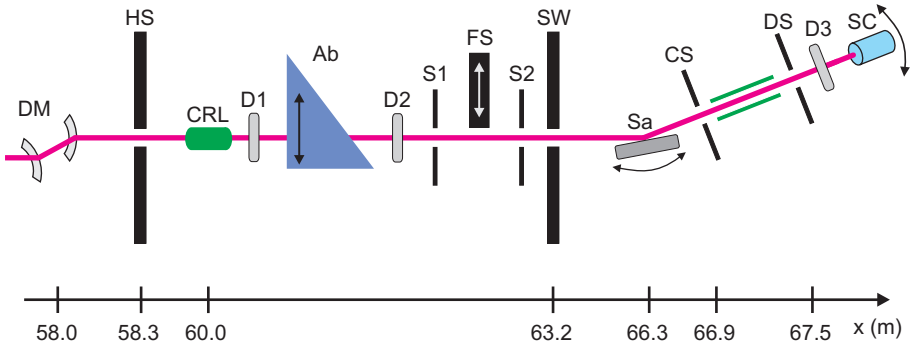

Figure 3.3: X-ray optical elements and beamline setup for high energy reflectivity experiments at ID15A, ESRF. (DM) double crystal monochromator in Laue geometry; (HS) wall of the experimental hutch ID15A; (CRL) compound refractive lens; (D1) primary beam monitor diode; (Ab) absorber wedge with absorption path $d = 0 \ldots 60\,\mathrm{cm}$; (D2) second monitor diode; (S1) first slit set; (FS) fast shutter; (S2) second slit set; (SW) shielding wall; (Sa) sample position; (CS) collimator slits; (T) flight tube; (DS) detector slits; (D3) detector diode; (SC) scintillation counter (CyberStar, Oxford-Danfysik).

larger electronic signal compared to ionization chambers (one photon with an energy of $70\,\mathrm{keV}$ absorbed in the diode will create almost 20000 electron-hole pairs). The absolute flux N_{ph} can be calculated from the measured diode current I_{PIN} by

$$N_{ph} = \frac{I_{PIN} E_g}{eE}(1 - e^{-\mu_{en} t})^{-1}. \tag{3.1}$$

$E_g = 3.6\,\mathrm{eV}$ denotes the average energy for the excitation of an electron hole pair by photoabsorption, t the diode thickness, and μ_{en} the energy absorption coefficient. The effective dynamic range of the detector diode is approximately five orders of magnitude [51].

For the scintillation counter a $5\,\mathrm{mm}$ thick NaI crystal was used. The conversion efficiency for photons with an energy of $70\,\mathrm{keV}$ is more than $99\,\%$. In order to increase the dynamic range of the scintillation counter, the measured count rates have been corrected for deadtime, and a PMMA (Polymethyl methacrylate) absorber was used. The deadtime correction factor for count rates well below the saturation level of the detector can be approximated by

$$N_{corr} = \frac{N}{(1 - N\tau)}. \tag{3.2}$$

with $\tau = 0.68\,\mu\mathrm{s}$ the deadtime constant [51]. The count rates in the experiments were limited to $150000\,\mathrm{cps}$ to ensure a deadtime correction always less than $10\,\%$.

3.1.5 Absorber

The dynamic range of the scintillation counter was limited to $150000\,\mathrm{cps}$. However, the dynamic range of the reflectivity measurements performed in this work spans 9 orders of magnitude. Using a Polymethyl methacrylate (PMMA) absorber the accessible dynamic

range of the scintillation counter can be increased by attenuating the beam at high intensities. The use of PMMA as absorber material avoids the problem of beam hardening for absorption factors down to 10^{-5} (see Ref. [51]).

3.2 Sample chamber

The sample chamber used for the experiments in this work was designed for reflectivity measurements at solid-liquid interfaces. The chamber can be evacuated to a pressure of approximately $10^{-6}\,\mathrm{mbar}$. The accessible temperature range is $-120\,^{\circ}\mathrm{C}$ to $+250\,^{\circ}\mathrm{C}$. All materials of the chamber in direct contact with the sample environment are inert and easy to clean in order to prevent contamination of the sample with impurities.

The main parts of the chamber are a copper socket with a glass cell on top of it. The two parts are connected via a KF flange. Conical shaped window holders are fused into the glass cell, one at the front and one at the back. As window material Mylar was used. The glass cell contains additional KF flanges which can be used for connecting e.g. a vacuum pump, a ventilation valve, and a tube to purge the cell with inert gas.

The copper part contains the heating device, the cooling mechanism and a Pt100 temperature sensor. On top of the copper socket a stainless steel sample holder is mounted (see Fig. 3.6 bottom). The sample holder can easily be exchanged and cleaned. Heating is achieved by four cartridges which are placed symmetrically inside the copper part. Each cartridge has a heating power of $200\,\mathrm{W}$. The whole setup can be heated with a maximum power of $800\,\mathrm{W}$. Cooling is achieved by flowing a cooling liquid or gas through the copper part. In the experiments described in this work nitrogen gas, which was cooled by heat exchange in liquid N_2, was used.

All PTFE gaskets, glass and stainless steel parts of the chamber were cleaned before every application by immersing them in an alkaline detergent in an ultrasonic bath. Afterwards they were rinsed with pure water and dried in an oven. The copper part was immersed in a solution of acetic acid and hydrogen peroxide for $30\,\mathrm{min}$. Subsequently the copper part was thouroughly rinsed with pure water and dried in an oven.

Temperature control and accuracy

The temperature of the sample was controlled via a Pt100 resistive temperature sensor. The sensor was located in the copper part about $1\,\mathrm{cm}$ below the sample in vertical direction and therefore outside of the chamber atmosphere. In order to estimate the actual sample temperature T_s, a second Pt100 resistive sensor was placed first inside of the stainless steel sample holder and second on top of the sample holder.

The temperature offset between the control sensor (inside the copper part) and the one inside the sample holder depends also on the residual pressure inside the chamber. Figure 3.5a shows the offset for ambient pressure which is almost constant for the entire temperature range, and for a pressure of about $10^{-5}\,\mathrm{mbar}$. Figure 3.5b shows the offsets between the control sensor and the sensor inside the sample holder, and the sensor on top of the sample holder. The latter data was used to obtain an analytical expression for

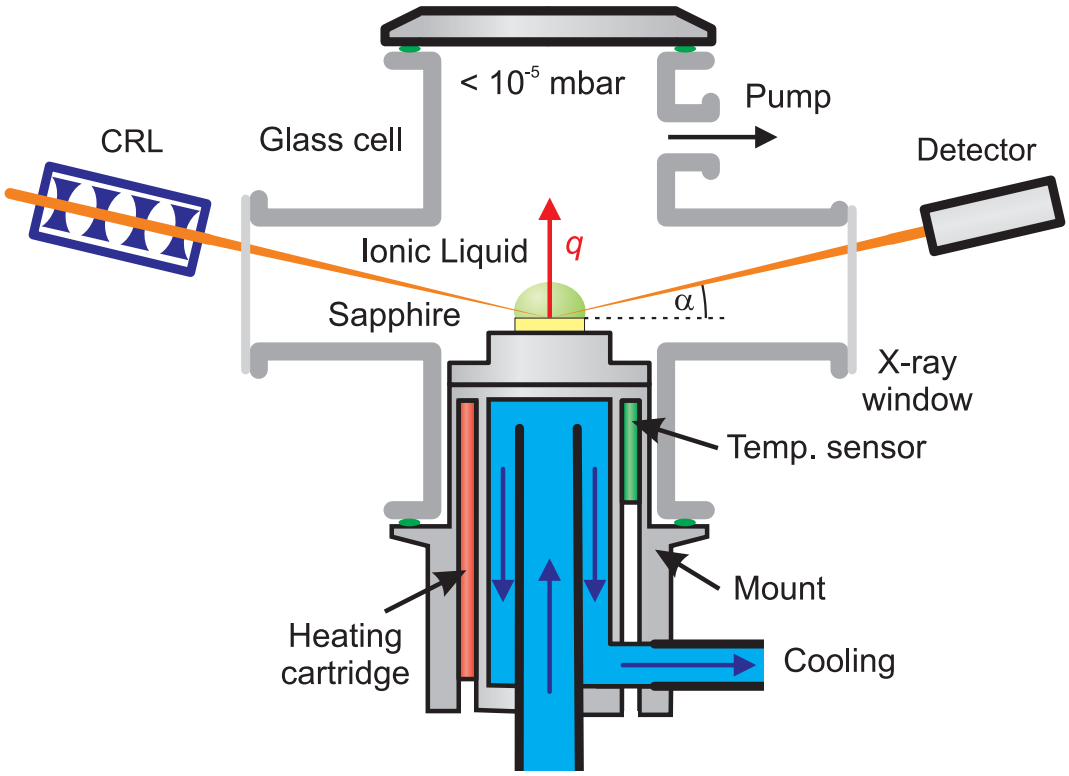

Figure 3.4: Sketch of the sample chamber used in the x-ray reflectivity experiments of this work taken from Ref. [63]. The different parts are indicated.

the temperature offset by fitting a linear function:

$$\Delta T(T_c) = 0.0916 \cdot T_c - 1.4783 \tag{3.3}$$

with T_c the control temperature in degrees Celsius. The sample temperature T_s is obtained by subtracting the offset from the control temperature $T_s = T_c - \Delta T$.

Errors of the offset measurements are caused by the sensor inaccuracy (manufacturer specification: $\pm 0.1\,\mathrm{K}$) and fluctuations in the cooling power, i.e. the nitrogen flow. The impact of the latter was estimated to be about $\pm 0.3\,\mathrm{K}$.

All sensor measurements were performed using the Kelvin (4-wire) method to avoid systematic errors caused by wire resistance. For temperature measurement and control a Lakeshore model 331 was used. A power supply, delivering the current for the heating cartridges, served as amplifier of the controller signal. The use of the PID control algorithm with manually adjusted values resulted in a high temperature stability of the sample environment ($\pm 5\,\mathrm{mK}$). The temperature was logged during all the experiments via a serial connection between the temperature controller and a personal computer. The acquisition of the temperature history was programmed in the development environment Labview.

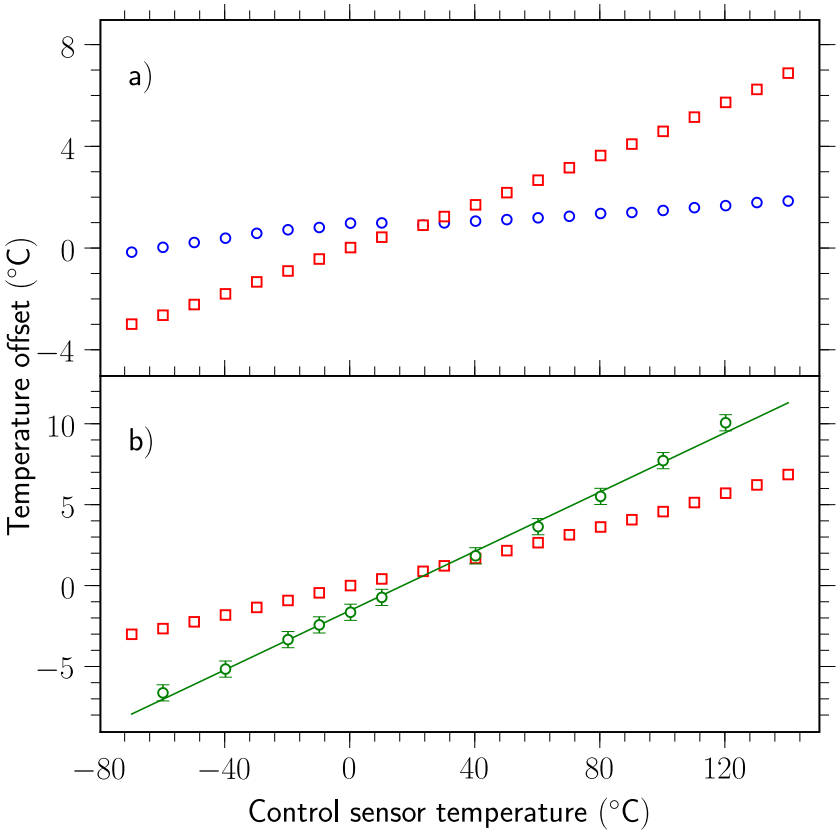

Figure 3.5: (a) Offset between the control temperature and the temperature inside the sample holder at ambient pressure (circles) and a pressure of 10^{-5} mbar (squares) inside the chamber. (b) Offsets between the control temperature and the temperature inside the sample holder (squares) and the actual sample temperature (circles), respectively, both at a pressure of 10^{-5} mbar inside the chamber.

3.3 Sample preparation

The following sections elaborate on the preparation and the cleaning procedures of the RTILs and the sapphire substrates.

The room temperature ionic liquids were all obtained from Merck in high purity grade (water content $< 100\,\mathrm{ppm}$, chloride content $< 100\,\mathrm{ppm}$). In order to remove volatile residues, the RTILs were dried for $24\,\mathrm{h}$ at $80\,^{\circ}\mathrm{C}$ at a pressure of $1\,\mathrm{mbar}$.

Sapphire substrates were used as model system for a hard wall. Sapphire has the advantage of being chemically inert and being commercially available with a surface roughness of $< 0.3\,\mathrm{nm}$. The small roughness allows to access a large q-range in the x-ray reflectivity experiments.

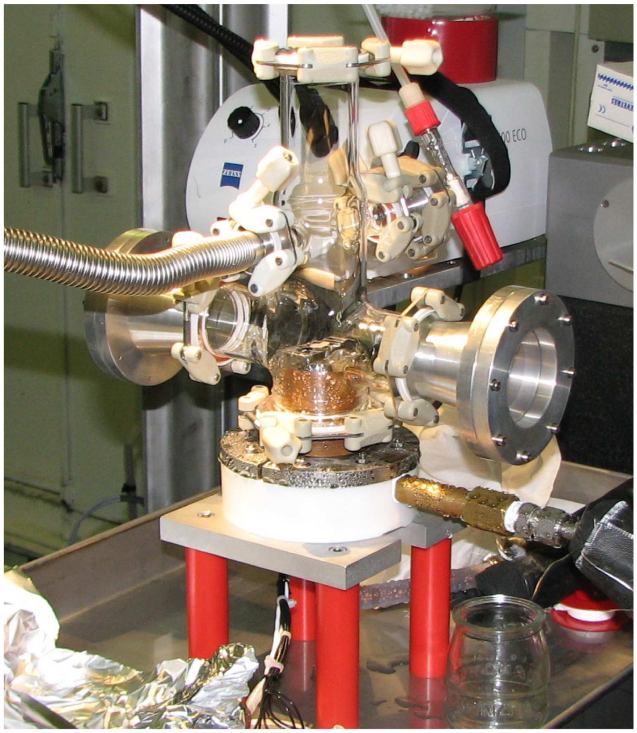

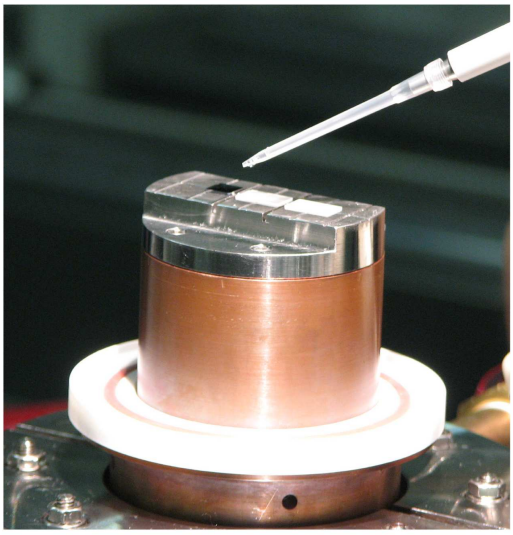

Figure 3.6: Pictures of the sample chamber mounted on the HEMD diffractometer (top) and of the copper socket with the stainless steel sample holder. One silicon and two sapphire substrates are placed on top (bottom).

The sapphire wafers (thickness $400\,\mu\mathrm{m}$, (0001) orientation), purchased from Saint-Gobain Crystals, were cut in pieces with a size of $10\,\mathrm{mm} \times 6\,\mathrm{mm}$.

The sapphire substrates were cleaned with a sequence of different solvents to remove residues of RTILs from previous experiments and contaminations from the ambient environment. First, the samples were immersed in acetonitrile for $15\,\mathrm{min}$ in an ultrasonic bath mainly to remove residues of RTILs (all RTILs used in this work are soluble in acetonitrile). Then the samples were placed in isopropanole, acetone and chloroform for $15\,\mathrm{min}$ each in an ultrasonic bath. Afterwards the samples were etched in freshly prepared piranha solution ($\mathrm{H_2SO_4}$ $98\,\%$ and $\mathrm{H_2O_2}$ $36\,\%$ in $3:1$ ratio) for $1\,\mathrm{min}$. Its strong oxidizing tendency leads to removal of traces of organic contaminants and to hydroxylation of the samples. After the piranha etch the samples were thoroughly rinsed with pure water and subsequently blown dry in a jet of pure Argon gas. Finally, the sapphire samples were treated with UV light irradiation ($\lambda = 172\,\mathrm{nm}$, BlueLight Excimer Compact Source, $20\,\mathrm{W}$ electric, irradiance $50\,\mathrm{mWcm^{-2}}$; Heraeus Noblelight, Hanau) in an oxygen atmosphere for $30\,\mathrm{min}$. The UV light/ozone treatment removes covalently bonded hydrocarbons from the sapphire surface and oxidizes them to $\mathrm{CO_2}$ and $\mathrm{H_2O}$. This mechanism leads to a more hydrophilic surface, resulting in complete wetting with water as opposed to non-wetting before the cleaning. The UV light/ozone treatment was applied just before the experiment because of the decrease of hydrophilicity in time as shown by Luo and Wong [64]. In the following, a brief summary of the cleaning procedure for the sapphire substrates is given:

1. Immersion in solvents for $15\,\mathrm{min}$ each in an ultrasonic bath: acetonitrile, isopropanole, acetone, chloroform.

2. Etching in piranha solution for $1\,\mathrm{min}$.

3. Thorough rinsing with pure water.

4. Drying in a jet of pure Ar gas.

5. UV light treatment in an oxygen atmosphere for $30\,\mathrm{min}$.

In order to determine the spatially averaged surface roughness (FWHM) of the sapphire substrates, the x-ray reflectivities of the corresponding substrates in vacuum were measured. The same setup as for the other reflectivity experiments in this work was used, and the measurements were performed at the beamline ID15A, ESRF. For a dry substrate in vacuum the Master formula (see Sec. 2.1) yields $R^2(q_z) \,/\, R_\mathrm{F}^2(q_z) = \exp(-\sigma_s^2 q_z^2)$. Therefore, the roughness of the substrate can be obtained from the slope of the plot $\ln\left(R^2(q_z) \,/\, R_\mathrm{F}^2(q_z)\right)$ vs. q_z^2 (see Fig. 3.7). Due to alignment problems in the low-q regime, and since the Master formula is only a good approximation above the critical angle, only the high-q range has been used for determining the substrate roughness. For both substrates a spatially averaged roughness of $\sigma_s = 1.9\,\mathrm{\AA}$ was retrieved.

In a typical experiment, a cleaned sapphire substrate was mounted in the chamber which has been heated up to $120\,^\circ\mathrm{C}$. Then the chamber was closed and a vacuum was applied for a few minutes to remove the moisture which may have been adsorbed to the

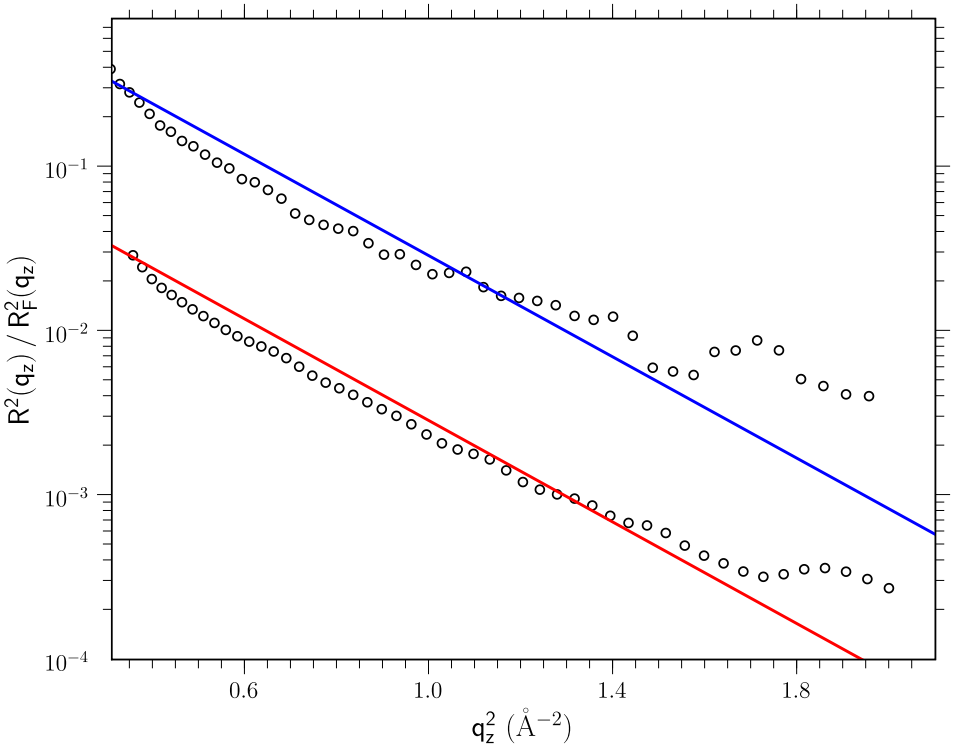

Figure 3.7: Normalized reflectivity from two different sapphire substrates in vacuum. Since roughness attenuates the measured intensity according to $\exp(-\sigma_s^2 q_z^2)$, the roughness for both substrates yields $\sigma_s = 1.9\,\text{Å}$.

substrate. Subsequently the chamber was opened and a $10\,\mu$l droplet of the RTIL of interest was placed on top of the substrate with a pipette. After closing the chamber and applying a vacuum, the temperature was adjusted.

3.4 Reflectivity measurements

The reflectivity curves were measured up to a maximum vertical momentum transfer of $q_{max} = 1.5\,\text{Å}^{-1}$. Since the reflected intensity decreases almost 10 orders of magnitude in this momentum transfer range, it was necessary to measure the whole reflectivity curve in several scans covering smaller q-ranges with different absorber settings. Overlap between neighboring scans allowed identification of misalignment and enabled better adjustment of the different scans to a continuous curve. The data in the q-region of interest was measured by two scans which have been shifted against each other by half the step size. In order to reduce the beam-induced damage of the RTILs by the x-ray radiation a fast shutter was used. The shutter was configured such that it opened $0.2\,\text{s}$ before every counting command. The horizontal translation of the sample of about $1.0\,(\text{mm}/\text{Å}^{-1})$ during every measurement minimized the radiation damage even further.

Table 3.1: Summary of the experimental parameters for the reflectivity experiments.

parameter	value
x-ray wavelength λ	$0.171\,\text{Å}$
wavelength spread $\Delta\lambda/\lambda$	$2.3 \cdot 10^{-3}$
primary beam intensity	$5 \cdot 10^{10}\,\text{photons}\,\text{s}^{-1}$
vertical detector slit opening	$350\,\mu\text{m}$
horizontal detector slit opening	$350\,\mu\text{m}$
vertical beam size b_v	$6\,\mu\text{m}$ - $8\,\mu\text{m}$
horizontal beam size b_h	$26\,\mu\text{m}$
distance sample-detector	$1196\,\text{mm}$
maximum vertical momentum transfer q_{max}	$1.5\,\text{Å}^{-1}$
sample length d	$6\,\text{mm}$

3.4.1 Data correction

Footprint correction

At very grazing incident angles α_i, the interface (length d along the incident beam direction) is almost parallel to the beam so that a fraction of the incoming beam (vertical width b_v) does not illuminate the interface and can therefore not be reflected. This has to be corrected by applying a footprint correction to the raw data. For a Gaussian beam profile the footprint correction is given by

$$f_{\text{fp}} = \text{erf}\left(\frac{d\sin\alpha_i}{8\sqrt{(\ln 2)}b_v}\right). \tag{3.4}$$

For more elaborate explanations and derivations see references [45, 65].

Normalization

The intensity of the incident beam was monitored with a PIN diode. The intensity varies in time, mainly because of the decreasing storage ring current between injections and temperature changes of the monochromators. To eliminate these fluctuations, all measured intensities have been normalized to the incident beam intensity.

Due to the limited dynamic range of the detectors the different parts of a reflectivity curve were measured with different absorber settings. Each section of the reflectivity curve was corrected for absorption before merging all sections into a continuous curve. Furthermore, the data were multiplied by a scaling factor since the measured reflectivity is only proportional to the absolute reflectivity.

Background subtraction

The measured reflectivity consists of the specular reflectivity and diffuse scattered background. The latter can arise by scattering from air, optical elements and most import the bulk liquid. It was measured by detuning the incident angle α_i by $+0.03\,^\circ \gg \Delta$, with Δ the width of the specular reflected beam. If the reflectivity and the background are measured on coinciding $q_z-\mathrm{values}$, the background can be eliminated by pointwise subtraction of the two scans. However, in most cases the reflectivity and the background were measured with different q_z steps. Therefore a regriding routine was applied to the data to obtain data points for the reflectivity and the background at the same $q_z-\mathrm{values}$. The routine determines the intensity at each q_z position by weighting the contribution of neighboring data points with a Gaussian distribution centered at that q_z point. For more details see [29].

3.5 Bulk liquid scattering measurements

The bulk liquid x-ray scattering experiments were performed with the same setup used for the x-ray reflectivity measurements (see Sec. 3.2) at the beamline ID15A, ESRF. The measurements were performed on a liquid droplet (approximately $10\,\mu\mathrm{l}$) placed on a silicon substrate ($5\,\mathrm{mm} \times 5\,\mathrm{mm}$) which was mounted in the sample chamber for the reflectivity measurements. The x-ray beam was horizontally positioned in the middle of the substrate and was penetrating the droplet $50\,\mu\mathrm{m}$ above the substrate-liquid interface. The horizontal momentum transfer was varied up to $q = 2\,\mathrm{\AA}^{-1}$ for the measurements of the bulk liquid scattering. The experimental parameters are summarized in Tab. 3.2.

Table 3.2: Summary of the experimental parameters for the bulk liquid scattering experiments.

parameter	value
x-ray wavelength λ	$0.171\,\mathrm{\AA}$
wavelength spread $\Delta\lambda/\lambda$	$2.3 \cdot 10^{-3}$
primary beam intensity	$5 \cdot 10^{10}\,\mathrm{photons\,s^{-1}}$
vertical detector slit opening	$4\,\mathrm{mm}$
horizontal detector slit opening	$1\,\mathrm{mm}$
vertical beam size b_v	$6\,\mu\mathrm{m}$ - $8\,\mu\mathrm{m}$
horizontal beam size b_h	$26\,\mu\mathrm{m}$
distance sample-detector	$1196\,\mathrm{mm}$
maximum vertical momentum transfer q_{max}	$2.0\,\mathrm{\AA}^{-1}$
data resolution	$0.016\,\mathrm{\AA}^{-1}$
counting time	$5\,\mathrm{s\,point}^{-1}$
sample length d	$6\,\mathrm{mm}$
droplet volume	$10\,\mu\mathrm{l}$

The measured intensity has to be corrected for several effects, which could otherwise lead to a misinterpretation of the data (see Sec. 2.3). First, the intensity was normalized to the incident beam intensity monitored by a PIN diode. The background from the experimental hutch (scattering from shieldings, optics, slits) and of the chamber was determined by measuring the scattered intensity with the empty sample chamber. No significant background was measured.

A geometric correction was applied since the detector follows the horizontal momentum transfer not by moving on a circle with the sample as center. Figure 3.8 shows a sketch of the detector geometry. The detector moves perpendicular to the incident beam along a straight line and performs a rotation such that the scattered beam is always perpendicular to the detector slits. This leads to an increase of the detector-sample distance with increasing scattering angle resulting in an intrinsic decrease of the measured intensity. The detector area (horizontal $\times$ vertical detector slit opening) records the scattered intensity which lies in the solid angle spanned by the detector area and the sample as origin. Since the sample-detector distance increases, whereas the detector area is constant with increasing scattering angle, the solid angle decreases (see Fig. 3.9). The solid angle of a four-sided right rectangular pyramid with the side lengths a and b, and the distance h from the center of the rectangle to the origin can be calculated with the Oosterom and Strackee algorithm [66] and is given by

$$\Omega = 4 \arcsin \frac{ab}{\sqrt{(4h^2 + a^2)\,(4h^2 + b^2)}}. \tag{3.5}$$

By dividing the solid angle Ω by 4π one obtains the fractional area. The measured intensity is corrected by rescaling with the factor $4\pi/\Omega(\alpha)$.

The polarization of the synchrotron radiation was taken into account by Eq. (2.38) with $\phi = 0$, $P_\mathrm{i} = 0.05$, and $P_\mathrm{o} = 0.95$, leading to $P = 0.05 + 0.95\cos^2\theta$. The contribution of multiple scattering events to the measured intensity was insignificant, since the product of the sample length and linear attenuation coefficient of the liquid was always smaller than $\mu t \leq 0.17$ (see Sec. 2.3). The calculated energy shift due to the Compton effect (see Eq. (2.40)) in the experiments of this work was less than $1\,\mathrm{keV}$. Therefore, Compton scattered photons could not be separated. An absorption correction Eq. (2.37) was applied to the data with the linear attenuation coefficients taken from NIST [61]. Figure 3.10 shows the correction factors applied to the experimental data.

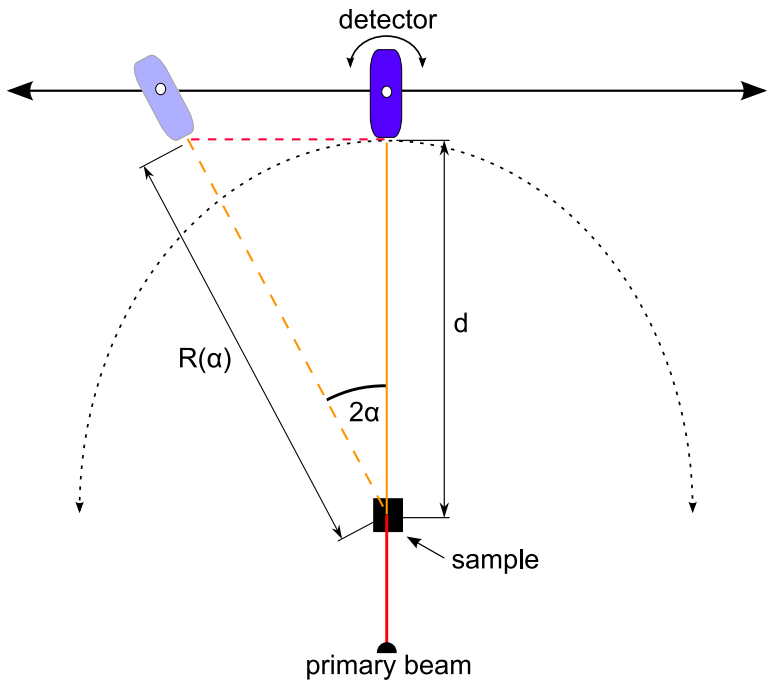

Figure 3.8: Sketch of the detector geometry for measuring the horizontal momentum transfer.

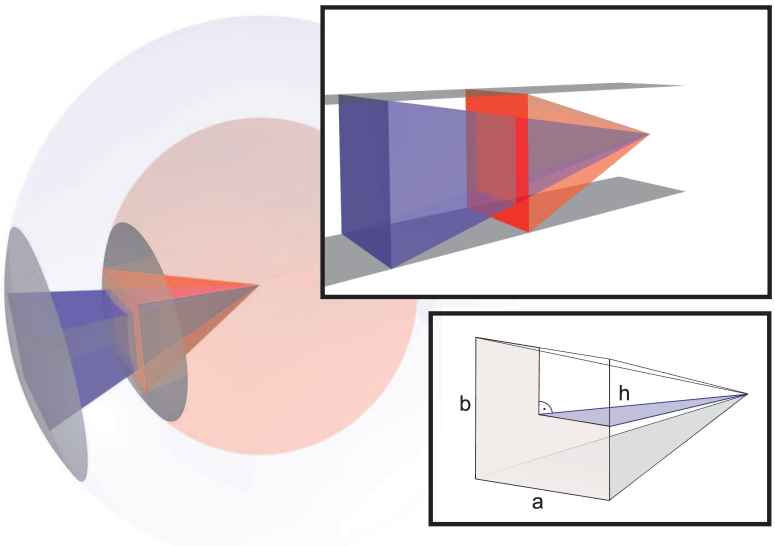

Figure 3.9: Sketches of solid angles spanned by rectangular areas or pyramides.

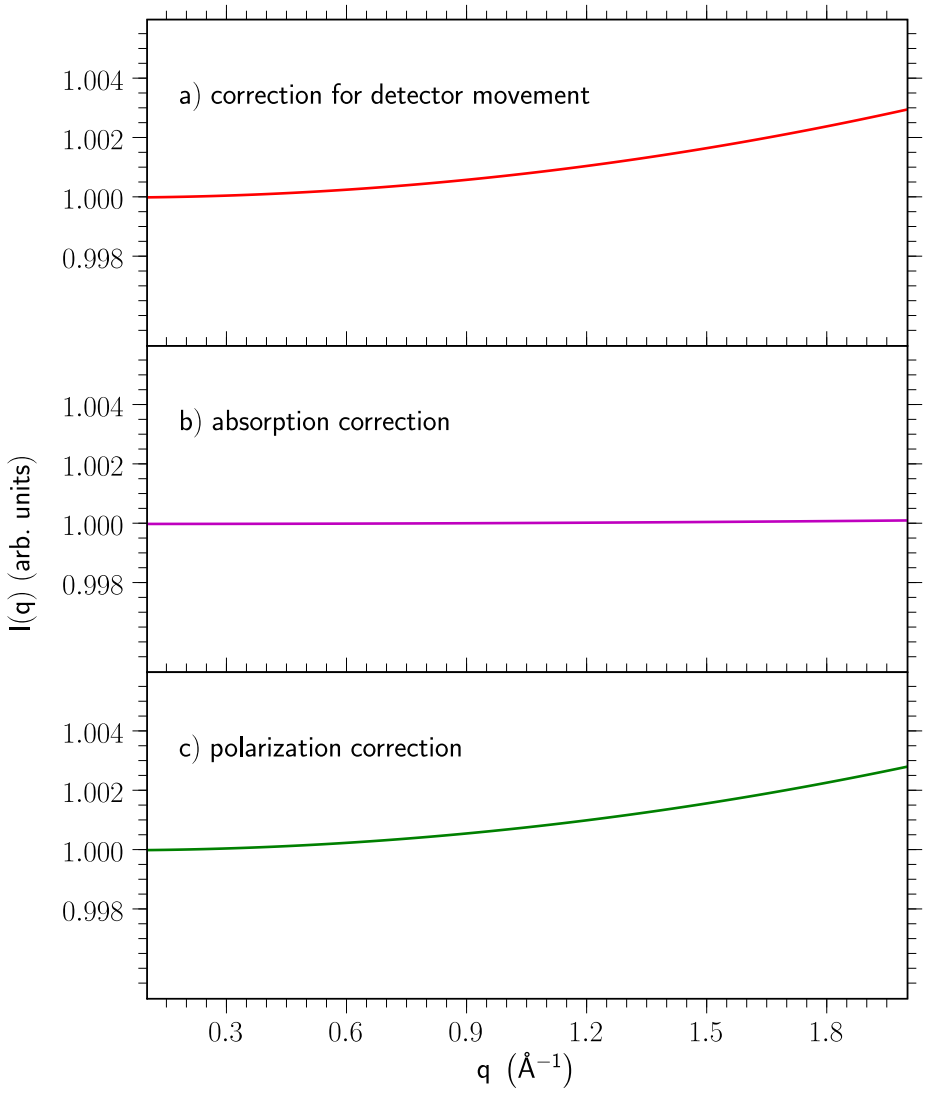

Figure 3.10: Corrections applied to the bulk liquid scattering intensity. a) The correction due to the detector movement, b) absorption correction (calculated with the linear absorption coefficient of [bmpy$^+$][Tf_2N^-] at 110 °C), and c) the polarization correction.

Chapter 4

Results and discussion

The results and the experimental data obtained in this work are presented in the following sections. First the density measurements of the bulk RTILs are discussed in detail and compared to literature values. Then the interfacial tension data of the RTILs are presented and analyzed, followed by the results and an elaborate discussion of the bulk liquid x-ray scattering from the four RTILs. Finally, the x-ray reflectivity data from RTIL-sapphire interfaces are presented together with the findings obtained by a thorough evaluation of that data.

4.1 Liquid density (pycnometry)

The bulk liquid density of all ionic liquids investigated in this work was measured as a function of temperature by density pycnometry. The knowledge of the density values of the RTILs is necessary in order to reduce the number of free parameters for the density profile reconstruction from the x-ray reflectivity and for the determination of the interfacial tension (see section 4.2).

A 5ml Duran glass pycnometer (see Fig. 4.1) was purchased from Carl Roth GmbH + Co. KG. The volume V_0 was calibrated at $T_0 = 20\,^{\circ}\mathrm{C}$ by the manufacturer. The temperature dependence of the volume was approximated by

$$V(T) = V_0 \left[1 + \gamma \left(T - T_0\right)\right]^3 \approx V_0 \left[1 + 3\alpha \left(T - T_0\right)\right], \tag{4.1}$$

with V_0 the calibrated volume at $T_0 = 20\,^{\circ}\mathrm{C}$, T the temperature in degrees Celsius and $\alpha = 3.3 \cdot 10^{-6}\,K^{-1}$ the linear expansion coefficient of borosilicate glass [67] and $\gamma \approx 3\alpha$. This is valid for isotropic materials and $\alpha T \ll 1$.

The pycnometer was cleaned with an alkaline detergent and afterwards rinsed with pure water. The mass of the cleaned empty pycnometer was determined by a balance with an accuracy of $\pm 0.5 \cdot 10^{-3}\,\mathrm{g}$ and will be referred to as m_p. The RTILs were degassed at a temperature of $80\,^{\circ}\mathrm{C}$ and a pressure of $1\,\mathrm{mbar}$ for $24\,\mathrm{h}$ before they were filled into the clean pycnometer. The equilibration time at each temperature was $1\,\mathrm{h}$. The excess liquid was removed with cleansing tissues.

Knowing the mass of the empty pycnometer m_p, the mass of the pycnometer filled with liquid $m_\mathrm{t}(T)$ and the volume of the pycnometer as a function of temperature

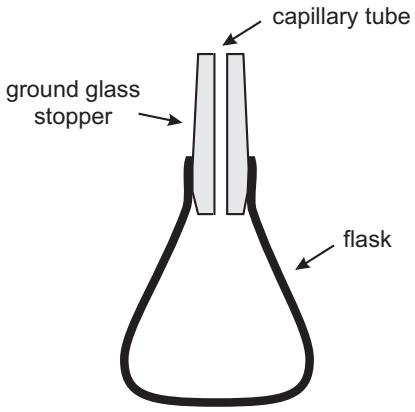

Figure 4.1: Sketch of a pycnometer as used for the determination of the RTIL bulk densities. The capillary tube feeding through the ground glass stopper provides a high precision for the measurement of changes in the volume, leading to a high accuracy of the density quantity.

$V(T)$, the temperature-dependent density of the liquid can be obtained via $\varrho(T) = (m_\mathrm{t}(T) - m_\mathrm{p})/V(T)$. The measured density values are shown in Tab. 4.1. The density values were fitted with a linear polynomial $\varrho(T) = a \cdot T + b$. The resulting fit parameters are summarized in Tab. 4.2. The density decreases with increasing temperature by approximately $10^{-3}\,\mathrm{g\,cm^{-3}K^{-1}}$.

With the knowledge of the temperature dependence of the densities, the volumetric thermal expansion coefficient $\gamma = -\frac{1}{\varrho}\frac{\partial \varrho}{\partial T}$ of the ionic liquids can be obtained with Eq. (4.1). Equation (4.1) can be rearranged to $\gamma(T) = \frac{1}{T}\left(\frac{\varrho_0}{\varrho(T)} - 1\right)$. The volumetric thermal expansion coefficients obtained from the density measurements for all investigated ionic liquids are shown in Tab. 4.2. They are all of the same order of magnitude $\gamma \approx 5 \cdot 10^{-4}\,\mathrm{K^{-1}}$ with only a slight increase with temperature. In the temperature range $-20\,^\circ\mathrm{C}$ to $+110\,^\circ\mathrm{C}$ γ changes less than $8\,\%$. The absolute error of the density measurements was estimated to $1.5 \cdot 10^{-3}\,\mathrm{g\,cm^{-3}}$ for all RTILs. The estimation was obtained by error propagation:

$$\begin{aligned}\Delta\varrho = &\left|\frac{1}{V(T)}\right|(\Delta m_\mathrm{t} + \Delta m_\mathrm{p}) + \left|\frac{m_\mathrm{p} - m_\mathrm{tl}}{V_0 V(T)}\right|\Delta V_0 \\ &+ \left|3\alpha V_0 \frac{m_\mathrm{p} - m_\mathrm{t}}{V(T)^2} + \frac{1}{V(T)}\frac{\partial m_\mathrm{t}}{\partial T}\right|\Delta T \\ &+ \left|3V_0\,(T_0 - T)\,\frac{m_\mathrm{p} - m_\mathrm{t}}{V(T)^2}\right|\Delta\alpha\end{aligned} \tag{4.2}$$

with $\Delta T = 0.5\,^\circ\mathrm{C}$ the temperature accuracy of the oven, $\Delta\alpha = 0.3 \cdot 10^{-7}\,\mathrm{K^{-1}}$ the error of the thermal expansion coefficient, $\Delta m_p = \Delta m_t = 0.5 \cdot 10^{-3}\,\mathrm{g}$ the uncertainty of the measurement of the mass of the empty and the filled pycnometer, respectively, and $\Delta V = 0.002\,\mathrm{cm^3}$ the error in the determination of the volume. The error of the volume is mainly caused by the high viscosities of the RTILs. The high viscosity leads

Table 4.1: Measured bulk density values ϱ of the ionic liquids at several temperatures.

	$[bmim^+][PF_6^-]$	$[bmim^+][BF_4^-]$	$[hmim^+][Tf_2N^-]$	$[bmpy^+][Tf_2N^-]$
T/(°C)	$\varrho/(\mathrm{g\,cm^{-3}})$	$\varrho/(\mathrm{g\,cm^{-3}})$	$\varrho/(\mathrm{g\,cm^{-3}})$	$\varrho/(\mathrm{g\,cm^{-3}})$
4.0	1.3873	1.2176	—	—
30.0	1.3640	1.1989	1.3693	—
35.0	—	—	—	1.3912
50.0	1.3512	1.1883	1.3536	1.3800
70.0	1.3381	1.1759	1.3357	1.3653
85.0	1.3261	1.1680	1.3235	
90.0	—	—	—	1.3491
100.0	1.3160	1.1572	1.3125	—
106.0	—	—	—	1.3416

to small air bubbles trapped inside the pycnometer and a small change in the position of the glass stopper. The error induced due to buoyancy falls within the above mentioned absolute error and was therefore not considered further. Impurities such as water and Cl^- decrease the density of RTILs as pointed out by Seddon et al. [68] and by the density data obtained by Jacquemin et al. [69]. All RTILs densities are higher than the density of water and vary between $1.2\,\mathrm{g\,cm^{-3}}$ and $1.4\,\mathrm{g\,cm^{-3}}$ at $20\,^\circ\mathrm{C}$. The density values of all measured RTILs are equal to the highest literature values or even higher. This suggests that the water content of our samples was rather small, but this was not quantified. Furthermore, the density values seem to deviate systematically from the literature; the difference increases with temperature with our data always lying above the literature values. This could be caused by an overestimation of the volume increase of the pynometer with temperature.

The density of $[bmim^+][BF_4^-]$ as a function of the temperature is shown in Fig. 4.2. The Figure also shows density values from literature. Our data compares well with the values measured by Azevedo et al. [70], Harris et al. [71] and Anthony et al. [72]. Also the value from the datasheet of the Merck KGaA [11] fits well. The highest deviation of about $1.4\,\%$ is found for the values obtained by Huo et al. [73]. The water content of the samples from Huo et al. was $< 2000\,\mathrm{ppm}$. Azevedo et al. reported a water content of $75\,\mathrm{ppm}$ and the samples of Harris et al. contained $70\,\mathrm{ppm}$ water. The water content of the samples from Anthony et al. was not reported. The two orders of magnitude higher water content of the samples from Huo et al. compared to Azevedo et al. and Harris et al. can explain the lower density values measured by Huo et al. The fact that our density values are very close to the ones from Harris et al. and Azevedo et al. suggests that our samples had also a water content of less than $100\,\mathrm{ppm}$.

The density of $[bmim^+][PF_6^-]$ is shown in Fig. 4.3 together with some values from literature. Jacquemin et al. [69] measured the density for a dry sample (about $190\,\mathrm{ppm}$

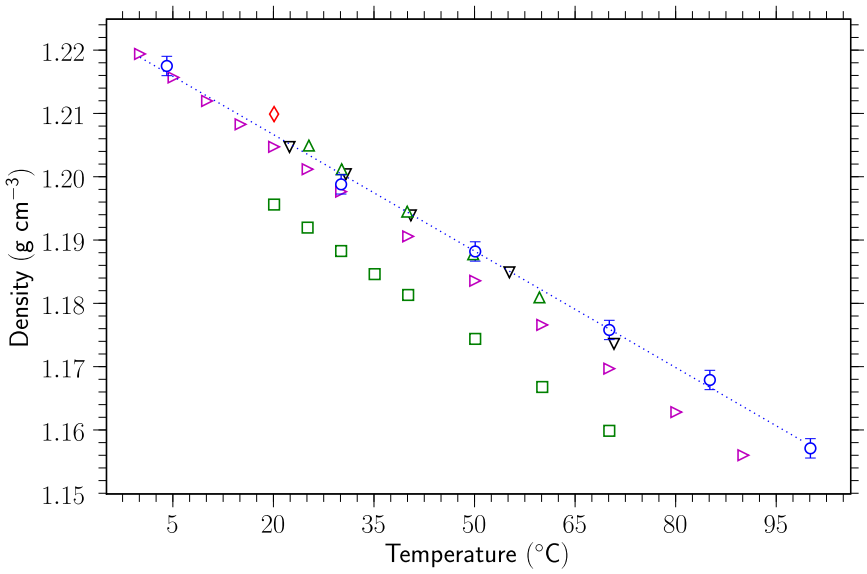

Figure 4.2: Temperature dependence of the density of [bmim$^+$][BF$_4^-$] (blue circles with error bars) and a linear fit to the data (blue dashed line) compared to literature values: Merck KGaA [11] data sheet value (red rhomb), Azevedo et al. [70] (green triangles up), Harris et al. [71] (magenta triangles right), Anthony et al. [72] (black triangles down), and Huo et al. [73] (green cubes).

water content) and a sample saturated with water (about $26800\,\mathrm{ppm}$ water content). The values of the saturated sample were about $1.5\,\%$ lower than the values of the dry sample. Other density values were measured by Pereiro et al. [74] (water content $300\,\mathrm{ppm}$), Kabo et al. [75] (water content $400\,\mathrm{ppm}$), Gu et al. [76] (water content $1500\,\mathrm{ppm}$) and Huo et al. [73] (water content $< 2000\,\mathrm{ppm}$). These values confirm the systematic decrease of the density with increasing water content.

The density of [hmim$^+$][Tf$_2$N$^-$] compares well with the available literature values (see Fig. 4.4). Azevedo et al. [77] reported a water content of $75\,\mathrm{ppm}$ of their samples and Kumelan et al. [78] used samples with a water content of $20\,\mathrm{ppm}$. Tokuda et al. [39] did not report any quantities concerning the mass fraction of water.

The density of [bmpy$^+$][Tf$_2$N$^-$] is shown in Fig. 4.5 together with some literature values. Gardas et al. [79] reported a water content of $22\,\mathrm{ppm}$. Tokuda et al. [39] did not report any values for the water content.

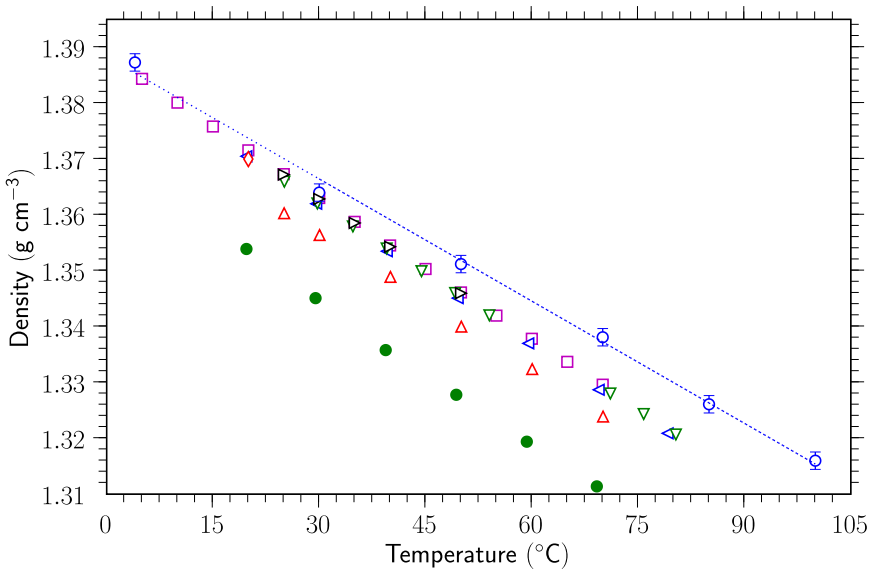

Figure 4.3: Temperature dependence of the [bmim$^+$][PF_6^-] density (blue circles with error bars) and a linear fit to the data (blue dashed line) compared to literature values: Merck KGaA [11] data sheet value (red rhomb), Kabo et al. [75] (green triangles down), Gu et al. [76] (red triangles up), Huo et al. [73] (black triangles right), Pereiro et al. [74] (magenta cubes), and Jacquemin et al. [69] (dried samples: blue triangles left; saturated with water: green full circles).

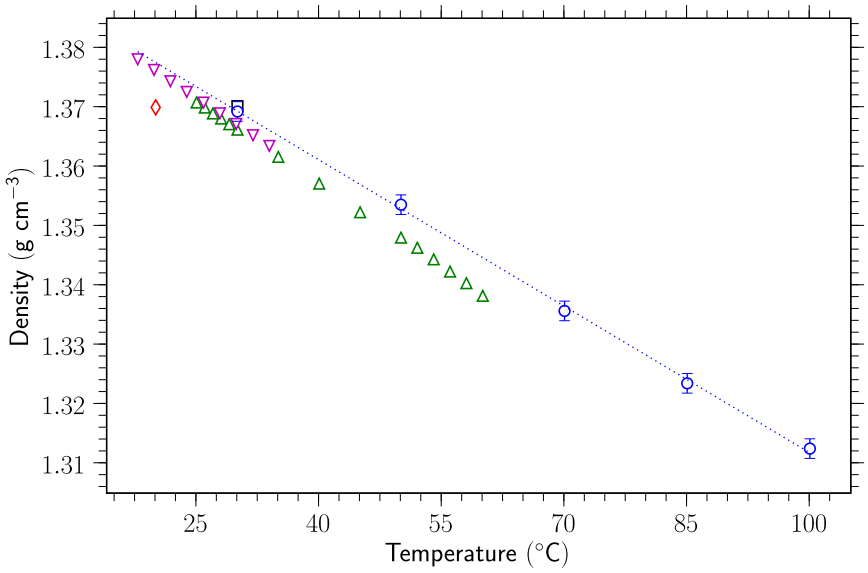

Figure 4.4: Temperature dependence of the [hmim$^+$][Tf_2N^-] density (blue circles with error bars) and a linear fit to the data (blue dashed line) compared to literature values: Merck KGaA [11] data sheet value (red rhomb), Azevedo et al. [77] (green triangles up), Kumelan et al. [78] (magenta triangles down), and Tokuda et al. [39] (black cube).

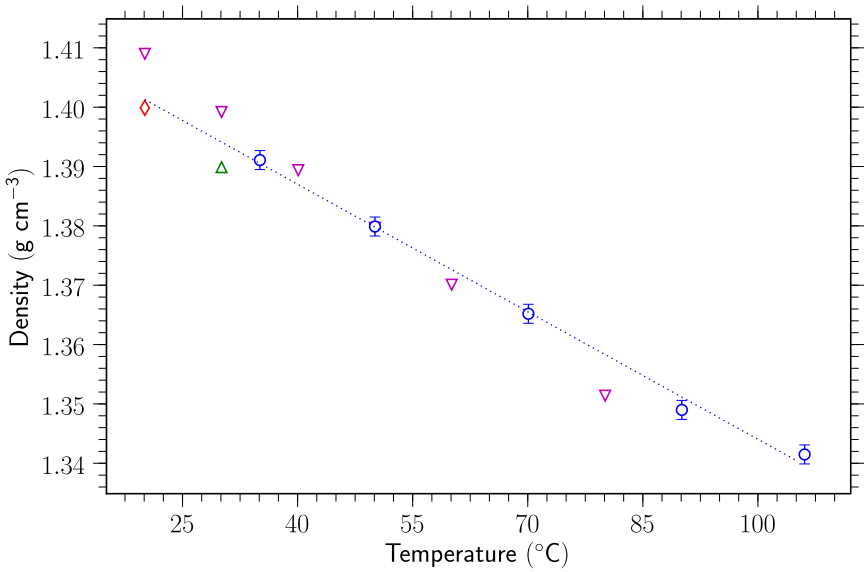

Figure 4.5: Temperature dependence of the [bmpy$^+$][Tf$_2$N$^-$] density (blue circles with error bars) and a linear fit to the data (blue dashed line) compared to literature values: Merck KGaA [11] data sheet value (red rhomb), Gardas et al. [79] (magenta triangles down), and Tokuda et al. [39] (green triangle up).

Table 4.2: Thermal expansion coefficients $\gamma/(10^{-4}\ \mathrm{K}^{-1})$ of the RTILs and correlation parameters $a/(\mathrm{g\ cm}^{-3}\mathrm{K}^{-1})$ and $b/(\mathrm{g\ cm}^{-3})$ for the densities as a function of temperature determined by fitting the measured values with a linear function $\varrho(T) = a \cdot T + b$.

	[bmim$^+$][PF$_6^-$]	[bmim$^+$][BF$_4^-$]	[hmim$^+$][Tf$_2$N$^-$]	[bmpy$^+$][Tf$_2$N$^-$]
γ	5.3	5.1	6.0	5.1
a	-0.0007	-0.0006	-0.0008	-0.0007
b	1.3883	1.2189	1.3940	1.4157

4.2 Surface and interfacial tension

RTILs can be considered as binary solutions. The impact of the cation/anion combination on the interfacial tension and particular composition at the interface are discussed in the following section. The interfacial tension between a RTIL and air is also referred to as surface tension.

The interfacial tensions γ_{ab} can be separated into contributions arising from dispersion and polar forces with an approach introduced by Fowkes [80], assuming that the total interfacial energy of n-hexane arises from dispersion forces only. Fowkes experimentally confirmed his prediction that the geometric mean of the dispersion forces sufficiently describes the interaction energies at the interface caused by dispersion forces

$$\gamma_{ab} = \gamma_a + \gamma_b - 2\sqrt{\gamma_a^d \gamma_b^d}, \tag{4.3}$$

$$\gamma_a = \gamma_a^d + \gamma_a^p, \tag{4.4}$$

with γ_a as the surface tension of liquid a, γ_a^d the dispersion force component of liquid a and γ_a^p the polar force component of liquid a. Equation (4.4) was suggested by Schultz et al. [81], assuming that the surface tension can generally be expressed by the sum of a dispersion and a polar component.

The interfacial tensions of four RTILs with air and n-hexane were measured at ambient conditions ($22 \pm 2\,^\circ\mathrm{C}$, $22 \pm 1\,\%\,\mathrm{RH}$) with the pendant drop method. The latter exploits the fact that the gravitational force acting on a drop of a few μl (depending on the interfacial density difference) is of the same order of magnitude as the corresponding interfacial tension. Therefore, the interfacial tension can be obtained by fitting numerical solutions of the Laplace equation to a digitized contour of a hanging drop right before it detaches from the dispense needle. Measurements and drop shape analysis were performed on the instrument OCA 30 (Dataphysics, see Fig. 4.6). The instrument was adjusted to reach a high optical contrast even for the liquid-liquid measurements and still provide a vapor-water tension value of $72.8\,\mathrm{mN\,m^{-1}}$ at $22\,^\circ\mathrm{C}$ in good agreement with the literature ($72.4\,\mathrm{mN\,m^{-1}}$ at $22\,^\circ\mathrm{C}$ obtained by a second order polynomial fit to the data from CRC handbook [82]).

Every measurement was repeated five times. The arithmetic means for all RTILs are summarized in Tab. 4.3. The standard deviation of the respective measurements was $\pm 0.1\,\mathrm{mN\,m^{-1}}$. However, additional error sources led to a higher total error of about $\pm 0.6\,\mathrm{mN\,m^{-1}}$. The main error sources are the background lighting which may lead to a deviation from the calibration and the adjustment of the focus which may cause an altered drop shape and therefore result in a different interfacial tension value.

Figure 4.6: The instrument OCA 30 used for the pendant drop measurements (left). A picture of a pendant drop of pure water surrounded by air (center) and picture of a pendant drop of [hmim$^+$][Tf_2N^-] immersed in n-hexane (right) as recorded with the OCA 30.

Table 4.3: Surface tension $\gamma_v/(\mathrm{mN\,m^{-1}})$, interfacial tension with n-hexane $\gamma_{C6}/(\mathrm{mN\,m^{-1}})$, dispersive component $\gamma^d/(\mathrm{mN\,m^{-1}})$, and polar component $\gamma^p/(\mathrm{mN\,m^{-1}})$ of the four RTILs measured with the pendant drop method.

	γ_v	γ_{C6}	γ^d	γ^p
[bmim$^+$][PF_6^-]	43.5	14.1	30.8	12.7
[bmim$^+$][BF_4^-]	44.2	13.1	33.0	11.2
[hmim$^+$][Tf_2N^-]	31.0	4.9	26.8	4.2
[bmpy$^+$][Tf_2N^-]	33.2	8.2	25.5	7.7

The obtained surface tensions of the RTILs are in general higher than for alkanes (e.g. n-Decane: $\gamma_v = 23.9\,\mathrm{mN\,m^{-1}}$ [80]) but still smaller than the surface tension of water. The surface tensions of [bmim$^+$][PF_6^-] and [bmim$^+$][BF_4^-] are of the same order of magnitude and so are their interfacial tensions with n-hexane. However, the latter has a slightly higher surface tension and a slightly lower interfacial tension. Consequently, this leads to similar dispersion and similar polar components for both RTILs. Mach et al. [83] reported that fluorination tends to lower the surface tension substantially. Therefore the decrease of surface tension by changing the anion from [BF_4^-] to [PF_6^-] is most likely caused by the higher degree of fluorination for the latter anion rather than by the variation of the anion size. Exchanging the anion by a similar type of anions has only a small impact on the surface tension.

Similar results were obtained for the surface tensions of [hmim$^+$][Tf_2N^-] and [bmpy$^+$] [Tf_2N^-] with a slightly higher value for the latter one. Exchanging the cations modified the surface tension by about the same amount as exchange of the anions in [bmim$^+$][PF_6^-] and [bmim$^+$][BF_4^-]. The interfacial tensions between n-hexane and [hmim$^+$][Tf_2N^-] and [bmpy$^+$][Tf_2N^-] deviate by about $40\,\%$ from each other. This can be explained by an increase of the dispersive component caused by the longer alkyl-chain for [hmim$^+$] compared to [bmpy$^+$].

Langmuir's principle of independent surface action [84] states that the value of the interfacial tension corresponds to the chemical composition of the interface. Since both, anion and cation, have an impact on the surface tension of the RTILs as discussed before, they should both be present at the surface.

Figure 4.7 shows the surface tension values for the RTILs measured in this work together with some literature values. The spread of the literature data is rather large. The values of Sung et al. [85] and Deetlefs et al. [86] agree well with our data for [bmim$^+$][BF$_4^-$]. Also Sloutskin et al. [15] measured the surface tension for both RTILs, [bmim$^+$][BF$_4^-$] and [bmim$^+$][PF$_6^-$], with less deviation for the value of the dry sample. Freire et al. [87] obtained temperature-dependent values for the same two RTILs which are in good agreement with our data. The difference between our data and the values measured by Huddleston et al. [38] is significant, for [bmim$^+$][BF$_4^-$] our value is smaller by about $2.5\,\mathrm{mN\,m^{-1}}$ and for [bmim$^+$][PF$_6^-$] by about $5.5\,\mathrm{mN\,m^{-1}}$. Pereiro et al. [88] and Halka et al. [89] measured values for the surface tension of [bmim$^+$][PF$_6^-$] which fit in with the data obtained in this work. Dzyuba et al. [90] report values for [bmim$^+$][PF$_6^-$] and [hmim$^+$][Tf$_2$N$^-$], which are about $2.5\,\mathrm{mN\,m^{-1}}$ and about $4.5\,\mathrm{mN\,m^{-1}}$ higher than our data, respectively. The surface tension of [hmim$^+$][Tf$_2$N$^-$] agrees well with the temperature-dependent values obtained by Rebelo et al. [91]. Millefiorini et al. [92] report values for [hmim$^+$][Tf$_2$N$^-$] and [bmpy$^+$][Tf$_2$N$^-$]. The value for the latter one deviates only little from our data compared to a lower value of about $4\,\mathrm{mN\,m^{-1}}$ for the first one.

The above mentioned literature values were obtained by different methods. Huddleston et al. [38] and Freire et al. [87] used the du Noüy ring method [93]. Our values obtained with the pendant drop method coincide well with the values from Freire et al., but not with the values supplied by Huddleston et al. This suggests that the value of the surface tension does not unconditionally dependent on the method used. The scatter of the data for the surface tensions could also be caused by the different water and halide contents of the samples. Freire et al. [87] confirmed the dependence of the [bmim$^+$][PF$_6^-$] surface tension on the bulk water content. Starting from a dry sample the surface tension first decreases with increasing water content to about $94\,\%$ of the value of the dry sample and then increases again to a somewhat higher value than the starting value for the dry sample. Therefore, a deviation up to $6\,\%$ can be explained already by means of the bulk water content. Additionally, Deetlefs et al. [86] suggested that an increase of halide content may lead to an increase of the surface tension. Up to now there is, however, no data confirmation of this suggestion.

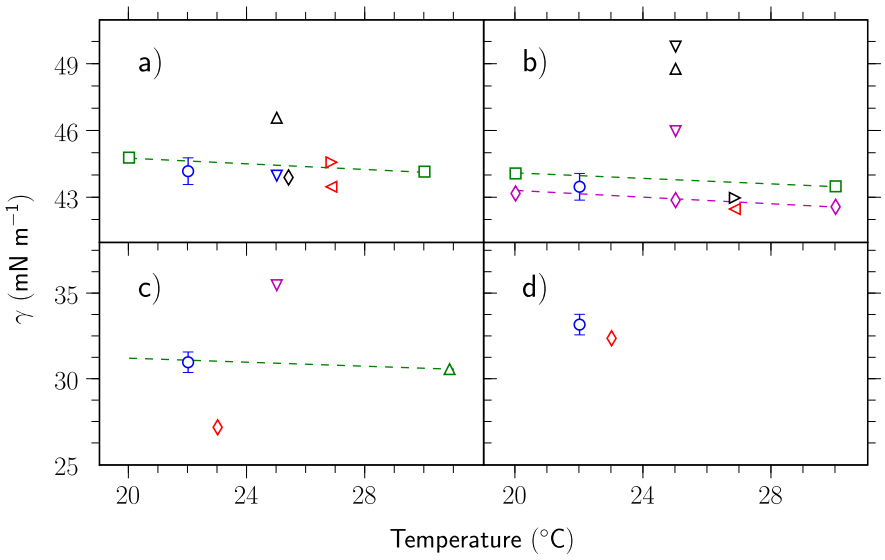

Figure 4.7: Measured surface tension values (blue open circles with error bars) together with literature values. a) [bmim$^+$][BF$_4^-$]: Huddleston et al. [38] (black triangle up), Sung et al. [85] (blue triangle down), Deetlefs et al. [86] (black rhomb), Freire et al. [87] (green cubes, green dashed line: linear fit to temperature dependent data), Sloutskin et al. [15] (red triangle left: dry sample, red triangle right: with water saturated sample); b) [bmim$^+$][PF$_6^-$]: Pereiro et al. [88] (magenta rhombs; magenta dashed line: second order polynomial fit to temperature dependent data), Freire et al. [87] (green cubes, green dashed line: linear fit to temperature dependent data), Sloutskin et al. [15] (red triangle left), Halka et al. [89] (black triangle right), Dzyuba et al. [90] (magenta triangle down), Huddleston et al. [38] (black triangle up: dry sample, black triangle down: with water saturated sample); c) [hmim$^+$][Tf$_2$N$^-$]: Dzyuba et al. [90] (magenta triangle down), Millefiorini et al. [92] (red rhomb), Rebelo et al. [91] (green triangle up; green dashed line: linear fit to the temperature dependent data); d) [bmpy$^+$][Tf$_2$N$^-$]: Millefiorini et al. [92] (red rhomb).

4.3 Bulk liquid structure

The bulk liquid x-ray scattering experiments were performed with the same setup used for the x-ray reflectivity experiments at the beamline ID15A, ESRF. The horizontal momentum transfer was varied up to $q = 2\,\text{Å}^{-1}$ for the measurement of the bulk liquid scattering. The raw data was corrected as described in Sec. 3.5.

The corrected data are summarized in Fig. 4.8. The RTILs containing the [Tf$_2$N$^-$] anion ([hmim$^+$][Tf$_2$N$^-$] and [bmpy$^+$][Tf$_2$N$^-$]) were both measured at $T = 110\,^\circ\text{C}$ and $T = -20\,^\circ\text{C}$. The bulk scattering of the RTILs containing the [bmim$^+$] cation ([bmim$^+$][BF$_4^-$] and [bmim$^+$][PF$_6^-$]) were measured at $T = 110\,^\circ\text{C}$ for the first and at $T = -20\,^\circ\text{C}$ for the latter. The RTIL [bmpy$^+$] [Tf$_2$N$^-$] was also measured with a high water content at $T = 2\,^\circ\text{C}$. The RTIL droplet was saturated with water by im-

mersing it in pure water for $12\,\mathrm{h}$ at room temperature (maximum possible water uptake: $14800\,\mathrm{ppm}$ [12]).

Bulk liquid scattering from [bmim$^+$][BF$_4^-$] and [bmim$^+$][PF$_6^-$]

The bulk liquid scattering recorded for [bmim$^+$][BF$_4^-$] shows only one maximum at $q = 1.47\,\text{Å}^{-1}$ in the investigated momentum transfer range. The scattered intensity of [bmim$^+$][PF$_6^-$] shows two clear maxima, one at $q = 0.99\,\text{Å}^{-1}$ and one at $q = 1.43\,\text{Å}^{-1}$. These peaks indicate dominant length scales on which spatial correlations are present in the bulk liquid (see Sec. 2.3). The corresponding real space distances are approximately given by $2\pi/q = 4.3\,\text{Å}$ for the peak in the intensity scattered of [bmim$^+$][BF$_4^-$], and $6.4\,\text{Å}$ and $4.4\,\text{Å}$ for the first and second peak in the [bmim$^+$][PF$_6^-$] data, respectively. Furthermore, a shoulder rather than a distinct peak is observed in the low q range, which is less pronounced in the bulk liquid scattering from [bmim$^+$][BF$_4^-$]. The shoulder in the scattered intensity of [bmim$^+$][PF$_6^-$] spans roughly the range $0.45\,\text{Å}^{-1} < q < 0.7\,\text{Å}^{-1}$. The first peak in [bmim$^+$][PF$_6^-$] cannot be assigned to intramolecular correlations within the cation, since no such peak was observed for the [bmim$^+$][BF$_4^-$] containing the same cation. The peak at $q = 1.43\,\text{Å}^{-1}$ can be assigned to the distance between imidazolium rings in planar configuration [94].

The x-ray analysis of shock-induced crystallization of supercooled [bmim$^+$][PF$_6^-$] showed a rather unconventional charge ordered structure with the cations forming channels, where the anions are placed in the channels [95]. In these measurements, a similar imidazolium-imidazolium interplanar distance of $4.34\,\text{Å}$ was retrieved. Furthermore, a centroid-to-centroid separation of $6.11\,\text{Å}$ was reported for the cations in this configuration. Interestingly, the x-ray analysis of the crystallized [bmim$^+$][PF$_6^-$] revealed that two different imidazolium-imidazolium ring arrangements are present in the crystal structure. Figure 4.9a shows a sketch of both structures. The first structure with the butyl groups pointing into the space between the imidazolium rings (cations shown in red in Fig. 4.9a) exhibits correlations as mentioned before. The second structure with the butyl groups pointing away (cations shown in green in Fig. 4.9a) shows an interplanar imidazolium-imidazolium distance of $3.46\,\text{Å}$ and a centroid-to-centroid distance of $4.86\,\text{Å}$. The centers of corresponding imidazolium ring pairs are shifted by $4.31\,\text{Å}$. This suggests that the second peak observed in the bulk liquid scattering from [bmim$^+$][PF$_6^-$] corresponds to planar correlations between imidazolium rings with the butyl chains pointing into the space between them. The first peak corresponds to centroid-centroid correlations of the cations. The second possible arrangement may be less pronounced in the liquid state due to the higher mobility of the molecules.

Keeping the structure analysis results of [bmim$^+$][PF$_6^-$] in mind and comparing it to [bmim$^+$][BF$_4^-$] suggests that the interplanar distance of the imidazolium rings is even smaller than in the crystallized state of [bmim$^+$][PF$_6^-$], reflected in the real space correlation distance of $4.3\,\text{Å}$. Since no peak indicates the presence of centroid-centroid correlations of $6.1\,\text{Å}$ in the RTIL [bmim$^+$][BF$_4^-$], some structural changes of the cations have to occur by changing the anion from [PF$_6^-$] to [BF$_4^-$]. The smaller anion [BF$_4^-$] has, however, also a smaller ionic radius and exhibits therefore a stronger cation-anion bond-

ing. This enables tighter ion packing and could therefore lead to a smaller imidazolium-imidazolium ring distance and more importantly to a smaller shift of the ring centers of respective cation pairs which would result in a smaller centroid-centroid correlation distance of about the same as the interplanar imidazolium ring distances. This explains also the broader peak with the center positioned at $q = 1.47\,\text{Å}^{-1}$ in the bulk liquid scattering intensity of [bmim$^+$][BF$_4^-$]. This finding is corroborated by neutron diffraction data obtained from liquid 1,3-dimethylimidazolium hexafluorophosphate [mmim$^+$][PF$_6^-$] and 1,3-dimethylimidazolium chloride [mmim$^+$][Cl$^-$], which show that the most favorable location of the chloride is closer to the imidazolium ring of the cation than the hexafluorophosphate reflected in a expanded liquid structure for the RTIL with the latter anion [96, 97]. It was already reported that the structure of different solid RTILs is at least partially preserved even in their liquid state, although the absolute distances are most likely to change upon melting [97, 98].

Further evidence for the peak assignments discussed above is provided by the results of x-ray structural analysis of the 1-ethyl-3-methylimidazolium hexafluorophosphate [emim$^+$][PF$_6^-$] by Fuller et al. [99]. They reported a centroid-centroid cation pair separation of $5.39\,\text{Å}$ and a imidazolium ring-ring distance of $4.53\,\text{Å}$. The structural arrangement is mainly driven by interionic cation-anion coulomb interactions and only minimal hydrogen bonding forces [99]. On the other hand, simulations assigned the correlation distance of approximately $4.3\,\text{Å}$ to the first solvation shell of the [PF$_6^-$] anion around the imidazolium ring. The characteristic distance of $6.35\,\text{Å}$ resembles cation-cation correlations in these studies [100]. This would also explain the [bmim$^+$][BF$_4^-$] data, since a smaller anion leads to smaller cation-cation distances which could in the case of [bmim$^+$][BF$_4^-$] coincide with the correlation length of the first solvation shell.

Finally, the low q shoulder has to be discussed. Wide angle x-ray diffraction data of [bmim$^+$][PF$_6^-$] also showed a low q shoulder between $0.6\,\text{Å}^{-1}$ and $0.7\,\text{Å}^{-1}$ [94]. The authors suggested that such a feature is related to intermediate range order. Molecular dynamic simulation studies showed indeed such a low wave-vector peak [100]. The presence of such a peak was attributed to medium range spatial correlations between long alkyl chains. Medium range correlations were also found in the partial structure factor of the anions. Since twice the centroid-centroid distance in [bmim$^+$][PF$_6^-$] corresponds to features in the low q range, it may be concluded that the shoulder originates from medium range correlations of the butyl chains of the cation. A less pronounced low q shoulder in the case of [bmim$^+$][BF$_4^-$] is most likely caused by closer packing of the ions, leading to a reduced order of the alkyl chains caused by steric hindrance.

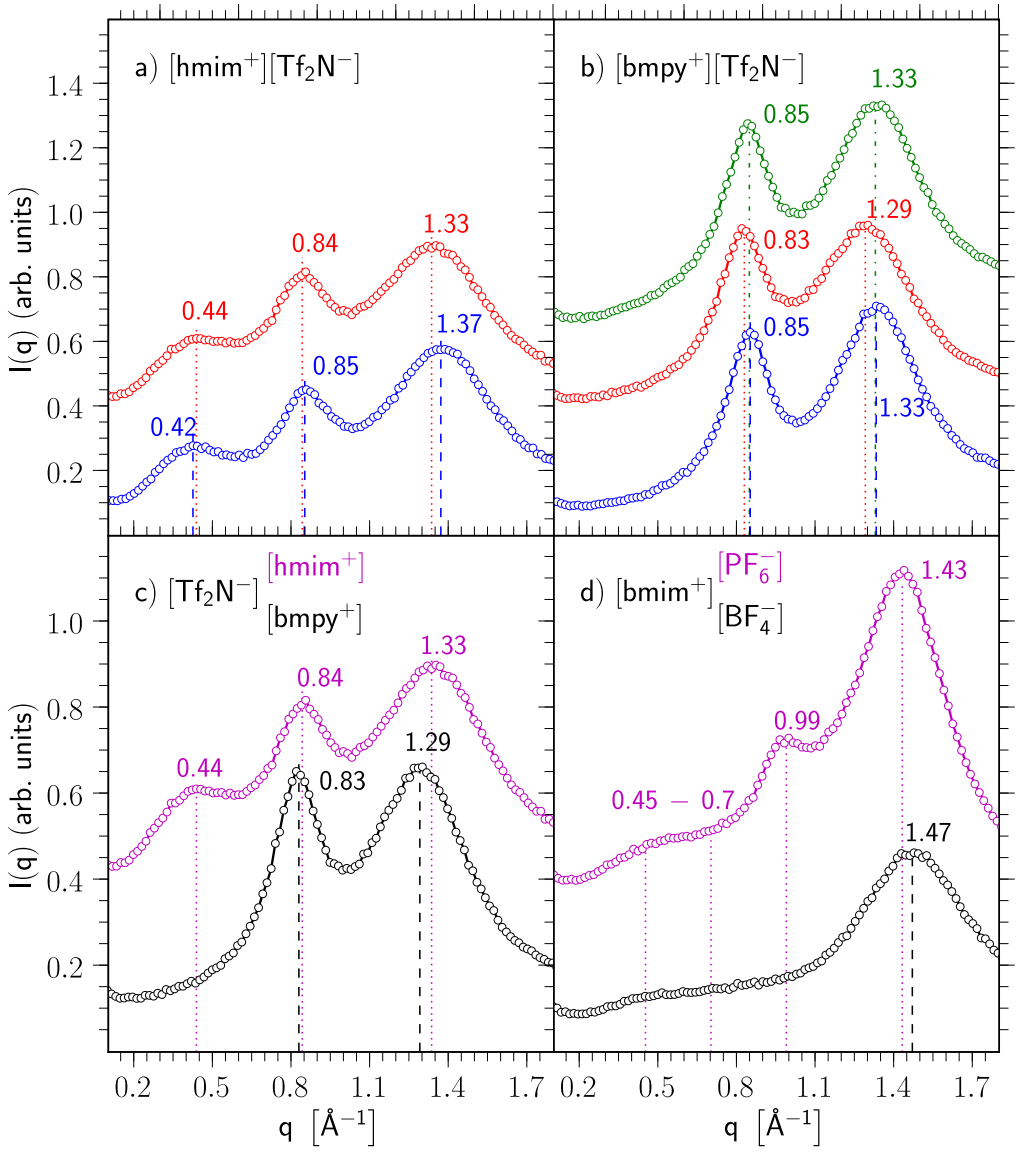

Figure 4.8: Bulk liquid scattering results from a) [hmim$^+$][Tf$_2$N$^-$]. All curves are shifted vertically by 0.3 units for clarity. b) [bmpy$^+$][Tf$_2$N$^-$] at $T = 110\,^\circ$C (red curves) and $T = -20\,^\circ$C (blue curves). The green curve shows the scattered intensity from a water saturated sample of [bmpy$^+$][Tf$_2$N$^-$] at $T = 2\,^\circ$C. c) Comparison of the high temperature measurements of [hmim$^+$][Tf$_2$N$^-$] (magenta curve) and [bmpy$^+$][Tf$_2$N$^-$] (black curve). d) Scattered intensity of [bmim$^+$][PF$_6^-$] at $T = 110\,^\circ$C (magenta curve) and of [bmim$^+$][BF$_4^-$] at $T = -20\,^\circ$C (black curve).

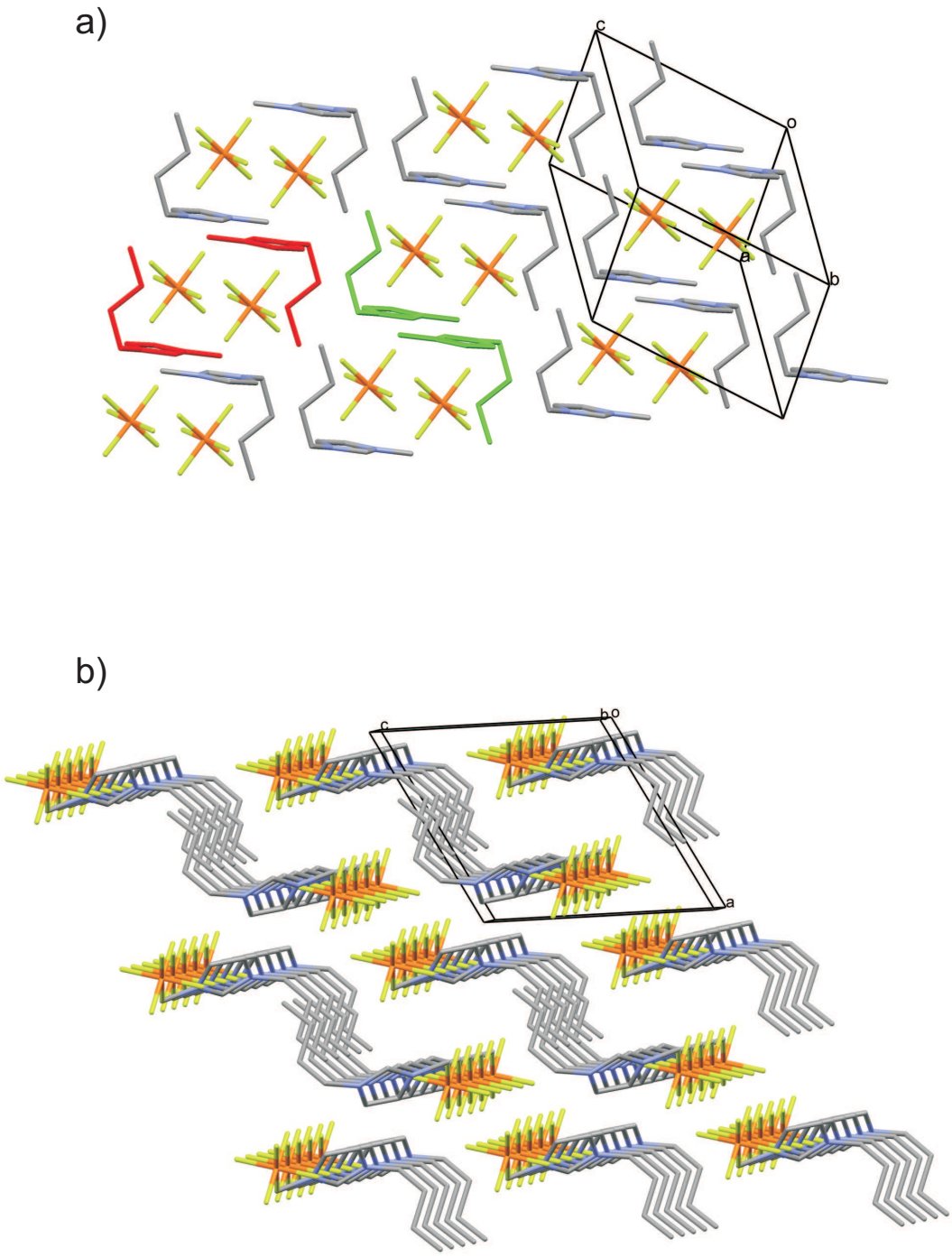

Figure 4.9: Sketches of structural arrangements of [bmim$^+$][PF_6^-] reproduced from Dibrov et al. [95] with the visualisation software *Mercury* [101]. a) Two different types of interplanar arrangements of imidazolium cations in [bmim$^+$][PF_6^-]. b) A view of the molecular arrangements of [bmim$^+$][PF_6^-], showing the [PF_6^-] channels with interpenetrating alkyl chains. H atoms have been omitted.

Bulk liquid scattering from [hmim$^+$][Tf_2N^-] and [bmpy$^+$][Tf_2N^-]

Clear maxima can be observed in the high temperature data of [hmim$^+$][Tf_2N^-] at $q = 0.44\,\text{Å}^{-1}$, $q = 0.84\,\text{Å}^{-1}$ and $q = 1.33\,\text{Å}^{-1}$. The first maximum shifts to a lower q value upon changing the temperature to $T = -20\,^\circ\text{C}$. The other maxima shift to higher q values with a decrease in temperature. The thermal expansion coefficient of [hmim$^+$][Tf_2N^-] (see Sec. 4.1) states a linear expansion in one dimension which is approximately twice as much as the shifts of the maxima in the bulk liquid scattering.

The bulk liquid scattering of [bmpy$^+$][Tf_2N^-] at $T = 110\,^\circ\text{C}$ exhibits two maxima at $q = 0.83\,\text{Å}^{-1}$ and $q = 1.29\,\text{Å}^{-1}$. The maxima shift to higher q values as the temperature is decreased to $T = -20\,^\circ\text{C}$. The scattered intensity from [bmpy$^+$][Tf_2N^-] saturated with water at $T = 2\,^\circ\text{C}$ shows exactly the same features as the dry [bmpy$^+$][Tf_2N^-] at $T = -20\,^\circ\text{C}$.

The first peak in the bulk liquid scattering of [hmim$^+$][Tf_2N^-] appears at the position of the low q shoulder in [bmim$^+$][PF_6^-], but much more pronounced, since the cations contain the longer hexyl chain. The temperature behavior of this peak suggests even further that it corresponds to medium range correlations of the cation alkyl chains. The first peak gets sharper and shifts to a lower q value with decreasing temperature whereas the other features shift to higher q values. Thus, the spatial correlations are enhanced and the corresponding real space distance increases with decreasing temperature. A possible explanation is that the lower temperature leads to a reduced mobility of the alkyl chains around their C-C bonds with a linear conformation of the hydrocarbon chains. The real space distance assigned to the peak at $q = 0.42\,\text{Å}^{-1}$ in the case of the $T = -20\,^\circ\text{C}$ measurement is $15.0\,\text{Å}$. Again this is roughly twice the correlation distance of the second maximum $7.4\,\text{Å}$ which appeared in the [hmim$^+$][Tf_2N^-] scattering data. The absence of such a low q peak or shoulder in the data of [bmpy$^+$][Tf_2N^-] suggests that the anion contribution to it is rather weak or even missing.

The second and third peak in the [hmim$^+$][Tf_2N^-] data are assigned to the cation centroid-centroid distance and the interplanar imidazolium ring distance, respectively, in the same manner as in the [bmim$^+$][PF_6^-] case. Both peak positions are at lower q values than for [bmim$^+$][PF_6^-], resembling the larger anion with a higher degree of charge delocalization.

In the case of [bmpy$^+$][Tf_2N^-] no peak or shoulder is observed in the low q range. The first and second peak correspond to real space distances of $7.6\,\text{Å}$ and $4.9\,\text{Å}$, respectively. These distances are slightly larger compared to the corresponding distances in the [hmim$^+$][Tf_2N^-] data. This could be caused by the twisted pyrrolidinium ring of the cation which prevents packing as close as in the case of [hmim$^+$][Tf_2N^-].

The [bmpy$^+$][Tf_2N^-] saturated with water at $T = 2\,^\circ\text{C}$ shows the same features at the same positions in the scattered intensity as the data of dry [bmpy$^+$][Tf_2N^-] at $T = -20\,^\circ\text{C}$. This implies that the small water content does not change the ion correlations discussed before. The water molecules tend to bond preferably to the anions via hydrogen bonding [102].

In order to favor one of the above discussed explanations upon others, further bulk liquid scattering data is needed from RTILs with systematically changed cations, alkyl

chain lengths and/or anions.

Table 4.4: Peak positions $q\,(\text{Å}^{-1})$ and corresponding real space distances $d\,(\text{Å})$ obtained by bulk liquid x-ray scattering at different temperatures.

$T\,(^\circ\text{C})$	[bmim$^+$][BF$_4^-$]		[bmim$^+$][PF$_6^-$]		[hmim$^+$][Tf$_2$N$^-$]		[bmpy$^+$][Tf$_2$N$^-$]	
	q	d	q	d	q	d	q	d
	1.47	4.3[b]	–	–	1.33	4.7[b]	1.29	4.9[b]
110			–	–	0.84	7.5[a]	0.83	7.6[a]
			–	–	0.44	14.3[c]		
	–	–	1.43	4.4[b]	1.37	4.6[b]	1.33	4.7[b]
-20	–	–	0.99	6.4[a]	0.85	7.4[a]	0.85	7.4[a]
	–	–	< 0.7	> 9.0[c]	0.42	15.0[c]		

a: corresponds to the cation centroid-centroid correlation distance or cation-cation distance

b: corresponds to the imidazolium ring-ring distance or the first solvation shell of the anion

c: corresponds to alkyl chain medium range correlations

4.4 X-ray reflectivity

The reflectivity data presented in the following section were obtained during five beamtimes (May 2007, June 2007, September 2007, November 2007 and February 2008) at beamline ID15A of the ESRF, which were partially devoted to this project. The interfaces of sapphire with four different RTILs were probed with x-ray reflectivity at two different temperatures each. In addition, the interface between sapphire and one RTIL ([bmpy$^+$][Tf$_2$N$^-$]) with high water content was investigated. A summary of the experimental reflectivity curves is shown in Fig. 4.10. All measurements span a momentum transfer range up to at least $q_z = 1.3\,\text{Å}^{-1}$, resulting in a molecular-scale real space resolution of $4.8\,\text{Å}$.

Three of the four investigated solid-liquid interfaces show clear features in their reflectivity data, suggesting molecular layered structures in the vertical direction. In principle there are two different ways to form a layered structure in a two-component ionic system, both are depicted in Fig. 4.11 and Fig. 4.12. The first possibility is a checkerboard-type structure with an equal amount of anions and cations in each layer (Fig. 4.11). This structure should be formed in systems where the coulomb interactions between the ions are the dominant interactions. The other feasible arrangement is a double layer structure with anions and cations clearly separated into distinct layers Fig. 4.12. This structure requires a system with strong correlations between the ions and a preference for either cations or anions at the interface. These two models can clearly be distinguished by their associated layering periodicity d_l.

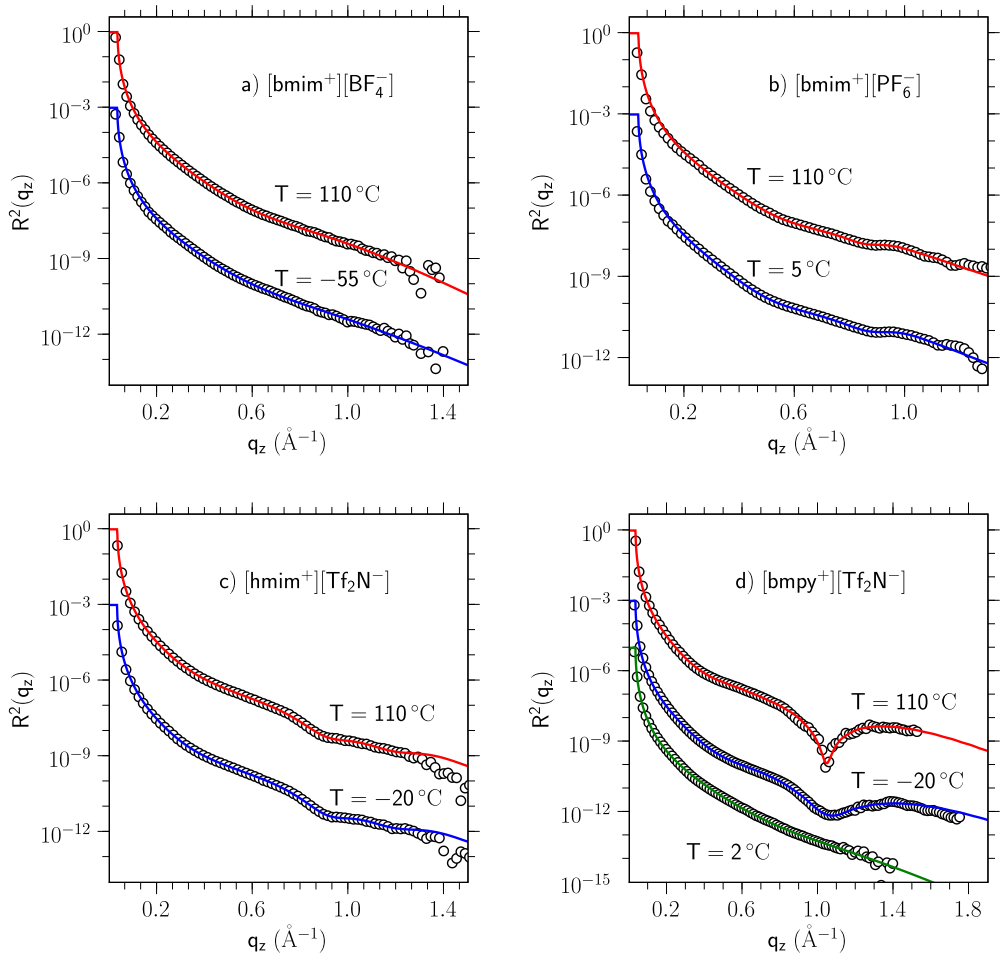

Figure 4.10: Summary of the reflectivity measurements (black circles) together with the fits obtained via the DC model (solid lines). Every solid-liquid interface was investigated at a high (red line) and a low (blue line) temperature. The corresponding data to the green line in d) shows the reflectivity of a [bmpy$^+$][Tf$_2$N$^-$] - sapphire interface saturated with water. The curves are shifted vertically for clarity.

Due to the loss of phase information in x-ray reflectivity experiments (see Sec. 2.2), the electron density profiles perpendicular to the interfaces have been reconstructed by parameter refinement of model profiles. The models employed in the analysis are the modified two component distorted crystal model (DC) (see Sec. 2.2.2) and a semi-quantitative generic layering model (SQ) (see Sec. 2.2.1). Initially, the DC model simulates the before discussed ion double-layer structure. However, also the checkerboard-type structure can be simulated with the DC model by using the symmetry factor Δ_s.

Fixing that symmetry factor to $\Delta_s = -0.5\, d_l$ results in a coinciding position of the j^{th} cation layer center with the j^{th} anion layer center, thus resembling a checkerboard-type structure. The extent of the molecular layering can be deduced from the decay of the modulus of the normalized electron density profile. Therefore the decay length values ξ were obtained by fitting an envelope function to the electron density profile. In addition, the reflection pattern calculated within the Parratt algorithm (see Sec. 2.1.6) for a single slab model with up to two interfacial layers was used to fit the data. The number of free fitting parameters was reduced by using the independently determined bulk liquid density values (see Sec. 4.1) as fixed parameters, and the known atomic composition (related to diffraction and absorption) in all models for the interfacial density profile. The raw data were corrected as already discussed in detail in Sec. 3.4.1 by normalizing to the monitored primary beam intensity and applying the foot print correction and background correction. For further analysis the measured reflectivity curves have been normalized by the Fresnel reflectivity from an infinitely sharp interface between the sapphire substrate and the bulk RTIL.

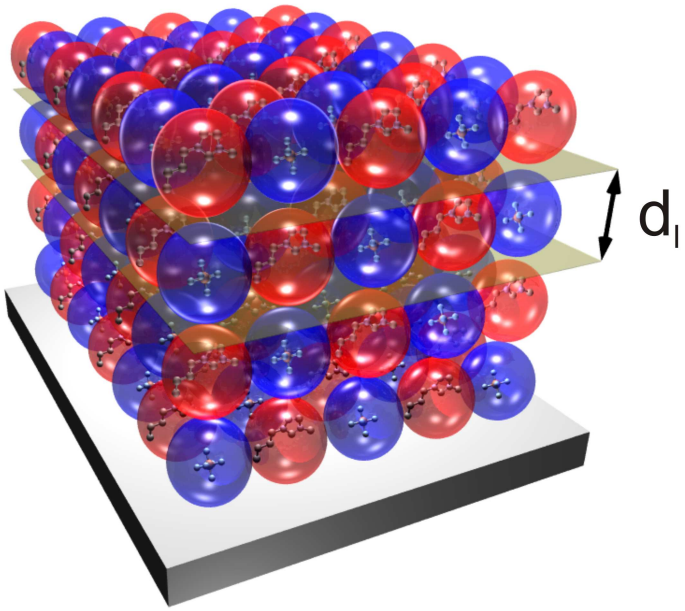

Figure 4.11: Sketch of a checkerboard-type structure of a two-component ionic system. Positive and negative charged particles are indicated by red and blue spheres, respectively. The molecules inside the spheres are not true to scale.

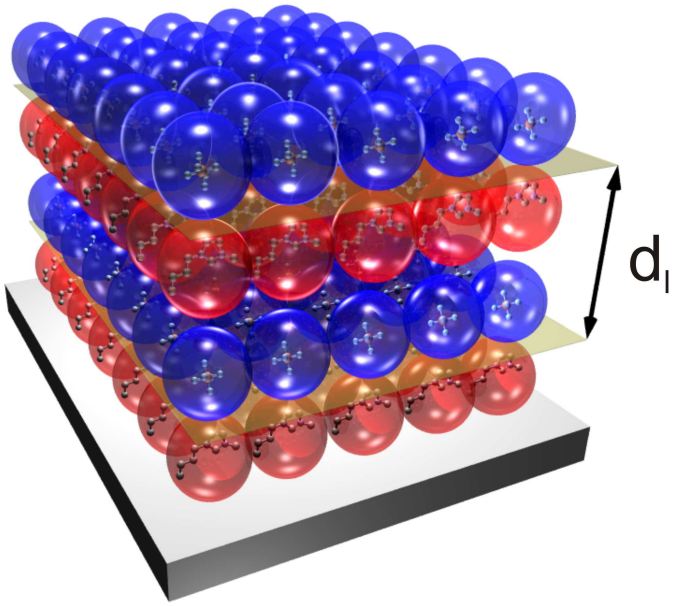

Figure 4.12: Sketch of a double layer arrangement of a two-component ionic system. Positive and negative charged particles are indicated by red and blue spheres, respectively. The molecules inside the spheres are not true to scale.

4.4.1 The [bmim$^+$][BF$_4^-$] - sapphire interface

The reflectivity from the [bmim$^+$][BF$_4^-$] - sapphire interface has been recorded at two different temperatures. One at $T = 110\,^\circ\mathrm{C}$ and a second at $T = -55\,^\circ\mathrm{C}$. The normalized experimental data is shown in Fig. 4.13. The reflectivity decays monotonously with only a change in the slope at $q_z \approx 0.5\,\mathrm{\AA}^{-1}$. The slope in the low q_z part is approximately the same at both temperatures, whereas the slope at large q_z is slightly steeper for the low temperature reflectivity. However, the x-ray reflectivity shows no distinct features indicating molecular layering.

The simplest model which could adequately describe the interface was a single slab model including an interfacial layer with enhanced liquid density as depicted in Fig. 4.13. For the fitting the experimental data in the range $0.26\,\mathrm{\AA}^{-1} < q_z < 1.35\,\mathrm{\AA}^{-1}$ was used. The model parameters obtained by parameter refinement are summarized in Tab. 4.5. The thickness of the interfacial layer $d = 3.9\,\mathrm{\AA}$ at $T = -55\,^\circ\mathrm{C}$ increases with increasing temperature by about $17\,\%$ to $d = 4.7\,\mathrm{\AA}$ at $T = 110\,^\circ\mathrm{C}$. A decrease in temperature leads to an increase of the density of the interfacial layer of about $10\,\%$. The interfacial density is at both temperatures approximately $40\,\%$ higher than the corresponding bulk liquid density. A comparison of these results with the molecular geometry of the ions shown in Fig. 4.13 suggests the segregation of a single molecular layer with an enhanced density to the solid-liquid interface. This is supported by the bulk liquid scattering measurement for [bmim$^+$][BF$_4^-$] (see Sec.) which revealed a strong spatial correlation with a real space distance of $4.3\,\mathrm{\AA}$. The degree of adsorption is

weakened with increasing thermal energy leading to a decrease of the density of the interfacial layer. Larger lateral diffusion and different molecular conformations due to a higher thermal energy are most likely the reason for the increase of the interfacial layer thickness with increasing temperature. The absolute value of the interfacial layer thickness is somewhat smaller than the thickness of $6.5\,\text{Å}$ of a distinct surface layer with modified structure observed with x-ray reflectometry at the solid-vapor interface [15]. This can be explained with the results obtained via direct recoil spectrometry (DRS) and sum-frequency generation spectroscopy (SFG) [13, 35]. These studies report the [bmim$^+$][BF$_4^-$]-vapor interface being composed of an equal amount of cations and anions. The orientation of the imidazolium-ring of the cation with respect to the surface is reported to be perpendicular to the surface plane with the butyl chain sticking into the vapor phase. However, the imidazolium-ring of the cation at the [bmim$^+$][BF$_4^-$] - quartz interface is oriented such that it exhibits a tilt angle between $45°$ and $90°$ with respect to the interface plane as revealed by SFG measurements [103]. The butyl chain is oriented parallel to the interface due to the confined geometry, leading to a smaller interfacial layer thickness at the solid-liquid interface.

Table 4.5: Comparison of the different parameters of the slab model including an interfacial layer for the [bmim$^+$][BF$_4^-$] - sapphire interface at $T = 110\,°\text{C}$ and $T = -55\,°\text{C}$.

		d (Å)	σ (Å)	ρ (g cm^{-3})	$\rho_e r_e$ (10^{-10}cm^{-2})	δ (10^{-8})	β (10^{-12})
$110\,°\text{C}$	bulk		2.09	1.15	10.19	4.74	0.97
	interfacial	4.65	1.56	1.84	16.27	7.56	1.56
$-55\,°\text{C}$	bulk		2.49	1.26	11.16	5.19	1.07
	interfacial	3.86	1.45	2.05	18.17	8.45	1.74

4.4.2 The [bmim$^+$][PF$_6^-$] - sapphire interface

Figures 4.14 and 4.15 show the experimental x-ray reflectivity of the [bmim$^+$][PF$_6^-$] - sapphire interface at $T = 110\,°\text{C}$ and $T = 5\,°\text{C}$. Since [bmim$^+$][PF$_6^-$] exhibits a melting temperature of $T_\text{m} = 12\,°\text{C}$, one measurement was performed far above the melting point and the other one was conducted at a slightly supercooled liquid. The overall structure of the reflectivity shows a monotonous decay with two different slopes similar the reflectivity curves of the [bmim$^+$][BF$_4^-$] - sapphire interface. The change of the slope occurs also at $q_z \approx 0.5\,\text{Å}^{-1}$. However, the reflectivity from [bmim$^+$][PF$_6^-$] displays an additional feature at $q_z \approx 1.0\,\text{Å}^{-1}$ related to a real space periodicity of $2\pi/1.0 = 6.3\,\text{Å}$, indicating the appearance of molecular layering at the interface.

The reflectivities obtained at different temperatures were analyzed employing the DC model as well as the SQ model. The experimental data in the range $0.3\,\text{Å}^{-1} < q_z < 1.2\,\text{Å}^{-1}$ was used for the refinement process with the DC model. For the SQ model, only the data in the range $0.7\,\text{Å}^{-1} < q_z < 1.2\,\text{Å}^{-1}$ was compared to the calculated pattern.

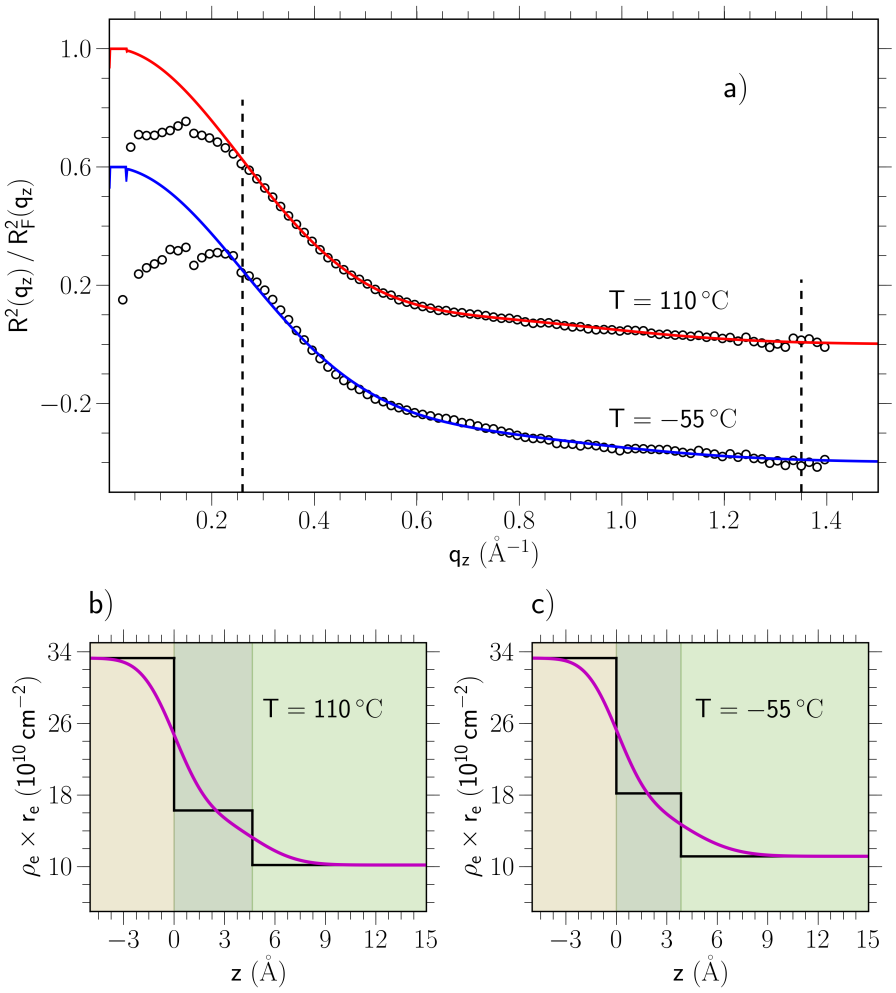

Figure 4.13: a) Comparison of the normalized reflectivity pattern from the [bmim$^+$][BF$_4^-$] - sapphire interface at $T = 110\,^\circ$C (red line) and $T = -55\,^\circ$C (blue line, shifted in vertical direction for clarity). The vertical dashed lines indicate the data range used for fitting. Density profiles reconstructed with a one slab model are shown in b) for $T = 110\,^\circ$C and in c) for $T = -55\,^\circ$C.

The DC model delivers the best fit results with the cation next to the substrate and a full step layer broadening. The use of a single layer model led to unreasonable model parameters and an insufficient match with the experimental data. The calculated reflectivities are compared with the experimental data in Fig. 4.14 for the high temperature and in Fig. 4.15 for the low temperature. Figure 4.16 depicts the obtained density profiles. The corresponding parameters are summarized in Tab. 4.6.

The temperature increase from $T = 5\,^\circ$C to $T = 110\,^\circ$C does not induce a significant change of the reflection pattern, resulting in a constant substrate-first layer offset $d_0 = 3.5\,$Å in this temperature range as retrieved with the DC model. However, the

layer periodicity is increasing by approximately $6\,\%$ with an increase in temperature of $\Delta T = 105\,^{\circ}\mathrm{C}$. The decay length decreases about $15\,\%$ from $T = 110\,^{\circ}\mathrm{C}$ to $T = 5\,^{\circ}\mathrm{C}$. The widths of the first cation and the first anion layer both increase approximately $5\,\%$. The anion layers are slightly shifted away from the substrate such that they are asymmetrically placed between the neighboring cation layers. Although the shift Δ_s is very small, its impact on the quality of the fit result is dramatic. The shift Δ_s is increasing with decreasing temperature.

The SQ model led to a reflectivity which reproduces the experimental data only for $q_z > 0.7\,\mathrm{\AA}^{-1}$. However, the temperature behavior of the layer periodicity as retrieved by the DC model is confirmed by the results of the SQ approach with only slightly different absolute values. The decay length obtained from the SQ model is identical for the low temperature to the value of the DC fit, but decreases with increasing temperature. It has to be noted that the meaning of the parameter d_0 is different for the DC and the SQ model. Therefore, the d_0 values of the different models cannot be compared. For the [bmim$^+$][PF$_6^-$] - vapor interface by x-ray reflectivity a distinct layer of $5.8\,\mathrm{\AA}$ thickness is found [15]. Interestingly, a spatial correlation in the bulk RTIL with a dominant distance of $6.4\,\mathrm{\AA}$ was found at $T = -20\,^{\circ}\mathrm{C}$ (see Sec. 4.3). That distinct correlation length was assigned to centroid-centroid interactions of the cations. This suggests that the layer periodicity measured at the solid-liquid interface corresponds to a double layer structure rather than a checkerboard-type arrangement.

Table 4.6: Comparison of the different parameters obtained from the reflectivity data of the [bmim$^+$][PF$_6^-$] - sapphire interface via DC model and SQ model. All units are in ($\mathrm{\AA}$) except for the ratio ξ/d_l and the amplitude A (dimensionless).

		d_0	d_l	ξ/d_l	σ_b	σ_s	σ_c	σ_a	Δ_s	A
$110\,^{\circ}\mathrm{C}$	DC	3.5	6.9	1.5	1.3	2.5	1.7	2.0	0.14	
	SQ	0.2	6.4	1.0		1.1				0.2
$5\,^{\circ}\mathrm{C}$	DC	3.5	6.5	1.2	1.4	2.9	1.8	2.1	0.26	
	SQ	0.2	6.3	1.2		1.0				0.2

4.4.3 Comparison between [bmim$^+$][BF$_4^-$] and [bmim$^+$][PF$_6^-$]

The shape of the x-ray reflectivity of the [bmim$^+$][BF$_4^-$] - sapphire interface suggests the presence of a liquid layer with enhanced density adsorbed to the substrate. The density profile of the [bmim$^+$][PF$_6^-$] - sapphire interface reconstructed from the corresponding reflection pattern, indicates the presence of molecular layering which decays into the bulk liquid with a decay length of $1.5\,d_l$.

Since both RTILs contain the same cation the change in the interfacial behavior is caused by the different anions. The bulk liquid structure changes accordingly upon exchanging the anion which could be deduced from the bulk liquid scattering experiments. Surprisingly, the surface tension is equal for both RTILs within the error of the measurement (see Sec. 4.1). Another property which depends significantly on the choice of the

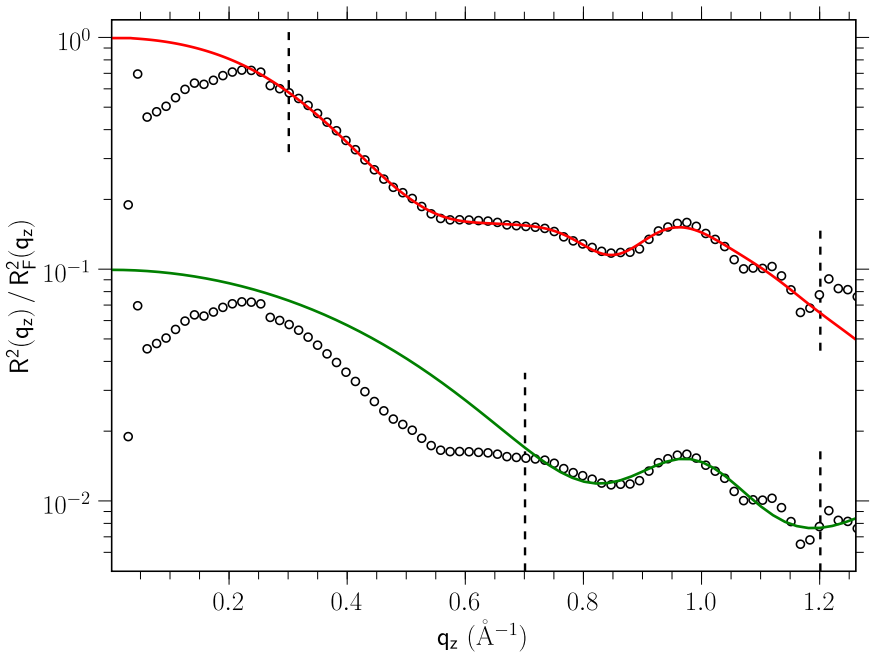

Figure 4.14: Normalized reflectivity data of the [bmim$^+$][PF$_6^-$] - sapphire interface obtained at $T = 110\,^\circ$C together with the calculated reflectivity of the DC model (red line) and of the SQ model (green line). The latter is shifted by an order of magnitude for clarity.

anion is the miscibility with water. While [bmim$^+$][BF$_4^-$] is totally miscible with water [bmim$^+$][PF$_6^-$] is not [104]. It is obvious that the water miscibility depends crucially on the choice of the anion. It was therefore concluded that [PF$_6^-$] is more hydrophobic than [BF$_4^-$]. Romero et al. [8] investigated the structural arrangement of [bmim$^+$] based RTILs at hydrophilic surfaces with SFG. The OH groups of the hydrophilic substrate form weak hydrogen bonds with the nitrogen atoms of the imidazolium ring. The authors also observed that the anion is adsorbed to the hydrophilic surface, resulting in a tilt of the cation towards the surface normal. Since the [BF$_4^-$] anion is hydrophilic it should be more attracted towards polar groups which in our case are the polar C(2)-H group on the imidazolium ring and the Al-O-H groups of the hydrophilic substrate. The strong coupling between the [BF$_4^-$] and the polar C(2)-H group of the imidazolium ring is confirmed by a x-ray crystallographic analysis of [bmim$^+$][Cl$^-$], which is also fully miscible with water [105]. The anion size increases from [BF$_4^-$] with a B-F bonding length of about 1.4 Å [106] to [PF$_6^-$] with a P-F bonding length of about 1.5 Å. The larger the anions, the more delocalized are their charge. This is reflected by an increase of the ionic radius which is 2.29 Å for the [BF$_4^-$] and 2.54 Å for the [PF$_6^-$] as reported by Romero et al. [103]. This implies that the cation-anion attraction in [bmim$^+$][PF$_6^-$] is weaker than in [bmim$^+$][BF$_4^-$] and that the [PF$_6^-$] anion is less attracted to the hydrophilic substrate due to its hydrophobic character. However, the double layer structure leads to cations sitting next to each other and clearly repelling each other. The additional

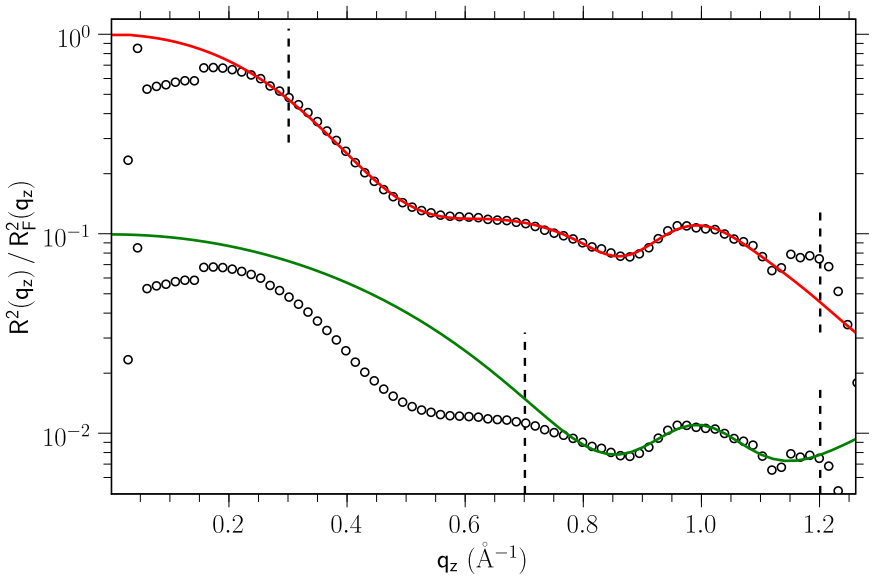

Figure 4.15: Normalized reflectivity data of the [bmim$^+$][PF$_6^-$] - sapphire interface obtained at $T = 5\,^\circ\mathrm{C}$ together with the calculated reflectivity of the DC model (red line) and of the SQ model (green line). The latter is shifted by an order of magnitude for clarity.

interaction which may stabilize such a configuration are the hydrogen bonds of the OH groups of the substrate with the nitrogen atoms of the imidazolium rings. An interdigitation of the following anion layer with the cation layer could further stabilize such a system. It has also to be noted that the structure of crystallized [bmim$^+$][PF$_6^-$] showed a layered channel arrangement with cations opposed to each other (see Fig. 4.9). This indicates that the tendency to form charge arrangements necessary to build up a double layer structure is already present in the bulk liquid structure. Obviously, the more confined geometry at the solid-liquid interface with additional interactions between the ions and the substrate promotes the formation of a layered structure further.

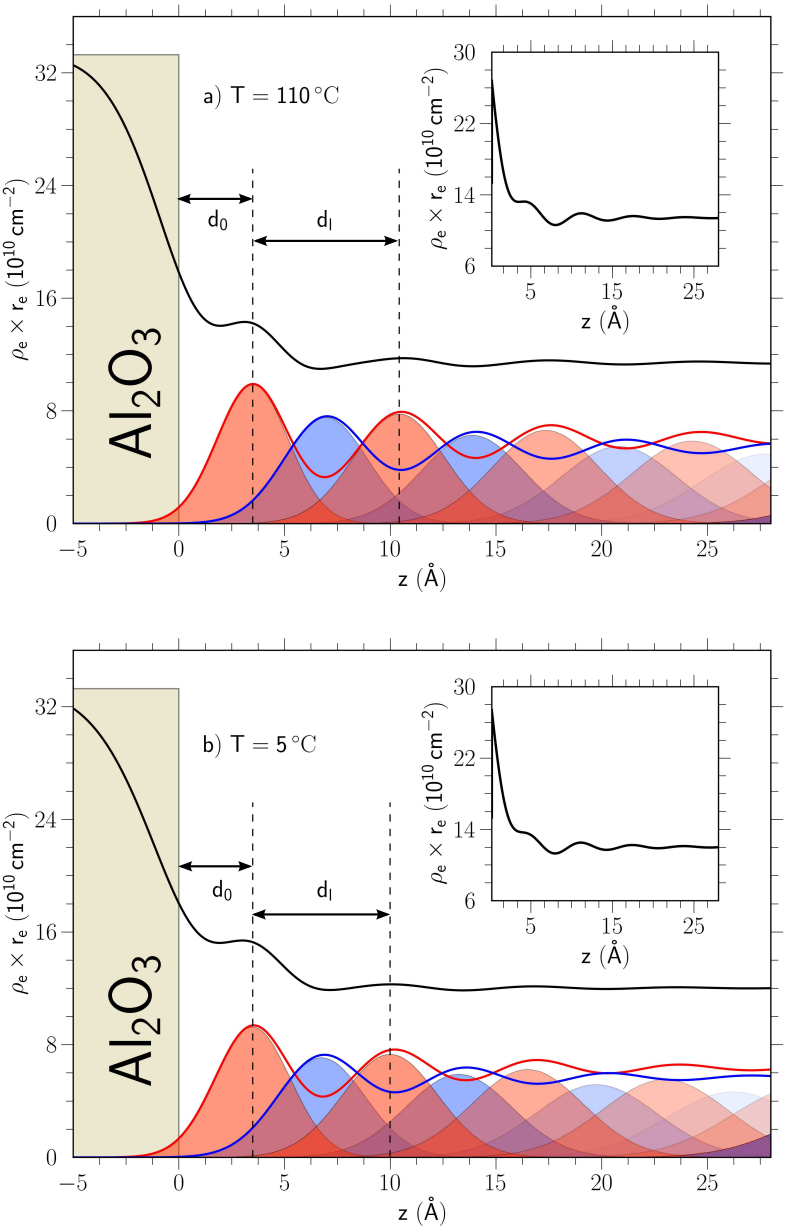

Figure 4.16: Electron density profiles of the [bmim$^+$][PF$_6^-$] - sapphire interface reconstructed from fits of the DC model for a) $T = 110\,^{\circ}\mathrm{C}$ and b) $T = 5\,^{\circ}\mathrm{C}$. The partial electron density profiles of the ions (red line: cations, blue line: anions) are shown together with the respective Gaussian distributions. The profiles obtained with the SQ model are shown in the respective insets.

4.4.4 The [hmim$^+$][Tf$_2$N$^-$] - sapphire interface

The results of the x-ray reflectivity measurements at the [hmim$^+$][Tf$_2$N$^-$] - sapphire interface at $T = 110\,^\circ\mathrm{C}$ and $T = -20\,^\circ\mathrm{C}$ are shown in Fig. 4.17. The RTIL exhibits a melting point of $M_p = -9\,^\circ\mathrm{C}$, thus one measurement was performed far above the melting point and the other one slightly beneath. The most essential features of the reflection pattern are two smooth dips, one located at $q_z \approx 0.3\,\mathrm{\AA}^{-1}$ and another one at $q_z \approx 0.9\,\mathrm{\AA}^{-1}$. The temperature variation of $\Delta T = 130\,^\circ\mathrm{C}$ led to no significant modification of these features as well as the overall structure. For the fitting the experimental data in the range $0.2\,\mathrm{\AA}^{-1} < q_z < 1.25\,\mathrm{\AA}^{-1}$ was used. The analysis of the reflectivity with the SQ model failed to reproduce the measured curves. However, with the DC model in the full step configuration and the first ion layer consisting of cations it was possible to reproduce the experimental data precisely. The corresponding parameters are summarized in Tab. 4.7 and the corresponding density profiles for both temperatures are shown in Fig. 4.18. Fitting the experimental data with a single layer model led to unphysical parameters and a poor agreement with the measured reflectivity curve.

The parameters obtained via the DC model clearly mirror the fact that the experimental reflectivity shows no significant alteration with temperature. The offset between substrate and the first ion layer stays constant within the error of the fitting routine and so do the widths of the first cation layer and first anion layer. A slight change was found for the layer periodicity and consequently for the decay length. d_l decreases by about $1\,\%$ and ξ/d_l increases approximately $3\,\%$ with the temperature decreasing from $T = 110\,^\circ\mathrm{C}$ to $T = -20\,^\circ\mathrm{C}$. Since the volumetric thermal expansion coefficient of [hmim$^+$][Tf$_2$N$^-$] is $\gamma = 6 \cdot 10^{-4}\,\mathrm{K}^{-1}$ (see section 4.1), the bulk liquid expands in one dimension about $2.6\,\%$ with an increase of $\Delta T = 130\,^\circ\mathrm{C}$. Thus, the increase of the layer periodicity is readily explained by the thermal expansion of the bulk liquid.

Table 4.7: Comparison of the parameters obtained from the reflectivity of the [hmim$^+$][Tf$_2$N$^-$] - sapphire interface via the DC model. The units are in (Å) except for ratio ξ/d_l (dimensionless).

		d_0	d_l	ξ/d_l	σ_b	σ_s	σ_c	σ_a	Δ_s
$110\,^\circ\mathrm{C}$	DC	1.8	6.5	1.1	1.5	2.2	1.5	1.8	0.39
$-20\,^\circ\mathrm{C}$	DC	1.8	6.4	1.1	1.4	2.2	1.6	1.8	0.32

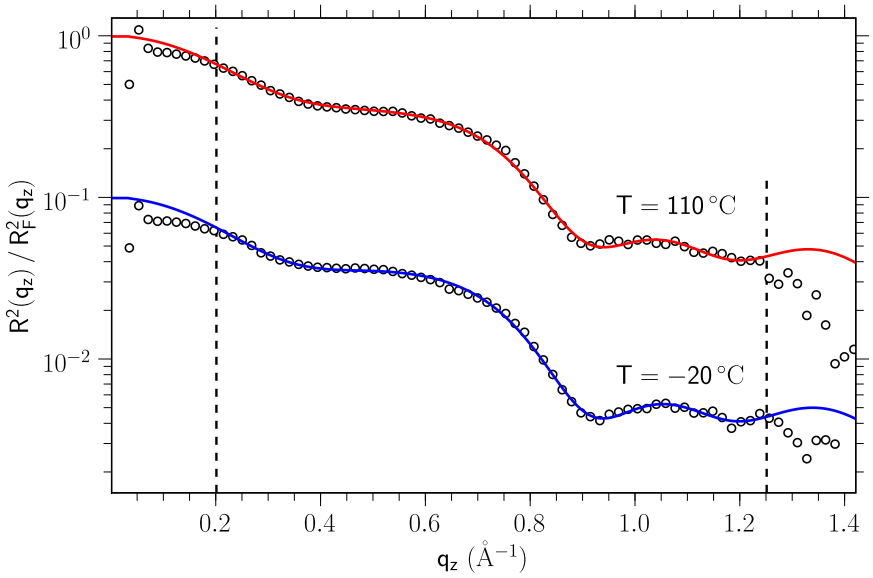

Figure 4.17: Normalized experimental reflectivity of the [hmim$^+$][Tf_2N^-] - sapphire interface (black circles) at $T = 110\,^{\circ}\mathrm{C}$ and $T = -20\,^{\circ}\mathrm{C}$ together with the best fit results obtained with the DC model (red line: $T = 110\,^{\circ}\mathrm{C}$; blue line: $T = -20\,^{\circ}\mathrm{C}$). No temperature dependence of the reflectivity pattern was observed.

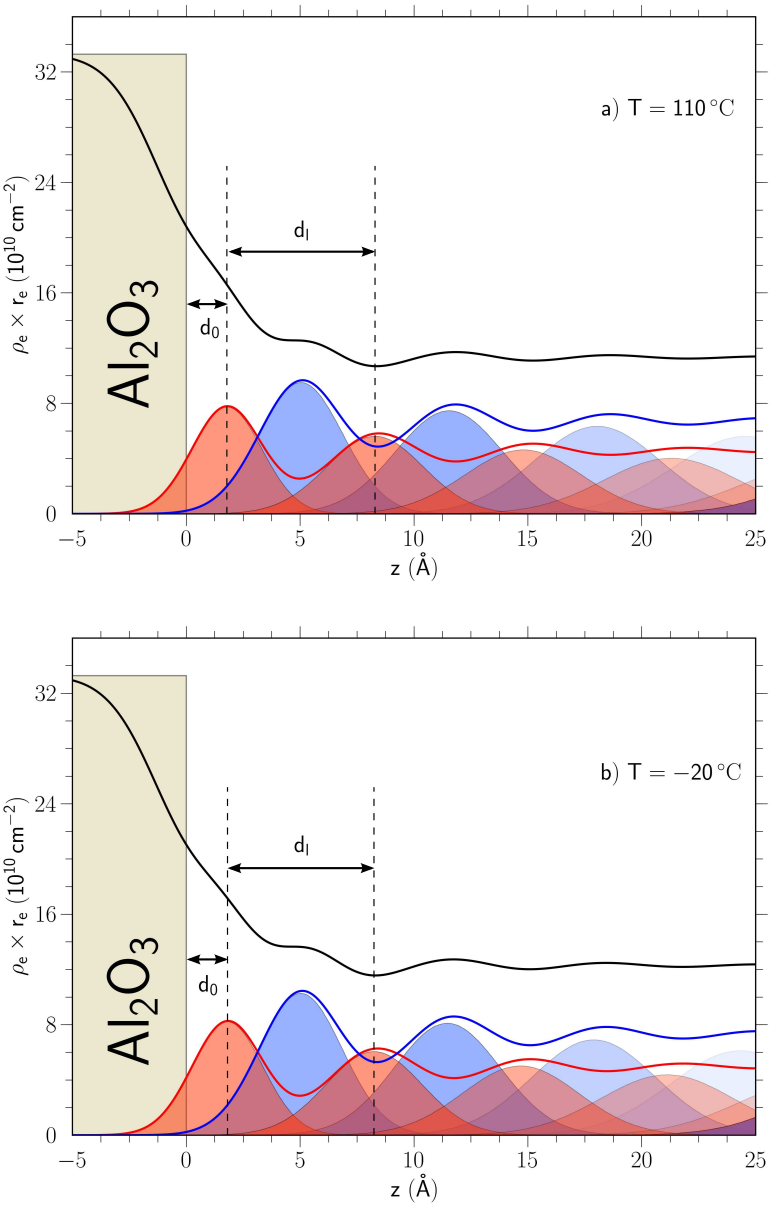

Figure 4.18: Reconstructed electron density profiles (DC model, black line) of the [hmim$^+$][Tf_2N^-] - sapphire interface at a) $T = 110\,^{\circ}\mathrm{C}$ and b) $T = -20\,^{\circ}\mathrm{C}$. The partial electron density profiles of the ions (red line: cations, blue line: anions) are shown together with the respective Gaussian distributions.

4.4.5 The [bmpy$^+$][Tf$_2$N$^-$] - sapphire interface

The reflection pattern of the interface between dry [bmpy$^+$][Tf$_2$N$^-$] and sapphire has been studied at two different temperatures: At $T = 110\,^\circ\mathrm{C}$ far above the melting temperature $T_m = -6\,^\circ\mathrm{C}$ and at $T = -20\,^\circ\mathrm{C}$ (slightly supercooled). In addition, the interface between sapphire and [bmpy$^+$][Tf$_2$N$^-$] saturated with water was investigated at $T = 2\,^\circ\mathrm{C}$. Figures 4.19 and 4.20 show the experimentally recorded x-ray reflectivity pattern of the dry RTIL at $T = 110\,^\circ\mathrm{C}$ and at $T = -20\,^\circ\mathrm{C}$, respectively. The most prominent feature of these curves are a Lorentzian-shaped dip at $q_z \approx 1.05\,\text{Å}^{-1}$. At the high temperature this dip is deeper with a smaller width compared to a broader less pronounced dip in the reflectivity recorded at the low temperature.

For the dry samples the DC model yielded the best fit result in the full step configuration with a cation layer next to the substrate. The overall shape of the experimental data could also be described with the SQ model. The full step DC model with an anion layer next to the substrate resulted in poor fits with the experimental data and unphysical values for the free model parameters. With the cation next to the substrate the half step DC model led to an unacceptable result. In another approach to reconstruct the density profile a single layer DC model was fitted to the experimental data. However, the measured reflectivity could not be reproduced by such a model. The reflectivity from the RTIL saturated with water could be fitted using a single slab model including an interfacial layer.

High temperature

The experimental reflectivity curve obtained at $T = 110\,^\circ\mathrm{C}$ was fitted with the modified distorted crystal model with several different parameter settings. The best fit result was obtained with the full step model and the first layer next to the substrate consisting of cations. Figure 4.19 shows the results of this fit and the experimental reflectivity. For the parameter refinement the experimental data in the range of $0.15\,\text{Å}^{-1} < \mathrm{q} < 1.35\,\text{Å}^{-1}$ has been used. The parameters obtained with the DC full step model and the cation in the vicinity of the substrate are discussed in the following. The center of the first ion layer is located at $d_0 = 1.86\,\text{Å}$ away from the sapphire substrate. The periodicity of the layering was determined to $d_l = 6.48\,\text{Å}$. The widths of the first Gaussian density distributions are $\sigma_c = 1.2\,\text{Å}$ for the cations and $\sigma_a = 1.6\,\text{Å}$ for the anions. The broadening $\sigma_b = 2.4\,\text{Å}$ leads to a decay length for the layering of $\xi = 3.3\,\text{Å} = 0.5\,d_l$. The substrate roughness is $\sigma_s = 2.0\,\text{Å}$. The reconstructed total density profile together with the ion Gaussian density distributions of the ion layers are shown in Fig. 4.21. The profile indicates clearly the fact that the layering decays after approximately half a layer periodicity. Only the first two Gaussians are rather sharp displaying a real charge separation. The third Gaussian layer is already significantly broadened resembling a blurred charge separation.

The employment of the SQ model to the same experimental data range as mentioned before leads to a calculated reflectivity which coincides well with the experimental data. The result is shown in Fig. 4.19 (green line). The overall shape of the two calculated reflectivities, one obtained with the DC model and the second obtained with the SQ

model, is similar. The only significant deviation can be observed around the region of the dip at $q_z \approx 1.1\,\text{Å}$. This is most likely the reason for the slightly different layer periodicity of $d_l = 6.3\,\text{Å}$ obtained within the SQ model, since the position of the dip q_z^d is related to the real space layer periodicity by $d_l = 2\pi/q_z^d$. The decay length $\xi = 3.6\,\text{Å} = 0.6\,d_l$ determined with the SQ approach coincides well with values obtained by the DC model. Only the substrate roughness $\sigma_s = 2.7\,\text{Å}$ is significantly larger. This is most likely an artefact of the simpler SQ model, since the Fresnel reflectivity of a substrate with such a large roughness would decay much faster with q_z, such that it would be impossible to measure the reflection pattern to such high q values. All parameter values are summarized in Tab. 4.8 together with the values obtained for the low temperature measurement. It has to be noted that the meaning of the parameter d_0 is different for the DC and the SQ model. Therefore, the d_0 values of the different models cannot be compared.

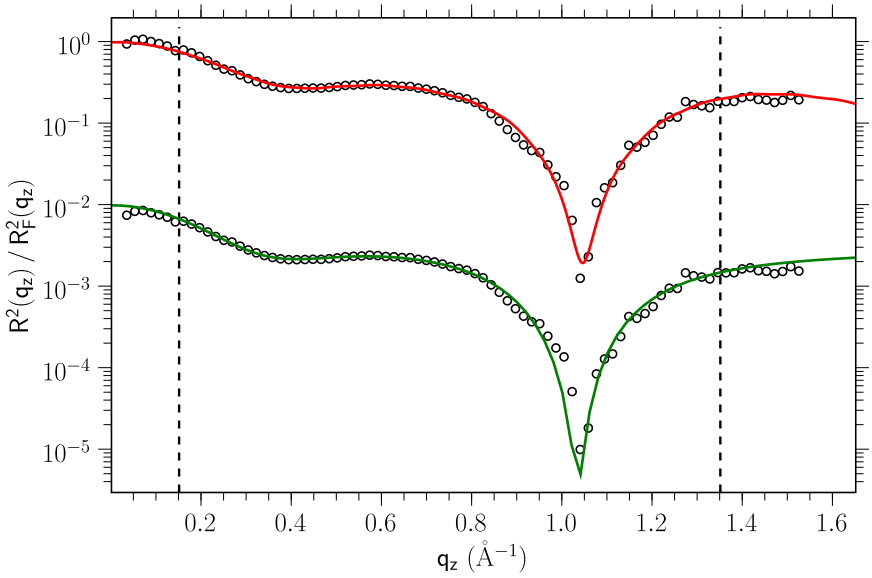

Figure 4.19: Normalized reflectivity of the [bmpy$^+$][Tf$_2$N$^-$]-sapphire interface at $T = 110\,°\text{C}$ together with the best fit obtained with the DC model (red line) and the fit result of the SQ model (green line; data and fit are shifted by 2 orders of magnitude for clarity).

Low temperature

The reflectivity obtained at $T = -20\,°\text{C}$ is also best reproduced by the DC full step model with cations next to the substrate (see Fig. 4.20). The experimental data in the range of $0.25\,\text{Å}^{-1} < \text{q} < 1.50\,\text{Å}^{-1}$ has been used for the fit process. The resulting parameters have the following values: the center of the first ion layer is located at $d_0 = 1.1\,\text{Å}$, the periodicity of the layering is $d_l = 5.6\,\text{Å}$, the width of the first cation layer Gaussian density distribution is $\sigma_c = 1.1\,\text{Å}$ and $\sigma_a = 1.6\,\text{Å}$ for the anions. The broadening is $\sigma_b = 2.0\,\text{Å}$ with an associated decay length of $\xi = 3.1\,\text{Å} = 0.6\,d_l$, and the

substrate roughness $\sigma_s = 1.7\,\text{Å}$. The corresponding electron density profile is shown in Fig. 4.21.

The analysis of the low temperature data with the SQ model resulted in the following parameter values: layer periodicity $d_l = 6.4\,\text{Å}$, decay length $\xi = 2.4\,\text{Å} = 0.4\,d_l$, substrate roughness $\sigma_s = 2.1\,\text{Å}$. The reflectivity curve calculated from the fitted model is shown in Fig. 4.20. The model describes the experimental reflectivity up to a vertical momentum transfer $q_z \approx 1.4\,\text{Å}^{-1}$ quite well. For $q_z > 1.4\,\text{Å}^{-1}$ the experimental data show a slight decrease in the intensity, which is not reproduced by the SQ model. The DC model describes the reflectivity in the high-q regime much better. However, the deviation is still larger than in the low-q regime. The values for the layer periodicity obtained the two models deviate by about $13\,\%$ from each other. The decay lengths are also quite different.

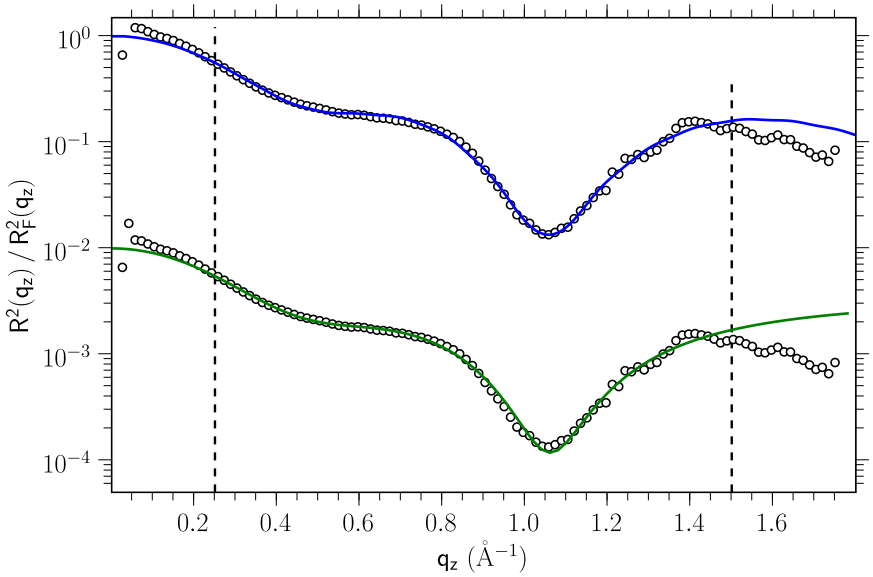

Figure 4.20: Normalized reflectivity of the [bmpy$^+$][Tf$_2$N$^-$]-sapphire interface at $T = -20\,^\circ\text{C}$ together with the best fit obtained with the DC model (blue line) and the fit result of the SQ model (green line; data and fit are shifted by 2 orders of magnitude for clarity).

Comparison of the reflectivity at low and high temperature

The distance between the substrate and the center of the first ion layer increases by $\Delta d_0/d_0 \approx 39\,\%$ with increasing temperature (see Tab. 4.8). This is in contrast to x-ray reflectivity results from an interface between sapphire and a RTIL which contains the same cation but a different anion, tris(pentafluoroethyl) trifluorophosphate [FAP$^-$] [63]. These findings manifest once more that the properties of RTILs are strongly dependent on their anion-cation combination rather than a single cation or anion type.

The volumetric thermal expansion coefficient of [bmpy$^+$][Tf$_2$N$^-$] is $\gamma = 6{\cdot}10^{-4}\,\text{K}^{-1}$ (see Sec. 4.1). A change in temperature of $\Delta T = 130\,^\circ\text{C}$ leads to a relative decrease of

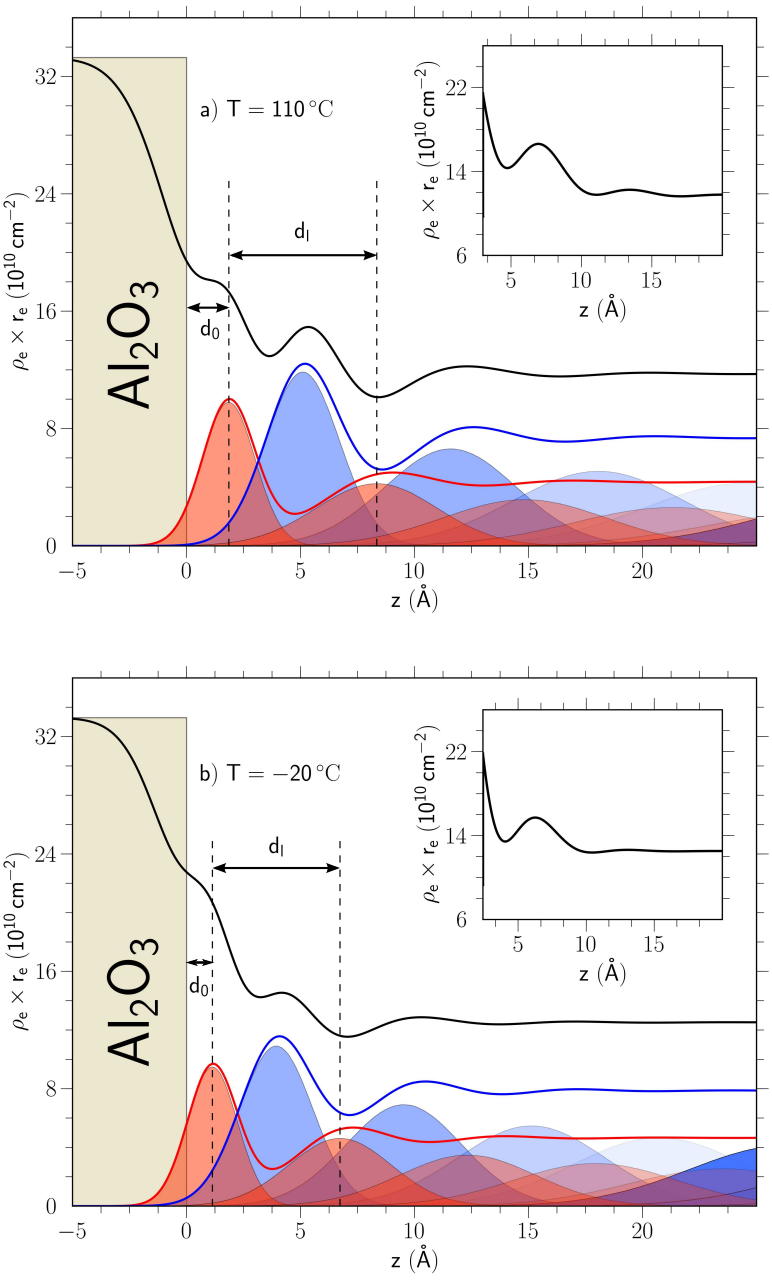

Figure 4.21: Electron density profiles of the [bmpy$^+$][Tf_2N^-]-sapphire interface at $T = 110\,°C$ and at $T = -20\,°C$ deduced from the best fit with the DC model. Also the partial electron density profiles of the ions (red line: cations, blue line: anions) are shown together with the respective Gaussian distributions. The profiles obtained with the SQ model are shown in the respective insets.

Table 4.8: Comparison of the parameters obtained from the reflectivity of the [bmpy$^+$][Tf$_2$N$^-$] - sapphire interface via the DC model and the SQ model. The units are in (Å) except for ratio ξ/d_l and the amplitude A (dimensionless).

		d_0	d_l	ξ/d_l	σ_b	σ_s	σ_c	σ_a	Δ_s	A
$110\,^\circ\mathrm{C}$	DC	1.9	6.5	0.5	2.4	2.0	1.2	1.6	0.0	
	SQ	3.0	6.3	0.6		2.7				0.5
$-20\,^\circ\mathrm{C}$	DC	1.1	5.6	0.6	2.0	1.7	1.1	1.6	0.11	
	SQ	2.4	6.4	0.4		2.1				0.7

the bulk liquid density of $\Delta\rho/\rho \approx 7.7\,\%$. Since the volumetric and the linear thermal expansion coefficient for a liquid are related by $\gamma \approx 3\alpha$, the expansion in one dimension is about $2.6\,\%$. However, the layer periodicity changes by about $13.6\,\%$ in this temperature range. Thus, the change of the layer periodicity is not only caused by the thermal expansion of the liquid. The slightly higher decay length at low temperature indicates the impact of the thermal energy. As one would expect the increase in temperature leads to a higher thermal energy and therefore to an increase in entropy. Since the layering can be considered as an ordered structure with lower entropy compared to the disordered bulk liquid, an increase in the entropy should lead to a less ordered arrangement, thus a faster decay. In addition, the interaction between the hydrophilic substrate and the first ion layer increases with decreasing temperature as clearly indicated by the substrate to first layer distance d_0. These interactions, most likely hydrogen bonds and van der Waals interactions, drive the layering process, thus balancing the cation-anion attraction and the cation-cation/anion-anion repulsion. On the other hand, the layering feature in the experimental data is much more pronounced at high temperature. The layering feature depends on the ratio of d_0/d_l. This is supported by calculating the reflectivity curve for different d_0 values (see Fig. 4.22). The width of the first anion layer does not change in the investigated temperature range. The width of the first cation layer increases by about $4.3\,\%$ which is not significant.

High water content

A drop of the RTIL was placed for $12\,\mathrm{h}$ in liquid water at room temperature. The maximum possible water uptake for [bmpy$^+$][Tf$_2$N$^-$] was reported to be $14800\,\mathrm{ppm}$ [12]. This drop was then placed on top of a sapphire substrate. The interface was investigated by x-ray reflectivity at a temperature of $T = 2\,^\circ\mathrm{C}$. The recorded x-ray reflectivity curve is shown in Fig. 4.23. The reflectivity shows no features indicating molecular layering at the interface. The monotonous decay can be adequately described with a single slab model including an interfacial layer with an enhanced density similar to the one used for the [bmim$^+$][BF$_4^-$] - sapphire interface. For the fitting the experimental data in the range $0.15\,\text{Å}^{-1} < q_z < 1.15\,\text{Å}^{-1}$ was used. The reconstructed density profile is shown in Fig. 4.23 and the corresponding parameters are summarized in Tab. 4.9. The $3.3\,$Å thick interfacial layer exhibits a density which is about $31\,\%$ higher than the one of the bulk

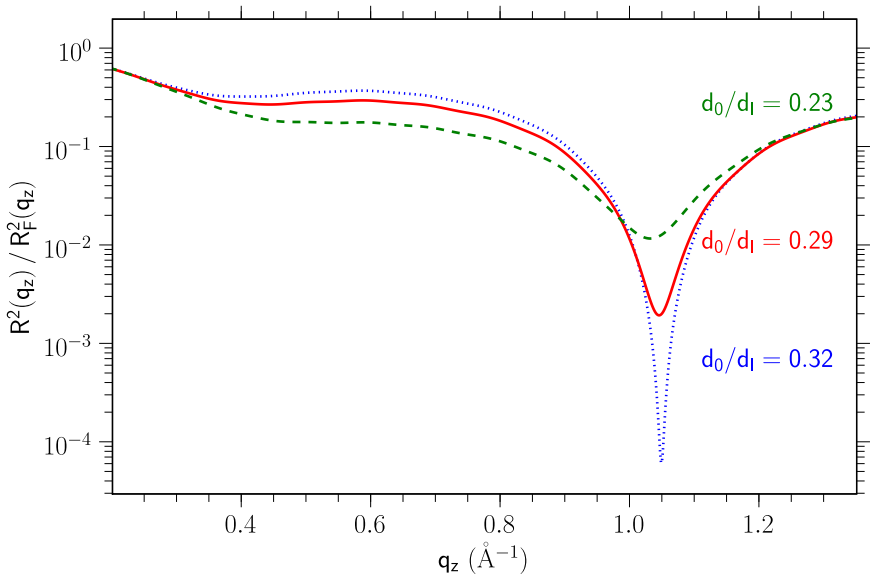

Figure 4.22: Calculated reflectivity curves for different ratios of d_0/d_l with otherwise the same parameters as for the reflectivity of the [bmpy$^+$][Tf$_2$N$^-$]-sapphire interface at $T = 110\,^\circ$C. The ratio $d_0/d_l = 0.29$ (red line) corresponds to the best fit of the experimental reflectivity curve.

liquid. For the liquid drop the corresponding bulk liquid scattering (see Sec. 4.3) has also been measured. Interestingly the scattered intensity did not indicate altered spatial correlations in the investigated momentum transfer range whereas the molecular layering at the solid-liquid interface vanished. One possible explanation is that the water did not diffuse into the bulk liquid during the exposure time of 12 h, since [bmpy$^+$][Tf$_2$N$^-$] is known to be rather hydrophobic [11, 12]. Since the maximum water uptake is only 14800 ppm it is most likely that such a small water content does not change the bulk liquid correlations. On the other hand, it is a well establish fact that even small amounts of impurities (in the ppm range) lead to significant changes in the surface and interface structures.

Table 4.9: Comparison of the different parameters of the slab model including an interfacial layer [bmpy$^+$][Tf$_2$N$^-$]-sapphire interface saturated with water at $T = 2\,^\circ$C.

	d (Å)	σ (Å)	ρ (g cm^{-3})	$\rho_e r_e$ (10^{-10}cm^{-2})	δ (10^{-8})	β (10^{-12})
bulk		1.8	1.4	12.4	5.7	4.3
interfacial	3.3	1.3	2.0	17.8	8.3	6.3

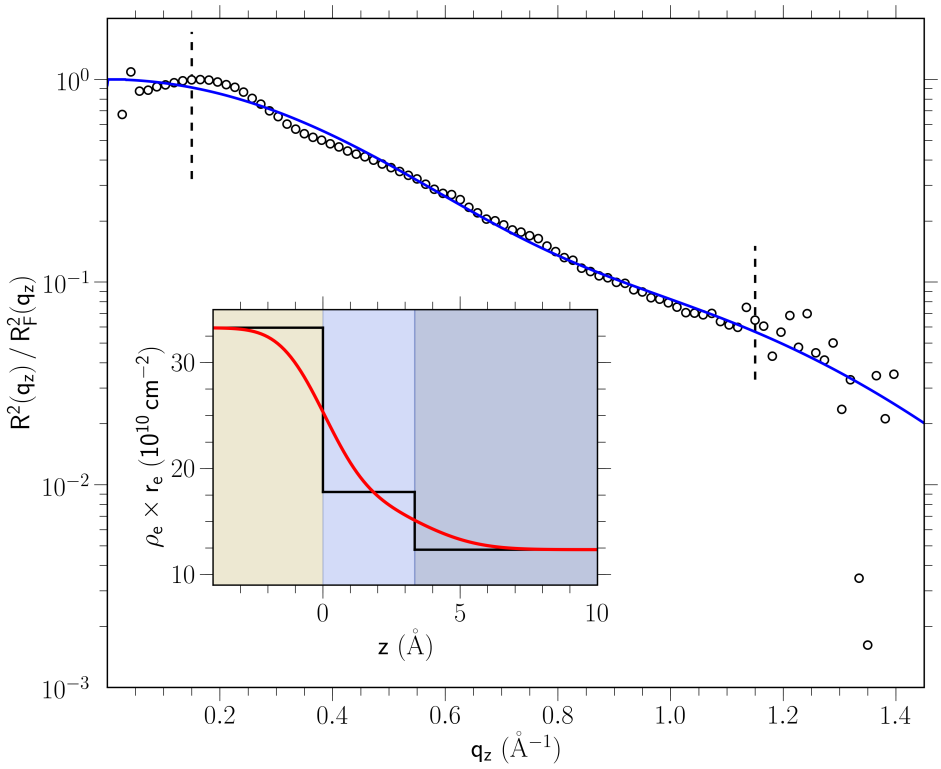

Figure 4.23: Normalized reflectivity of the [bmpy$^+$][Tf$_2$N$^-$]-sapphire interface, where the RTIL was saturated with water. The inset shows the corresponding density profile reconstructed with a single slab model at the interface.

4.4.6 Comparison between [hmim$^+$][Tf$_2$N$^-$] and [bmpy$^+$][Tf$_2$N$^-$]

Both RTILs show a molecular layering at the solid-liquid interface with similar layering periodicities of about 6.5 Å and comparable substrate to first cation layer distances at $T = 110\,^{\circ}\mathrm{C}$. Typical distances deduced from the bulk liquid scattering for both RTILs are about 4.8 Å and 7.5 Å. The observed layering periodicity lies in between, but closer to the cation centroid-centroid distance.

The electron density distribution of the [hmim$^+$][Tf$_2$N$^-$]-sapphire interface shows no significant temperature dependence in the investigated temperature range. On the other hand, [bmpy$^+$][Tf$_2$N$^-$] exhibits a rather pronounced temperature-dependent behavior near the solid-liquid interface. A similar pronounced temperature-dependence was found for [bmpy$^+$][FAP$^-$] at a sapphire interface [63]. This clearly suggests a high impact of the cation of a RTIL on the temperature-dependent behavior near a solid-liquid interface.

The temperature behavior of the [bmpy$^+$] cation might be caused by a change of its conformation with temperature. For the pyrrolidinium the existence of conformers with different structural conformation energies has indeed been reported [107]. One of the conformations exhibits a global minimum of the structural conformation energy. The other conformers have higher structural conformation energies ranging from

$\Delta E = 35\,\mathrm{meV}$ to $\Delta E = 150\,\mathrm{meV}$. A temperature increase of $\Delta T = 130\,^{\circ}\mathrm{C}$ corresponds to an energy increase of about $11\,\mathrm{meV}$. Recalling that a Maxwell-Boltzmann distribution holds for the motion of the molecules, it seems possible that a conformational change of the pyrrolidinium ring is induced by that temperature variation. Since mainly the pyrrolidinium ring carries the positive charge of the respective cation, the ionic interactions primarily take place at the pyrrolidinium ring. And as already mentioned, the coulomb interactions present in the investigated RTILs have a major impact on the structural order of these liquids. Therefore, it is suggested that the RTIL structure is affected by the energetic accessible conformers of the pyrrolidinium ring. In the case of imidazolium-based cations only one ring conformation exists, making the structural impact of the imidazolium ring temperature independent. This suggestion is supported by the fact that the DC model retrieved in the case of [bmpy^{+}][Tf_2N^{-}] for the width of the first cation Gaussian a decrease with decreasing temperature, opposed by a temperature independent first anion Gaussian width.

Chapter 5

Conclusions

In this work a high energy x-ray reflectivity study of interfaces between RTILs and a hard wall is reported. For the first time the interfacial structure was obtained with molecular resolution. The thorough analysis of the experimental reflectivities gives clear evidence of a pronounced molecular layering at the RTIL-solid interface. The periodicity of the molecular layering corresponds to correlation distances in the bulk liquid RTILs. The values of the surface tension seem to be unrelated to the interfacial structure.

Four different RTILs were studied. Two of them share the same cation, [bmim$^+$], with the most widely used and extensively studied anions, [BF_4^-] and [PF_6^-]. The other two RTILs fall into a more recent class of RTILs with higher electrochemical stability. They share the same anion, [Tf_2N^-], and a pyrrolidinium-based and an imidazolium-based cation, respectively. The systematic exchange of the ion types within these four RTILs revealed a distinct impact of the ion pair on the interfacial behavior.

Further information on interactions within the probed systems was gained by measurements of the interfacial tensions with air and n-hexane for all four RTILs at ambient condition. The surface tension of the RTILs is higher than the one for n-hexane but still smaller than the one for water. The measurements revealed that small changes in the nature of the ions have only a minor impact on the value of the surface and interfacial tension. The results suggest that the RTIL-vapor and RTIL-n-hexane interface is composed of similar amounts of cations and anions, thus no charge separation occurs at the RTIL-vapor interface.

In order to correlate the results for the interfacial structures with the bulk properties of the RTILs, bulk liquid x-ray scattering experiments were carried out at all four RTILs. These measurements revealed the presence of significant spatial correlations. In all cases, correlations assigned to the cation ring-ring distance or the first solvation shell of the anion were observed. A distinct feature indicating cation centroid-centroid correlation distance or cation-cation distance was identified in the bulk liquid scattering of [bmim$^+$][PF_6^-], [hmim$^+$][Tf_2N^-], and [bmpy$^+$][Tf_2N^-]. The imidazolium-based RTILs showed an additional feature in the low q range. As supported by literature this was assigned to medium range correlations of the alkyl chains of the cations. The temperature dependence of the correlations present in the respective RTILs is insignificant. The comparison of the correlation distances of the liquid state with the distances determined in

the crystalline state for [bmim$^+$][PF_6^-] suggests the existence of a substantial degree of order even in the liquid state, resembling the crystalline order. Thus, the charge ordered structure of the crystalline phase is partially preserved in the liquid state. In the case of [bmpy$^+$][Tf_2N^-], saturation with water did not change the correlation distances in the bulk liquid scattering.

The x-ray reflectivity measurements gave firm evidence for an exponentially damped molecular layering in charge-separated double layers at a sapphire substrate in the case of [bmim$^+$][PF_6^-], [hmim$^+$][Tf_2N^-], and [bmpy$^+$][Tf_2N^-] with a layering periodicity of approximately $6.5\,\text{Å}$. For [bmim$^+$][BF_4^-], no layering was observed in the investigated q range. [bmim$^+$] [PF_6^-] exhibits the most extended layering with a decay length of approximately 1.5 layer spacings. A less pronounced layering is observed for [hmim$^+$][Tf_2N^-] with a decay length of about 1.1 layer spacings. In the case of [bmpy$^+$][Tf_2N^-], the layering shows a decay length of approximately 0.5 layer spacings. A significant temperature dependence of the x-ray reflectivity of the RTIL-sapphire interface was only observed for [bmpy$^+$][Tf_2N^-]. This temperature behavior might be triggered by a conformational change of the pyrrolidinium ring of the cation. For [bmpy$^+$][Tf_2N^-] saturated with water no layering was observed.

The RTILs which show a molecular layering at the interface also exhibit a correlation distance in the bulk liquid scattering similar to the layering periodicity. The typical value of about $40\,\text{mN}\,\text{m}^{-1}$ for the surface tension does not change significantly upon ion exchange. The interfacial structure at a hard wall, on the other hand, depends significantly on the ions. It is therefore concluded that the molecular layering at a hard wall corresponds to an ordering tendency which is already present in the bulk liquid.

The layer periodicity and the decay length of the molecular layering are similar in the two models for the electron density, the semi-quantitative (SQ) generic layering model and the modified distorted crystal (DC) model. Therefore, they are considered as robust findings independent of the model for the electron density. The modified distorted crystal model strongly favored a cation layer adjacent to the substrate over an anion layer.

Summarizing the results, this work has shown that the molecular structure of RTIL-solid interfaces is experimentally accessible with high energy x-ray reflectivity. Our data provide strong evidence for an exponentially decaying ionic layering perpendicular to the interface with bulk-driven characteristics. Its decay length depends strongly on the ions in the RTILs. Due to the complex nature of the probed system and the vast number of RTILs, these first molecular-level results need to be corroborated by further studies and supported by different experimental techniques.

Chapter 6

Outlook

In the following, some open questions and prospects for further studies are discussed. One of the remaining questions arising from this work focuses on the type of forces leading to the molecular layering at the solid-liquid interface. In order to get a deeper understanding of the interactions present at the interface, several aspects of the solid-liquid system ought to be studied systematically. First, the impact of the substrate material and substrate termination has not been investigated so far. All interface studies in this work have been performed with the same kind of substrate material and the same substrate termination. Alteration of the interfacial properties determined by the surface termination of the sapphire substrate could give interesting information on the effect of hydrophobic and hydrophilic interaction. Other suitable substrate materials which could be used for this kind of studies are rather scarce. However, the impact of the chemical composition of the substrate on the degree of the interfacial layering can only be studied by using chemical different substrates.

A wide field for further studies is the influence of the chemical constitution of the RTIL ions. This might be done by varying the alkyl chain length of the cations, or by changing the degree and nature of the substitutions in a systematic way. Another matter of great importance are the Coulomb forces present in such an ionic system. It is still not totally clear to which extent they are present in RTILs and how they influence the behavior of the RTILs at the interface and in the bulk. Different approaches to achieve further details upon the Coulomb interactions are imaginable. The screening of the Coulomb forces can be studied by adding different fractions of a dielectric solvent to the RTIL. Interesting insights are also expected from recording the changes triggered by adding smaller mono atomic counter anions (halides) into a RTIL. Some of these ideas have already been put into practice in our group [29].

The x-ray reflectivity experiments showed that the first ion layer next to the substrate consists in all cases of cations. This result still needs to be supported by other experimental techniques and theory. One ansatz is to perform an in situ AFM measurement at the solid-liquid interface although the feasibility of such an experiment has yet to be proven. Additional information could be gained by probing the interface with the same x-ray reflectivity technique but trying to induce a switch of the cations to the anions next to the substrate by applying an electric field forcing the ions to rearrange. It should also

be possible to determine the consistency of the ion layer next to the substrate with the scanning Kelvin probe (SKP) technique. SKP is a technique capable of retrieving the work function of a surface and/or interface [108]. The combined use of SKP together with x-ray reflectivity measurements could also detect if the high energy x-ray beam somehow charges the substrate.

In particular for industrial applications it would be important to know how impurities modify the interfacial behavior of RTILs. Sources for impurities are the synthesis of RTILs and the ambient condition at which they are kept. The synthesis process leads in many cases to a significant halide content of the RTIL. The amount clearly depends on the efficiency and cost effectiveness of the synthesis process. The cost effectiveness of large scale industrial processes depends also highly on the required environment. Therefore, it would be of interest to investigate the impact of impurities in the surrounding atmosphere on the properties of RTILs.

Nonetheless, it is clear that the before discussed obstacles will be overcome such that RTILs can deploy their unique properties in a variety of new applications and processes.

Bibliography

[1] P. Walden. Molecular Weights and Electrical Conductivity of Several Fused Salts. *Bull. Acad. Sci. St. Petersburg*, pages 405–422, (1914).

[2] J. Wilkes and J. Zaworotko. Air and water stable 1-ethyl-3-methylimidazolium based ionic liquids. *Journal of the Chemical Society Chemical Communications*, pages 965–967, (1992).

[3] H. Reichert, O. Klein, H. Dosch, M. Denk, V. Honkimäki, T. Lippmann, and G. Reiter. Observation of five-fold local symmetry in liquid lead. *Nature*, **408** 839–841, (2000).

[4] S. Maolin, Z. Fuchun, W. Guozhong, F. Haiping, W. Chunlei, C. Shimou, Z. Yi, and H. Jun. Ordering layers of [bmim][PF6] ionic liquid on graphite surfaces: Molecular dynamics simulation. *The Journal of Chemical Physics*, **128** 134504, (2008).

[5] C. Pinilla, M. Popolo, R. Lynden-Bell, and J. Kohanoff. Structure and Dynamics of a Confined Ionic Liquid. Topics of Relevance to Dye-Sensitized Solar Cells. *The Journal of Physical Chemistry B*, **109** 17922, (2005).

[6] W. Freyland, C. Zell, S. El Abedin, and F. Endres. Nanoscale electrodeposition of metals and semiconductors from ionic liquids. *Electrochimica Acta*, **48** 3053–3061, (2003).

[7] J. Rollins, B. Fitchett, and J. Conboy. Structure and Orientation of the Imidazolium Cation at the Room-Temperature Ionic Liquid/SiO2 Interface Measured by Sum-Frequency Vibrational Spectroscopy. *Journal of Physical Chemistry B*, **111** 4990–4999, (2007).

[8] C. Romero, H. Moore, T. Lee, and S. Baldelli. Orientation of 1-Butyl-3-methylimidazolium Based Ionic Liquids at a Hydrophobic Quartz Interface Using Sum Frequency Generation Spectroscopy. *Journal of Physical Chemistry C*, **111** 240–247, (2007).

[9] H. Reichert, V. Honkimäki, A. Snigirev, S. Engemann, and H. Dosch. A new X-ray transmission-reflection scheme for the study of deeply buried interfaces using high-energy microbeams. *Physica B Condensed Matter*, **336** 46–55, (2003).

[10] L. Ingber. Simulated annealing: Practice versus theory. *Mathematical and Computer Modelling*, **18** 29–57, (1993).

[11] Merck KGaA. Data sheets. *http://www.ionicliquids-merck.de*, (2008).

[12] N. Ignat'ev, U. Welz-Biermann, A. Kucheryna, G. Bissky, and H. Willner. New ionic liquids with tris(perfluoroalkyl)trifluorophosphate (FAP) anions. *Journal of Fluorine Chemistry*, **126** 1150–1159, (2005).

[13] G. Law, P. Watson, A. Carmichael, and K. Seddon. Molecular composition and orientation at the surface of room-temperature ionic liquids: Effect of molecular structure. *Physical Chemistry Chemical Physics*, **3** 2879–2885, (2001).

[14] T. Gannon, G. Law, P. Watson, A. Carmichael, and K. Seddon. First Observation of Molecular Composition and Orientation at the Surface of a Room-Temperature Ionic Liquid. *Langmuir*, **15** 8429–8434, (1999).

[15] E. Sloutskin, B. Ocko, L. Tamam, I. Kuzmenko, T. Gog, and M. Deutsch. Surface Layering in Ionic Liquids: An X-ray Reflectivity Study. *Journal of the American Chemical Society*, **127** 7796–7804, (2005).

[16] CAS. SciFinder Scholar, (2008).

[17] P. Wasserscheid and T. Welton. *Ionic Liquids in Synthesis*. WILEY-VCH , Weinheim, (2003).

[18] M. Earle, J. Esperanca, M. Gilea, J. Lopes, L. Rebelo, J. Magee, K. Seddon, and J. Widegren. The distillation and volatility of ionic liquids. *Nature*, **439** 831–834, (2006).

[19] H. Sakaebe and H. Matsumoto. N-Methyl-N-propylpiperidinium bis(trifluoromethanesulfonyl)imide (PP13–TFSI) – novel electrolyte base for Li battery. *Electrochemistry Communications*, **5** 594–598, (2003).

[20] M. Buzzeo, C. Hardacre, and R. Compton. Use of Room Temperature Ionic Liquids in Gas Sensor Design. *Analytical Chemistry*, **76** 4583–4588, (2004).

[21] A. Abbott and K. McKenzie. Application of ionic liquids to the electrodeposition of metals. *Physical Chemistry Chemical Physics*, **8** 4265–4279, (2006).

[22] A. Jimenez, M. Bermudez, F. Carrion, and G. Martinez-Nicolas. Room temperature ionic liquids as lubricant additives in steel–aluminium contacts: Influence of sliding velocity, normal load and temperature. *Wear*, **261** 347–359, (2006).

[23] C. Ye, W. Liu, Y. Chen, and L. Yu. Room-temperature ionic liquids: a novel versatile lubricant. *Chemical Communications*, pages 2244–2245, (2001).

[24] M. Van Valkenburg, R. Vaughn, M. Williams, and J. Wilkes. Ionic Liquid Heat Transfer Fluids. *Paper presented at the Fifteenth Symposium on Thermophysical Properties*, (2003).

[25] F. Liu and Y. Jiang. Room temperature ionic liquid as matrix medium for the determination of residual solvents in pharmaceuticals by static headspace gas chromatography. *Journal of Chromatography A*, **1167** 116–119, (2007).

[26] P. Wasserscheid and W. Keim. Ionic Liquids—New "Solutions" for Transition Metal Catalysis. *Angewandte Chemie*, **39** 3772–3789, (2000).

[27] D. Fort, R. Swatloski, P. Moyna, R. Rogers, and G. Moyna. Use of ionic liquids in the study of fruit ripening by high-resolution 13C NMR spectroscopy: 'green' solvents meet green bananas. *Chemical Communications*, pages 714–716, (2006).

[28] E. Borra, O. Seddiki, R. Angel, D. Eisenstein, P. Hickson, and K. Seddon. Deposition of metal films on an ionic liquid as a basis for a lunar telescope. *Nature*, **447** 979–981, (2007).

[29] H. Schröder. *in preparation*. PhD thesis, University of Stuttgart, Faculty of Mathematics and Physics, (2008).

[30] C. Santos and S. Baldelli. Surface Orientation of 1-Methyl-, 1-Ethyl-, and 1-Butyl-3-methylimidazolium Methyl Sulfate as Probed by Sum-Frequency Generation Vibrational Spectroscopy. *Journal of Physical Chemistry B*, **111** 4715–4723, (2007).

[31] S. Rivera-Rubero and S. Baldelli. Influence of Water on the Surface of the Water-Miscible Ionic Liquid 1-Butyl-3-methylimidazolium Tetrafluoroborate: A Sum Frequency Generation Analysis. *Journal of Physical Chemistry B*, **110** 15499–15505, (2006).

[32] G. Law and P. Watson. Surface orientation in ionic liquids. *Chemical Physics Letters*, **345** 1–4, (2001).

[33] B. Bhargava and S. Balasubramanian. Layering at an Ionic Liquid-Vapor Interface: A Molecular Dynamics Simulation Study of [bmim][PF6]. *Journal of the American Chemical Society*, **128** 10073–10078, (2006).

[34] E. Sloutskin, R. Lynden-Bell, S. Balasubramanian, and M. Deutsch. The surface structure of ionic liquids: Comparing simulations with x-ray measurements. *The Journal of Chemical Physics*, **125** 174715–174715, (2006).

[35] C. Aliaga, C. Santos, and S. Baldelli. Surface chemistry of room-temperature ionic liquids. *Physical Chemistry Chemical Physics*, **9** 3683–3700, (2007).

[36] G. Chevrot, R. Schurhammer, and G. Wipff. Molecular dynamics simulations of the aqueous interface with the [BMI][PF6] ionic liquid: comparison of different solvent models. *Physical Chemistry Chemical Physics*, **8** 4166–4174, (2006).

[37] P. Bonhote, A. Dias N. Papageorgiou, K. Kalyanasundaram, and M. Grätzel. Hydrophobic, Highly Conductive Ambient-Temperature Molten Salts. *Inorganic Chemistry*, **35** 1168–1178, (1996).

[38] J. Huddleston, A. Visser, W. Reichert, H. Willauer, G. Broker, and R. Rogers. Characterization and comparison of hydrophilic and hydrophobic room temperature ionic liquids incorporating the imidazolium cation. *Green Chemistry*, **3** 156–164, (2001).

[39] H. Tokuda, S. Tsuzuki, Md. Abu Bin Hasan Susan, K. Hayamizu, and M. Watanabe. How Ionic Are Room-Temperature Ionic Liquids? An Indicator of the Physicochemical Properties. *Journal of Physical Chemistry B*, **110** 19593–19600, (2006).

[40] S. Carda-Broch, A. Bethod, and D. Armstrong. Solvent properties of the 1-butyl-3-methylimidazolium hexafluorophosphate ionic liquid. *Anal Bioanal Chem*, **375** 191–199, (2003).

[41] U. Schröder, J. Wadhawan, R. Compton, F. Marken, P. Suarez, C. Consorti, R. de Souza, and J. Dupont. Water-induced accelerated ion diffusion: voltammetric studies in 1-methyl-3-[2,6-(S)-dimethylocten-2-yl]imidazolium tetrafluoroborate, 1-butyl-3-methylimidazolium tetrafluoroborate and hexafluorophosphate ionic liquids. *New Journal of Chemistry*, **24** 1009–1015, (2000).

[42] A. Choudhury, N. Winterton, A. Steiner, A. Cooper, and K. Johnson. In situ Crystallization of Low-Melting Ionic Liquids. *Journal of the American Chemical Society*, **127** 16792–16793, (2005).

[43] R. Swatloski, A. Visser, W. Reichert, G. Broker, L. Farina, J. Holbrey, and R. Rogers. Solvation of 1-butyl-3-methylimidazolium hexafluorophosphate in aqueous ethanol-a green solution for dissolving 'hydrophobic' ionic liquids. *Chemical Communications*, pages 2070–2071, (2001).

[44] R. Swatloski, J. Holbrey, and R. Rogers. Ionic liquids are not always green: hydrolysis of 1-butyl-3-methylimidazolium hexafluorophosphate. *Green Chemistry*, **5** 361–363, (2003).

[45] M. Tolan. *X-Ray Scattering from Soft-Matter Thin Films*. Springer, Berlin, (1999).

[46] J. Daillant and A. Gibaud. *X-ray and Neuron Reflectivity: Principles and Applications*, volume 58. Springer, Berlin, (1999).

[47] J. Als-Nielsen and D. McMorrow. *Elements of Modern X-ray Physics*. John Wiley & Sons Ltd., Chichester, (2001).

[48] P. Egelstaff. *An Introduction to the Liquid State*. Oxford University Press, New York, (1992).

[49] J. Pryde. *The Liquid State*. Hutchinson & CO, London, (1966).

[50] J. Sorenson, G. Hura, R. Glaeser, and T. Head-Gordon. What can x-ray scattering tell us about the radial distribution functions of water? *The Journal of Chemical Physics*, **113** 9149–9161, (2000).

[51] M. Mezger. *X-ray Studies of the Density Depletion at Hydrophobic Water-Solid Interfaces*. PhD thesis, University of Stuttgart, Faculty of Mathematics and Physics, (2008).

[52] L. G. Parratt. Surface Studies of Solids by Total Reflection of X-Rays. *Physical Review*, **95** 359–369, (1954).

[53] J. Als-Nielsen. Synchrotron x-ray studies of liquid-vapor interfaces. *Physica A Statistical and Theoretical Physics*, **140** 376–389, (1986).

[54] M. J. Regan, P. S. Pershan, O. M. Magnussen, B. M. Ocko, M. Deutsch, and L. E. Berman. X-ray reflectivity studies of liquid metal and alloy surfaces. *Physical Review B*, **55** 15874–15884, (1997).

[55] L. Ingber. Adaptive Simulated Annealing (ASA). http://www.ingber.com, (2004).

[56] M. J. Regan, E. H. Kawamoto, S. Lee, P. S. Pershan, N .Maskil, M. Deutsch, O. M. Magnussen, B. M. Ocko, and L. E. Berman. Surface Layering in Liquid Gallium: An X-Ray Reflectivity Study. *Physical Review Letters*, **75** 2498–2501, (1995).

[57] O. M. Magnussen, B. M. Ocko, M. J. Regan, K. Penanen, P. S. Pershan, and M. Deutsch. X-Ray Reflectivity Measurements of Surface Layering in Liquid Mercury. *Physical Review Letters*, **74** 4444–4447, (1995).

[58] K. Nishikawa, Y. Sakamoto, and T. Iijima. Accuracy of Intensity Measurement by Use of an Area Detector with a Photostimulable Phosphor Screen, as Confirmed by Measuring Scattering Intensity from a Liquid. *Japanese Journal of Applied Physics*, **30** 1303–1306, (1991).

[59] T. Head-Gordon and G. Hura. Water Structure from Scattering Experiments and Simulation. *Chemical Reviews*, **102** 2651–2670, (2002).

[60] C. Dwiggins and D. Park. Calculation of the Intensity of Secondary Scattering of X-rays by Non-crystalline Materials. *Acta Crystallographica Section A*, **27** 264–272, (2000).

[61] The NIST Reference on Constants, Units, and Uncertainty. *http://www.physics.nist.gov/cuu/*, (2006).

[62] B. Lengeler, C. Schroer, M. Richwin, J. Tümmler, M. Drakopoulos, A. Snigirev, and I. Snigireva. A microscope for hard x rays based on parabolic compound refractive lenses. *Applied Physics Letters*, **74** 3924–3926, (1999).

[63] M. Mezger, H. Schröder, H. Reichert, S. Schramm, J. Okasinski, S. Schöder, V. Honkimäki, M. Deutsch, B. Ocko, J. Ralston, and H. Dosch. Extended Molecular Layering of a Pyrrolidinium-Based Ionic Liquid at Sapphire (0001). *submitted*, (2008).

[64] S. Luo and C. Wong. Effect of UV/Ozone Treatment on Surface Tension and Adhesion in Electronic Packaging. *IEEE Transactions on Components and Packaging Technologies*, **24** 43–49, (2001).

[65] S. Engemann. *Premelting at the ice–SiO_2 interface - A high-energy x-ray microbeam diffraction study*. PhD thesis, University of Stuttgart, Faculty of Mathematics and Physics, (2005).

[66] A. van Oosterom and J. Strackee. The Solid Angle of a Plane Triangle. *IEEE Transactions on Biomedical Engineering*, **bme-30** 125, (1983).

[67] DURAN Group GmbH. Physical properties of Borosilicate Glass. http://www.duran-group.com/english/products/duran/properties/physik.html, (2008).

[68] K. Seddon, A. Stark, and M. Torres. Influence of chloride, water, and organic solvents on the physical properties of ionic liquids. *Pure and Applied Chemistry*, **72** 2275–2287, (2000).

[69] J. Jacquemin, P. Husson, A.. Padua, and V. Majer. Density and viscosity of several pure and water-saturated ionic liquids. *Green Chemistry*, **8** 172–180, (2006).

[70] R. de Azevedo, J. Esperanca, V. Najdanovic-Visak, Z. Visak, H. Guedes, M. da Ponte, and L. Rebelo. Thermophysical and Thermodynamic Properties of 1-Butyl-3-methylimidazolium Tetrafluoroborate and 1-Butyl-3-methylimidazolium Hexafluorophosphate over an Extended Pressure Range. *Journal of Chemical & Engineering Data*, **50** 997–1008, (2005).

[71] K. Harris, M. Kanakubo, and L. Woolf. Temperature and Pressure Dependence of the Viscosity of the Ionic Liquid 1-Butyl-3-methylimidazolium Tetrafluoroborate: Viscosity and Density Relationships in Ionic Liquids. *Journal of Chemical & Engineering Data*, **52** 2425–2430, (2007).

[72] J. Anthony, J. Crosthwaite, D. Hert, S. Aki, E. Maginn, and J. Brennecke. Phase Equilibria of Gases and Liquids with 1-n-Butyl-3-methylimidazolium Tetrafluoroborate. *Ionic Liquids as Green Solvents ACS Symposium Series*, **856** 110–120, (2003).

[73] Y. Huo, Shuqian Xia, and P. Ma. Densities of Ionic Liquids, 1-Butyl-3-methylimidazolium Hexafluorophosphate and 1-Butyl-3-methylimidazolium Tetrafluoroborate, with Benzene, Acetonitrile, and 1-Propanol at T = (293.15 to 343.15) K. *Journal of Chemical & Engineering Data*, **52** 2077–2082, (2007).

[74] A. Pereiro, J. Legido, and A. Rodrıguez. Physical properties of ionic liquids based on 1-alkyl-3-methylimidazolium cation and hexafluorophosphate as anion and temperature dependence. *The Journal of Chemical Thermodynamics*, **39** 1168–1175, (2007).

[75] G. Kabo, A. Blokhin, Y. Paulechka, A. Kabo, M. Shymanovich, and J. Magee. Thermodynamic Properties of 1-Butyl-3-methylimidazolium Hexafluorophosphate in the Condensed State. *Journal of Chemical & Engineering Data*, **49** 453–461, (2004).

[76] Z. Gu and J. Brennecke. Volume Expansivities and Isothermal Compressibilities of Imidazolium and Pyridinium-Based Ionic Liquids. *Journal of Chemical & Engineering Data*, **47** 339, (2002).

[77] R. de Azevedo, J. Esperanca, J. Szydlowski, Z. Visak, P. Pires, H. Guedes, and L. Rebelo. Thermophysical and thermodynamic properties of ionic liquids over an extended pressure range: [bmim][NTf] and [hmim][NTf]. *The Journal of Chemical Thermodynamics*, **37** 888–899, (2005).

[78] J. Kumełan, A. Perez-Salado Kamps, D. Tuma, and G. Maurer. Solubility of CO2 in the ionic liquid [hmim][Tf2N]. *The Journal of Chemical Thermodynamics*, **38** 1396–1401, (2006).

[79] R. Gardas, H. Costa, M. Freire, P. Carvalho, I. Marrucho, I. Fonseca, A. Ferreira, and J. Coutinho. Densities and Derived Thermodynamic Properties of Imidazolium-, Pyridinium-, Pyrrolidinium-, and Piperidinium-Based Ionic Liquids. *Journal of Chemical & Engineering Data*, **53** 805–811, (2008).

[80] F. M. Fowkes. Attractive Forces at Interfaces. *Industrial & Engineering Chemistry*, **56** 40–52, (1964).

[81] J. Schultz, K. Tsutsumi, and J.B. Donnet. *Journal of Colloid and Interface Science*, **59** 277, (1977).

[82] D.R. Lide. *CRC Handbook of Chemistry and Physics*, volume 88. CRC Press by Taylor & Francis Group, Boca Raton, (2008).

[83] P. Mach, C. Huang, and H. Nguyen. Dramatic Effect of Single-Atom Replacement on the Surface Tension of Liquid-Crystal Compounds. *Physical Review Letters*, **80** 732–735, (1998).

[84] I. Langmuir. *Phenomena, Atoms and Molecules*. Philosophical Library, New York, (1950).

[85] J. Sung, Y. Jeon, D. Kim, T. Iwahashi, T. Iimori, K. Seki, and Y. Ouchi. Air–liquid interface of ionic liquid + H2O binary system studied by surface tension measurement and sum-frequency generation spectroscopy. *Chemical Physics Letters*, **406** 495–500, (2005).

[86] M. Deetlefs, K. R. Seddon, and M. Shara. Predicting physical properties of ionic liquids. *Physical Chemistry Chemical Physics*, **8** 642–649, (2006).

[87] M. Freire, P. Carvalho, A. Fernandes, I. Marrucho, A. Queimada, and J. Coutinho. Surface tensions of imidazolium based ionic liquids: Anion, cation, temperature and water effect. *Journal of Colloid and Interface Science*, **314** 621–630, (2007).

[88] A. Pereiro, P. Verdia, E. Tojo, and A. Rodrıguez. Physical Properties of 1-Butyl-3-methylimidazolium Methyl Sulfate as a Function of Temperature. *Journal of Chemical & Engineering Data*, **52** 377–380, (2007).

[89] V. Halka, R. Tsekov, and W. Freyland. Peculiarity of the liquid/vapour interface of an ionic liquid: study of surface tension and viscoelasticity of liquid BMImPF6 at various temperatures. *Physical Chemistry Chemical Physics*, **7** 2038–2043, (2005).

[90] S. Dzyuba and R. Bartsch. Influence of Structural Variations in 1-Alkyl(aralkyl)-3-Methylimidazolium Hexafluorophosphates and Bis(trifluoromethylsulfonyl)imides on Physical Properties of the Ionic Liquids. *ChemPhysChem*, **3** 161–166, (2002).

[91] L. Rebelo, J. Lopes, J. Esperanca, and E. Filipe. On the Critical Temperature, Normal Boiling Point, and Vapor Pressure of Ionic Liquids. *The Journal of Physical Chemistry B*, **109** 6040–6043, (2005).

[92] S. Millefiorini, A. Tkaczyk, R. Sedev, J. Efthimiadis, and J. Ralston. Electrowetting of Ionic Liquids. *Journal of the American Chemical Society*, **128** 3098–3101, (2006).

[93] P. du Noüy. A new apparatus for measuring surface tension. *The Journal of General Physiology*, **1** 521–524, (1919).

[94] A. Triolo, A. Mandanici, O. Russina, V. Rodriguez-Mora, M. Cutroni, C. Hardacre, M. Nieuwenhuyzen, H. Bleif, L. Keller, and M. Ramos. Thermodynamics, Structure, and Dynamics in Room Temperature Ionic Liquids: The Case of 1-Butyl-3-methyl Imidazolium Hexafluorophosphate ([bmim][PF6]). *Journal of Physical Chemistry B*, **110** 21357–21364, (2006).

[95] S. Dibrov and J. Kochi. Crystallographic view of fluidic structures for room-temperature ionic liquids: 1-butyl-3-methylimidazolium hexafluorophosphate. *Acta Crystallographica Section C Crystal Structure Communications*, **62** o19–o21, (2005).

[96] C: Hardacre, S. MacMath, M. Nieuwenhuyzen, D. Brown, and A. Soper. Liquid structure of 1, 3-dimethylimidazolium salts. *Journal of Physics Condensed Matter*, **15** S159–S166, (2003).

[97] C. Hardacre, S. McMath, D. Bowron, and A. Soper. Structure of molten 1,3-dimethylimidazolium chloride using neutron diffraction. *The Journal of Chemical Physics*, **118** 273–278, (2003).

[98] K. Matsumoto, R. Hagiwara, Y. Ito, and S. Kohara an K. Suzuya. Structural analysis of 1-ethyl-3-methylimidazolium bifluoride melt. *Nuclear Instruments and Methods in Physics Research Section B Beam Interactions with Materials and Atoms*, **199** 29–33, (2003).

[99] J. Fuller, R. Carlin, H. De Long, and D. Haworth. Structure of 1-ethyl-3-methylimidazolium hexafluorophosphate: model for room temperature molten salts. *Journal of the Chemical Society Chemical Communications*, pages 299–300, (1994).

[100] S. Urahata and M. Ribeiro. Structure of ionic liquids of 1-alkyl-3-methylimidazolium cations: A systematic computer simulation study. *The Journal of Chemical Physics*, **120** 1855–1863, (2004).

[101] The Cambridge Crystallographic Data Centre. Mercury visualization software. http://www.ccdc.cam.ac.uk/products/mercury/, (2008).

[102] L. Cammarata, S. Kazarian, P. Salter, and T. Welton. Molecular states of water in room temperature ionic liquids Electronic Supplementary Information available. See http://www.rsc.org/suppdata/cp/b1/b106900d/. *Physical Chemistry Chemical Physics*, **3** 5192–5200, (2001).

[103] C. Romero and S. Baldelli. Sum Frequency Generation Study of the Room-Temperature Ionic Liquids/Quartz Interface. *The Journal of Physical Chemistry B*, **110** 6213–6223, (2006).

[104] R. Sheldon. Catalytic reactions in ionic liquids. *Chemical Communications*, pages 2399–2407, (2001).

[105] S. Saha, S. Hayashi, A. Kobayashi, and H. Hamaguchi. Crystal Structure of 1-Butyl-3-methylimidazolium Chloride. A Clue to the Elucidation of the Ionic Liquid Structure. *Chemistry Letters*, **32** 740–741, (2003).

[106] S. Raj, G. Kumar, R. Mohan, R. Jayavel, and B. Varghese. Crystal structure and vibrational analysis of novel nonlinear optical L-histidinium tetrafluoroborate (L-HFB) single crystals. *physica status solidi (b)*, **244** 558–568, (2007).

[107] T. Fujimori, K. Fuji, R. Kanzaki, K. Chiba, H. Yamamoto, Y. Umebayashi, and S. Ishiguro. Conformational structure of room temperature ionic liquid N-butyl-N-methyl-pyrrolidinium bis(trifluoromethanesulfonyl) imide — Raman spectroscopic study and DFT calculations. *Journal of Molecular Liquids*, **131-132** 216–224, (2007).

[108] M. Rohwerder and F. Turcu. High-resolution Kelvin probe microscopy in corrosion science: Scanning Kelvin probe force microscopy (SKPFM) versus classical scanning Kelvin probe (SKP). *Electrochimica Acta*, **53** 290–299, (2007).

Acknowledgment

Mein Dank gilt allen, die zum Gelingen dieser Arbeit beigetragen haben. Im Einzelnen sind dies:

- **Prof. Dr. Helmut Dosch** für das Ermöglichen dieser Arbeit.
- **Prof. Dr. Jörg Wrachtrup** für die Übernahme des Mitberichts.
- **Dr. Harald Reichert** für die Betreuung und Durchsicht dieser Arbeit, die Vermittlung der experimentellen Fertigkeiten sowie theoretischer Details.
- **Dr. Markus Mezger** und **Heiko Schröder** von denen ich vieles lernen konnte und die mir immer mit Rat und Tat zur Seite standen.
- **Dr. Sebastian Schöder**, **Dr. John Okasinski** und **Dr. Sandrine Dourdain** für ihre Hilfe und Unterstützung, vor allem als *local contacts* in Grenoble.
- Die Mitarbeiter der ID15A an der ESRF, im Besonderen **Dr. Veijo Honkimäki**, **Dr. Diego Pontoni**, **Dr. Thomas Buslaps**, **Anthony Mauro** und **Dr. Harald Müller** für die Unterstüzung im zentralen Chemielabor an der ESRF.
- **Prof. Dr. Moshe Deutsch** und **Prof. Dr. Jörg Bilgram** für anregende Gespräche und Diskussionen nicht nur über diese Arbeit.
- **Dr. Emerson De Souza** für die Hilfe mit den Grenzflächenmessungen und die vielen erkenntnis-philosophischen Gespräche.
- **Annette Weißhardt**, **Frank Adams**, **Thomas Meisner** und **Arnold Weible** für die großartige technische Unterstützung.
- **Michael Schäfer** aus der mechanischen Werkstatt am ITAP und **Helmut Kammerlander** aus der Glaswerkstatt jeweils mit ihrem Team.
- **Dr. János Major** und **Dr. Andras Major** für den Betrieb und die Wartung des Clusters zur Datenanalyse und **Taufan Zimmer** für die IT-Unterstützung.
- **Ass.-Prof. Dr. Alejandro Diaz-Ortiz**, **Stefanos Tzivanakis** und **Navid Khorshidi** für die vielen aufschlußreichen Diskussionen.
- Alle Kollegen der Abteilung Dosch.
- Meine Familie und ganz besonders **meine Eltern** für die vielseitige Unterstützung.

Selbständigkeitserklärung

Hiermit bestätige ich, dass diese Arbeit selbständig angefertigt wurde. Alle verwendeten Quellen und Hilfsmittel sind angegeben.

Sebastian M. Schramm